UNIVERSITA' degli STUDI di ROMA
TOR VERGATA

Flares in Blazars

Alessandro Paggi

Università degli Studi di Roma "Tor Vergata"
Facoltà di Scienze Matematiche Fisiche Naturali
Dipartimento di Fisica
Via della Ricerca scientifica, 1, I-00133, Rome (Italy)

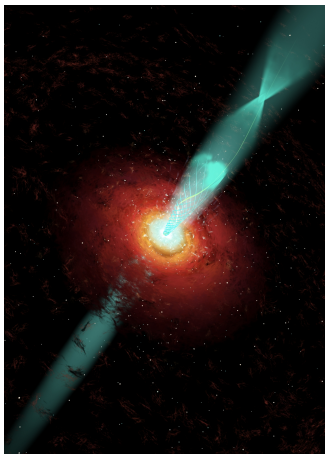

PhD THESIS

A.A. 2009/2010

Supervisor: Prof. F. Vagnetti

Co-supervisors: Prof. A. Cavaliere, Dr. A. Lapi

Coordinator: Prof. P. Mazzotta

PhD in Astronomy XXIII Cycle

Abstract:

Blazars are active galactic nuclei characterized by strong, nearly pure non-thermal radiations; these extend across the electromagnetic spectrum, from radio frequencies to the most energetics γ rays observed, in some cases up to TeV energies. They represent an ideal benchmark to test several fields of high energy astrophysics, like particle acceleration and emission processes. To this aim, a multi-λ approach is essential to disentangle the various processes taking place in these objects.

Even more enticing to understand Blazars physics is their variability, and in particular their "flares"; they are apparently random, substantial flux increases, taking place on timescales of days or less, in some cases down to hours. Flares may occur in different energy bands, and in this work I will in particular study how flux variations at different wavelength can be interpreted in terms of the underlying physical processes taking places in different type of Blazars.

Blazars are in fact divided in two major classes: BL Lacs and FSRQs. Both are widely held to radiate from a narrow relativistic jets closely aligned with observer's line of sight, and originating from a central engine constituted by a supermassive black hole coupled with a surrounding accretion disk. On the other hand, the differences between Blazars spectra point toward different environments surrounding the central black hole.

In fact, BL Lacs show no or just weak and intermittent emission lines, and yield no observational evidence of thermal emission from the accretion disk; these features can be interpreted in terms of scarce surrounding gas and small ongoing accretion. BL Lacs spectra are effectively interpreted in terms of pure synchrotron-self Compton (SSC) radiation, that is, synchrotron emission (in the bands from infrared to soft X-rays) from highly relativistic electrons inside the jet, and inverse Compton upscattering (radiating in the MeV - TeV energy range) by the same electrons on seed photons of the very synchrotron radiation.

FSRQs, on the other hand, with their broad emission lines and strong Big Blue Bump (BBB) yield evidence of plenty surrounding gas, associated to high current accretion rates onto the disk. Both emission lines and BBB provide seed photons that can be Compton scattered by the electrons inside the jets (the so called external Compton scenario), yielding the high γ-ray outputs often dominating their spectra.

Making use of refined and updated SSC models involving both analytical relations and numerical simulations I have performed detailed studies of flaring episodes of a number of BL Lacs, pushing the homogeneous single-zone SSC model to its limits to test whether it can explain observed multi wavelength variabilities, or more complex, structured sources are required.

Moreover, I investigated two saturation effects that can limit flux increase and so affect flaring behavior, either due to the particle acceleration processes or to the total available power. The latter, in particular, relates to the limited available power extractable from the central rotating hole via the Blandford-Znajek electrodynamical mechanism, involving the interplay between the accretion disk and the hole, governed by strong gravity effects of General Relativity; this mechanism is relevant for BL Lacs with very small current accretion rates. FSRQs, on the other hand, show evidences of high ongoing accretion and so easily overcome this limit.

My results show that the different physical properties of Blazars reflect into different flaring behaviors. While in BL Lacs the main driver of flaring episodes is provided by particle *acceleration* processes taking place *inside* the jets to energies $\gamma \simeq 10^6$, in FSRQs we understand flares in terms of increased *accretion* rates providing more and harder *external* photons to be inverse Compton scattered. In addition, the saturation effects taking place in BL Lacs reinforce these differences, yielding *divergent* flaring patterns for the two subclasses on the luminosity vs. electron energy plane.

Finally, to investigate the acceleration processes taking place in BL Lacs jets, I performed an extensive X-ray analysis of high-frequency peaked sources not (yet) detected at TeV energies, in order to compare these with those detected at such energies, to outline a simple electrostatic acceleration model to interpret their peak frequencies distribution and to single out some good TeV candidates.

Keywords:
– radiative non-thermal processes
– acceleration mechanisms
– jets – Active Galactic Nuclei
– Blazars

Guidelines to the reader:

This thesis is mostly based on theoretical interpretation and discussion of blazar observational properties. All new results found during these studies are published or submitted to the astronomical international reviews Astronomy & Astrophysics and The Astrophysical Journal, and have been presented in several conferences.

In writing this thesis I decided to directly focus on the work I carried on during my PhD, leaving classical results and mathematical details to the appendixes. The interested reader can found the discussion of the relevant radiation mechanisms and acceleration processes in Appendix A, while in Appendix B I presented analytical solutions of the diffusion equation relevant to the blazar physics.

In Chapter One an historical introduction combined with main observational properties and interpretations of blazars is reported.

In Chapter Two I presented the acceleration mechanisms that yield *curved* electron populations, and discussed how the former radiate the curved spectra that I mainly adopted for describing the blazar emissions; I have also shown here scaling relations between the parameters of the electron population and the corresponding emitted spectra.

In Chapter Three I applied this relations to interpret and predict correlations between spectral parameters of BL Lacs, to pinpoint the main driver of the flares of these sources; in this chapter I also investigated the limits of the simple Synchrotron Self Compton model.

In Chapter Four I presented a comprehensive framework to interpret blazar flares, and I showed how the physical differences between two main blazar subclasses, BL Lacs and FSRQs, are reflected in their flaring activity; moreover, I showed how limited power available to BL Lac sources may reinforce these dichotomy.

Chapter Four is dedicated to the investigation of the acceleration mechanisms in BL Lacs; here I presented an extensive X-ray analysis of high-frequency peaked sources not yet detected at TeV energies, and I outlined a simple electrostatic model to interpret their peak frequencies distribution; here I also draw a criterion to select some TeV candidates. The results of this analysis are presented in Appendix C.

Finally, in Chapter Six, the summary and the conclusions are presented.

Acknowledgments

This thesis is realized within the Astronomy PhD Course (XXIII cycle) of the Rome University "Tor Vergata.

I thank first Profs. Fausto Vagnetti and Alfonso Cavaliere, for giving me the possibility to carry out my research activity during these years; I am really grateful to them for many interesting discussions that allowed me to learn the spirit of astronomical research and to grow, both as a scientist and a person. I thank a lot Dr. Marco Tavani for helpful discussions and encouragements in my PhD.

I also thank Prof. Pasquale Mazzotta, my PhD coordinator, and all Professors that followed me during these three years with helpful discussion and courses.

Really special thanks go to Francesco Massaro, that introduced me X-ray data analysis and for his supported during my stay at the Harvard-Smithsonian CfA, both on professional and personal field. I thank a lot Valerio Vittorini, Filippo D'Ammando and Andrea Lapi, for helpful and enriching discussions.

Last but not least, I greatly thank my family and my girlfriend Barbara, for their support, their encouragements and their sustain in my research activity.

List of publications concerning the PhD thesis

Refereed papers

- *SSC radiation in BL Lac sources, the end of the tether*, **A. Paggi**, F. Massaro, V. Vittorini, A. Cavaliere, F. D'Ammando, F. Vagnetti & M. Tavani, 2009a, A&A, 504, 821
- *Power for dry BL Lacertae objects* **A. Paggi**, A. Cavaliere, V. Vittorini & M. Tavani, 2009b, A&A, 508L, 31
- *Powerful High Energy Emission of the Remarkable BL Lac Object S50716+714*, V. Vittorini, M. Tavani, **A. Paggi**, A. Cavaliere, A. Bulgarelli, A. W. Chen, F. D'Ammando, I. Donnarumma, A. Giuliani, F. Longo, L. Pacciani, G. Pucella, S. Vercellone, A. Ferrari, S. Colafrancesco & P. Giommi, 2009, ApJ, 706, 1433
- *Gamma-ray Bursts in the Fermi Era: The Spectral Energy Distribution of the Prompt Emission*, F. Massaro, J. E. Grindlay & **A. Paggi**, 2010, ApJ, 714L, 299

Presentations at Meetings and Conferences

- *BL Lacs energetics: the TXS 0716+714 case*, V. Vittorini, M. Tavani, **A. Paggi**, & A. Cavaliere, 6th AGILE Workshop, Milan, April 2009
- *The Power form BL Lacs*, **A. Paggi**, PROC. 1st Young Researcher Meeting Rome CONF., in press, Rome, Jul 2009
- *Power from Dry BL Lacs*, **A. Paggi**, A. Cavaliere, V. Vittorini, & M. Tavani, PROC. 7th *AGILE* Workshop CONF., in press, Rome, Sep 2009
- *The Power From Dry BL Lacs*, **A. Paggi**, A. Cavaliere, F. Massaro, V. Vittorini, & M. Tavani, 20th New England Regional Quasar and AGN Meeting, Boston, May 2010
- *BL Lacs bright in gamma rays*, **A. Paggi**, V. Vittorini, A. Cavaliere, & M. Tavani, PROC. 2nd Roma International Conference on Astro-Particle Physics CONF., in press, doi:10.1016/j.physletb.2003.10.071, Rome, May 2009
- *SSC radiation in BL Lac sources, the end of the tether*, **A. Paggi**, F. Massaro, V. Vittorini, A. Cavaliere, F. D'Ammando, F. Vagnetti, & M. Tavani, International Conference of Astrophysics: 2009 Fermi Symposium, Washington DC, November 2009

A mia madre

Contents

1

INTRODUCTION

1.1 General AGN properties

An Active Galactic Nucleus (AGN) is a galaxy with a central, compact region that can reach $10^2 - 10^3$ times the luminosity of the whole host galaxy (Peterson, 1997; Kembhavi & Narlikar, 1999); in fact, these nuclei emit bolometric luminosities $L \sim 10^{42} \div 10^{48}$ erg/s, with spectra extending across all observed frequencies from radio to the most energetic γ rays, and featuring continuum emission, and often broad and narrow emission and absorption lines. AGN emission is also characterized by strong variability on timescales of the order of years that often go down to days or hours (and sometimes to minutes).

The central "engine" powering AGNs is widely held to be a supermassive black hole (SMBH), with masses $M_\bullet \sim 10^6 \div 10^9 M_\odot$; being the characteristic size scale for BH the Schwarzschild radius

$$R_S = \frac{2GM_\bullet}{c^2} \simeq 3 \times 10^{13} \frac{M_\bullet}{10^8 M_\odot} \text{ cm},$$

the size of the AGN central region will be expressed in terms of $R_s \sim 10^{11} \div 10^{14}$ cm. Around the central BH lies an accretion disk, where the matter looses angular momentum and fall on the BH, converting gravitational energy is quasi-thermal radiation. If the accreted mass is M, the released energy is

$$E = \eta M c^2,$$

where η is the process efficiency in converting gravitational energy into radiation. It is possible to evaluate this efficiency with a simple newtonian calculation; the last stable orbit for a particle around a non rotating BH is $R_{lso} = 3R_s$, so that

$$L \simeq \frac{GM}{2R_{lso}} \frac{dM}{dt} = \frac{1}{12} \frac{dM}{dt} c^2,$$

yielding $\eta \approx 0.08$. On the other hand, accurate general relativity calculations yield $0.06 \leqslant \eta \lesssim 0.4$, far larger than the efficiency for stellar thermonuclear reaction $\eta^* \lesssim 0.008$.

If mass is accreted to the central BH at a rate dM/dt, the available power will therefore be

$$L = \eta \frac{dM}{dt} c^2;$$

this power is effectively normalized in terms of the Eddington luminosity

$$L \leq L_E = 4\pi c \frac{G M_\bullet m_P}{\sigma_T} \approx 1.3 \times 10^{46} \frac{M_\bullet}{10^8 M_\odot} \text{ erg/s},$$

where m_P is the proton mass and σ_T is the Thomson cross section; this luminosity corresponds to an accretion rate $\dot{M}_E = 4\pi \frac{G M m_p}{c \sigma_T} \approx 1.4 \times 10^{25} \left(M_\bullet/10^8 M_\odot\right)$ g/s $= 0.2 \left(M_\bullet/10^8 M_\odot\right) M_\odot$/yr, useful for normalizing accretion rates to $\dot{m} \equiv \dot{M}/\dot{M}_E$. If $L > L_E$ in symmetrically accreting source, radiation pressure will wipe away the incoming matter, thus stopping the accretion; nevertheless, for strongly

asymmetrical sources, with equatorial accretion and polar emission, this limit can be greatly overcome; this is the case for the AGN subclass of Blazars, that will be discussed in detail in this work.

The accretion disk can be modeled as a series of concentric annular black bodies, with temperatures that increase at inner radii up to about $5\,10^4$ K°; the total disk emission will therefore be the sum of each annulus emissions.

Around the accreting disk there is a "corona" of energetic electrons emitting synchrotron radiation, and inverse Compton scattering photons of the very synchrotron radiation or those coming from other sources up to X and γ rays.

Farther from the central BH lies an obscuring dust torus; also, there are orbiting gas clouds, ionized by the radiation from the accreting disk and thus emitting lines. Clouds closer to the disk (in the so called broad line region, BLR) are dens and fast moving, and emit optical and UV lines, broadened by Doppler effect; on the other hand, farther clouds, above and under the torus (in the narrow line region, NLR), are optically thin, less dense and slower than the others, and emit narrow optical lines.

Lastly (but not least), from the polar regions the AGN launches collimated, relativistic jets of non thermal radiation. When these jets happen to be closely aligned to the line of sight, they blaze the observer, often overwhelming other emissions, as a result of special relativity aberration and Doppler effects. As a matter of fact, these sources are called Blazars, and constitute an intriguing AGN subclass: this work will be mainly focused on these kind of sources.

To sum up, AGN mainly feature two emission kind: a thermal one from the accreting disk, and a non thermal one that can equal or even dominate the former in Blazars. The non thermal emission is due both to synchrotron emission from electron in the corona and from inverse Compton scattering of these electron on the synchrotron radiation itself (in the synchrotron-self Compton process), on disk radiation photons (originating strong emission in the blue region of the optical spectrum, the so called "Big Blue Bump"), or on photons coming from other regions, like for example the BLR; moreover, optical and UV emission and absorption lines originate form the interaction between the disk radiation and the surrounding gas clouds.

1.2 Quasars

AGNs that in optical wavelengths appear as small magnitude source are traditionally referred to as quasars; they were initially interpreted as stars, but they also showed radio emission, not present in stellar object, and they were so called quasi-stellar radio source (Schmidt, 1963). Moreover, while stellar spectra are constituted by black body emission with absorption lines, while quasar emission is mainly constituted by continuum extending from radio to more energetic γ rays, with emission lines typically falling in the optical wavelength; redshift of those lines allows distance measurements up to 10 Gpc, yielding isotropic luminosities $L > 10^{45}$ erg/s, higher than galactic ones.

Emission variability allows to set an upper limit to quasar size; in fact, if a substantial luminosity variations occur on timescale T, the casually connected source size has to be $R \leq cT$. As said before, variation timescale of some AGNs is of the order of days, so their size must be $R \sim 10^{15}$ cm. For Blazars, anyway, observed emissions come from highly relativistic jets launched toward the observer, so observed variation times are smaller than the intrinsic ones; but the formation and collimation of those jets again require $R \sim 10^{15}$ cm.

1.3 AGN classification

AGNs feature a variety of different observational features. A first classification can be made basing on the source radio emission (Kellermann et al., 1989) denoting with F_5 and F_B the specific radio fluxes at 5 GHz and the specific optical flux at 6.8×10^{14} Hz, respectively, AGNs can be classified as radio quiet (RQ) or radio loud (RL), whether $F_5/F_B \leqslant 10$ or $F_5/F_B \geqslant 10$, respectively.

Furthermore, RQ and RL AGNs can be subdivided, basing on their spectral properties, in three

subclasses: type 2 AGNs, with weak continua, narrow lines and low X-ray emission; type 1 AGNs, showing strong continua, broad emission lines and strong X-ray emission up to 10 keV; and type 0 AGNs, showing no or very weak lines.

Type 2 AGNs comprise: Seyfert 2 galaxies, with strong optical emission lines; Narrow Line X Galaxies (NLXG) (Mushotzky, 1982); Narrow Line Radio Galaxies (NLRG), where radio emission is due to synchrotron radiation by relativistic electrons in the active nucleus, and show narrow lines and large radio lobe with sizes even greater than Mpcs. Narrow Line Radio Galaxies can be subdivided in FRI (with diffused radio masses) and FRII (showing collimated jets and radio lobes) (Faranoff & Riley, 1974).

Type 1 ANGs comprise: Seyfert 1 galaxies, similar to Seyfert 1 but less intense; radio quiet quasars, much more numerous than radio loud ones, that in about 10% show broad optical absorption lines and therefore called Broad Absorption Line (BAL) quasars (Turnshek, 1984); Broad Line Radio Galaxies (BLRG), similar to NLRG but showing broad lines; Highly Polarized Quasars (HPQs), with polarized flux and broad lines; Core Dominated Quasars (CDQs); and RL quasars, showing non thermal continua, red-shifted emission line, strong X-ray emission and optical and radio variability. Radio loud quasars can be classified basing on the radio spectral index $F_\nu \propto \nu^{-\alpha}$; if $\alpha > 0.5$ RL quasars are called Steep Spectrum Radio Quasar (SSRQs), if $\alpha < 0.5$ they are called Flat Spectrum Radio Quasar (FSRQs). The latter feature an excess emission in the UV usually known as "Big Blue Bump", probably due to accretion disk thermal emission (Paltani et al., 1998). A sub-sample of FSRQs is constituted by Optically Violently Variable (OVV) AGN, with polarized optical continua, strong radio and optical variability and evidences of super-luminal motion.

Finally, we have type 0 AGNs, also called BL Lac objects. The archetype of this object class, BL Lacertae, was originally discovered in 1929 as a star (Hoffmeister, 1929); later it has been associated with a variable radio source (Schmitt, 1968), with apparently irregular pattern of brightening and dimming. Moreover, the spectrum of BL Lacertae showed no absorption nor emission lines. When other objects with same features have been discovered, they had been classified as BL Lac objects (Strittmatter et al., 1972). BL Lacertae was found to be located in a normal elliptical galaxy (Oke & Gunn, 1974), and obscuring the central region the surrounding area showed absorption lines that permitted a red-shift estimate $z \simeq 0.07$; this yields a distance of about 400 Mpc, indicating that the nuclear region of BL Lacertae has an isotropic luminosity $L \simeq 10^{46}$ erg s^{-1}. In general, BL Lac objects are compact radio sources with polarized emission, spectra showing no emission lines, and strong continua rapidly varying on timescales that goes down to days. They are observed at low red-shifts ($z \lesssim 0.2$), and show strong evidences of super-luminal motion.

1.4 The unified model

Antonucci in 1993 and Urry & Padovani in 1995 proposed an unification model for AGNs. In this model AGNs feature cylindric symmetry, with radiation jets emitted along the symmetry axis; in this scheme the different observational features of AGNs are essentially due to different observation angles with respect to the jet axis (see Fig. 1.1). For viewing angles $\simeq 90°$, the line of sight crosses the dusty torus, which obscures BLR emissions, and so the observed spectra do not feature broad lines (type 2 ANGs); for small viewing angles, on the other hand, we can see the BLR emissions and so the broad lines (type 1 AGNs).

Therefore the same source type seen under decreasing viewing angles will feature different observational features. So in RQ AGNs we can pass from Seyfert 2 galaxies, to Seyfert 1 galaxies, to RQ quasars. Similarly, in RL AGNs we pass from NLRG to BLRG: in particular we pass from FRII to FSRQs to SSRQ, and from FRI to BL Lacs. Moreover OVV AGNs may be FSRQs observed under very small viewing angles.

Both BL Lacs and FSRQs are therefore AGNs with jets that happen to be closely aligned with the observer line of sight; in this case the jet non-thermal luminosity is enhanced by relativistic effects,

and *blaze* the observer and overwhelming other emission from the nucleus. Those kind of sources are therefore called Blazars.

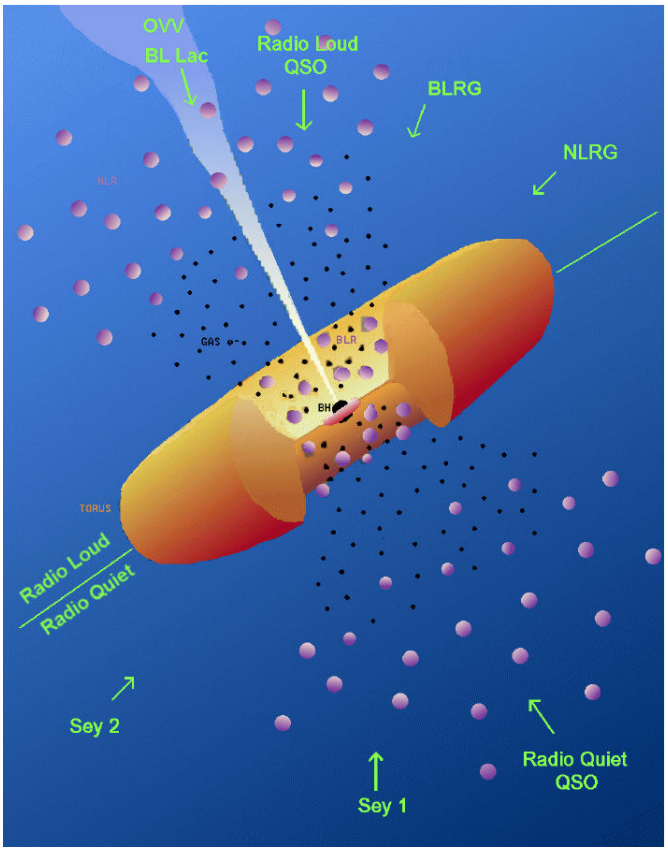

Figure 1.1: Unified model for AGNs.

1.5 Blazars

Blazars are characterized by high and variable polarization, super-luminal motion, very high luminosities, flat radio spectrum that steepens in the IR-optical bands and a rapid variability from the radio to X-ray bands, with weak or absent emission lines. As previously said, observational properties of BL Lac objects have been interpreted in terms of a relativistic jet closely aligned with the line of sight (Blandford & Rees, 1978).

In 1981 Moore & Stockman performed a polarization survey in which they discovered 17 HPQs and discussed their link to BL Lacs (Moore & Stockman, 1981), establishing the division of Blazars in the two main subgroups now referred to as BL Lacs and FSRQ.

Jet emission form Blazars is enhanced by relativistic beaming effects; in fact, the intrinsic jet-frame luminosity L' is related to the inferred isotropic luminosity L by

$$L = \frac{\delta^4}{(1+z)^2} L' ,$$

having denoted with δ the beaming factor

$$\delta = \frac{1}{\Gamma(1 - \beta\cos\theta)},$$

where Γ is the bulk motion Lorentz factor and θ is the observing angle; so the non-thermal continuum emission from the jet may completely overwhelm other kind of emission. The same beaming factor is also responsible for the apparent super-luminal motions observed in BL Lacs and FSRQs; the latter, as said before, features an excess emission in the UV called Big Blue Bump, probably due to thermal emission from the disk accreting at $\dot{m} \sim 1$, not observed in BL Lacs with $\dot{m} \sim 10^{-2}$. So, while in BL Lacs we mainly observe non-thermal jet emission, in FSRQs this is reprocessed and mixed to others.

In general, Blazar emission extends from radio to TeV energies; their emission, when represented with the spectral energy distribution (SED) $S_\nu = \nu F_\nu$, is characterized by a double hump: the first component typically peaks from IR to X-ray band, while the second one peaks high energy gamma-rays.

It is widely agreed that the low-energy component is produced by synchrotron radiation by ultra-relativistic electrons in the jet. In BL Lacs, following the widely entertained synchrotron-self Compton scenario (SSC) (Jones et al., 1974; Marscher & Gear, 1985; Ghisellini & Maraschi, 1989; Maraschi et al., 1992), the second component may be interpreted as inverse-Compton scattering of the synchrotron photons by the same electron population; in FSQRs, additional external photons sources are likely.

BL Lacs can be classified basing on their relative energetic content; Padovani & Giommi (1995a) defined the two main subclasses "Low-frequency peaked BL Lacs" (LBLs) and "High-frequency peaked BL Lacs" (HBLs), depending on whether $\Phi_{RX} = log(F_{5\,GHz}/F_{1\,keV})/7.68$ is greater or less than 0.75, respectively. In the same way Maselli et al. (2010) classify BL Lac on the basis on the ratio between the X-ray and radio flux $\Phi_{XR} = 10^{-12} F_X/f_R$, where F_X is the X-ray flux in the $0.1 - 2.4$ keV band expressed in erg cm^{-2} s^{-1} and f_R is the radio flux density at 1.4 GHz expressed in mJy; HBLs have values of $\Phi_{XR} > 1$, while LBLs attain at $\Phi_{XR} < 0.1$. Of course, between the two subclasses lie "Intermediate-frequency peaked BL Lacs" (IBLs).

In LBLs synchrotron power peaks at submm to IR wavelengths while the inverse Compton component peaks at GeV energies; in HBLs, on the other hand, synchrotron SED peaks at UV to X-ray wavelengths, while the inverse Compton component peak reaches TeV energies. So usually X-ray observations of HBLs show the peak and the fall of the synchrotron emission and for LBLs the rise of inverse Compton radiation; examples of SEDs of a LBL, IBL and HBL are plotted in Figs. 1.2, 1.3 and 1.4, respectively.

Recently, another classification has been proposed, based on the spectral properties of BL Lacs (Abdo et al., 2010b), in particular on the SED peak frequency of the synchrotron component ν_S: for $\nu_S \lesssim 10^{14}$ Hz we have Low Synchrotron Peaked (LSP) Blazars, for 10^{14} Hz $\lesssim \nu_S \lesssim 10^{15}$ Hz we have Intermediate Synchrotron Peaked (ISP) Blazars, and for $\nu_S \gtrsim 10^{15}$ Hz we have of course High Synchrotron Peaked (HSP) Blazars.

The continuum shapes of FSRQs are very similar to those of LBLs (Sambruna et al., 1996), with synchrotron peaks at $10^{13} - 10^{14}$ Hz and Compton peaks at $10^{22} - 10^{23}$ Hz. In general, FSRQs are more luminous than BL Lacs, with the ratio of Compton to synchrotron power higher than for LBLs. This suggests possible additions to SSC process, in particular inverse Compton scattering on electrons in the jet with photons coming from the accretion disk or BLR (Dermer & Schlickeiser, 1993; Sikora et al., 1994; Ghisellini et al., 1998). The SED of a FSRQ is shown in Fig. 1.5.

1.6 Characterizing Blazar flares

As mentioned before, Blazars undergo apparently random flux increases usually named "flares". To characterize and describe spectral variations in different wavelengths it is useful to make use of intrin-

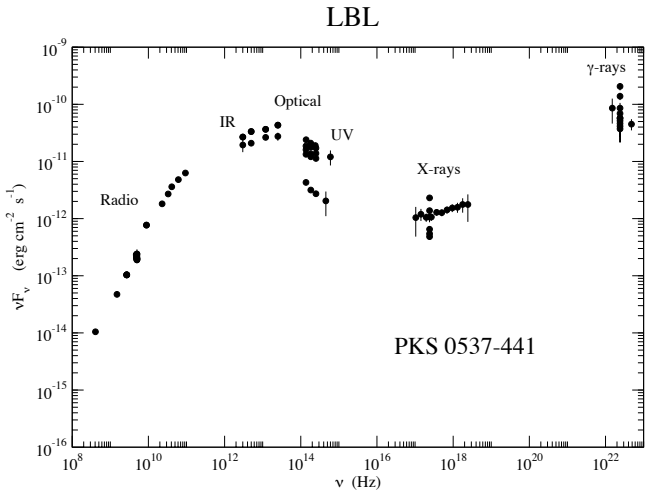

Figure 1.2: The spectral energy distribution of PKS 0537-441, an example of a low frequency peaked BL Lac object.In this source the peak of the first component lies between the IR and the optical band.

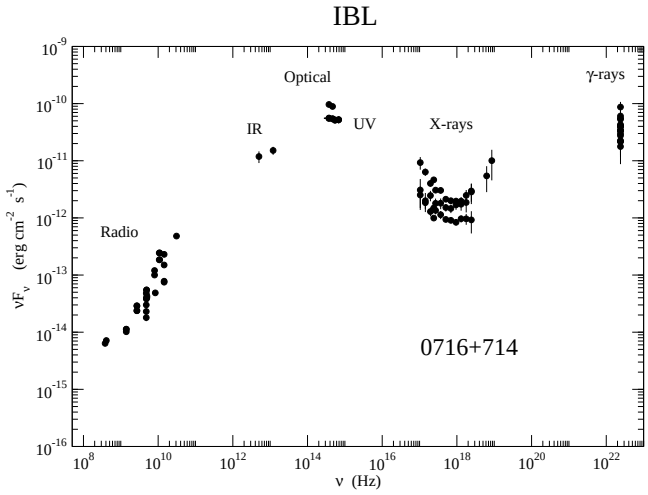

Figure 1.3: The spectral energy distribution of 0716+714, an example of an intermidiate BL Lac object. In this source, in the X-ray band it is possible to see both the fall of the first component and the rise of the second one.

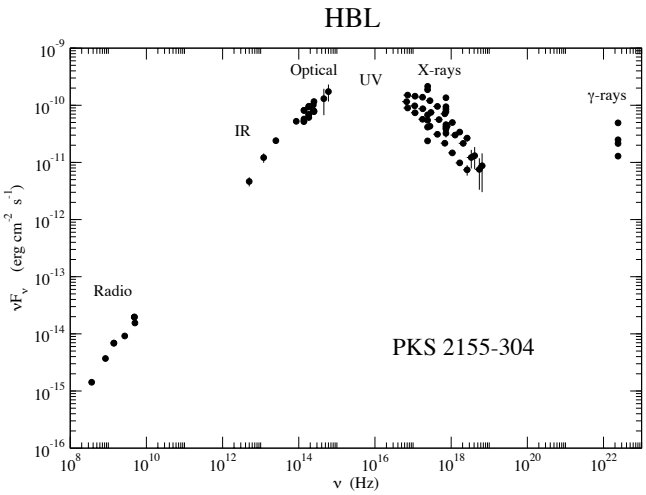

Figure 1.4: The spectral energy distribution of PKS 2155-304, an example of a high frequency peaked BL Lac object.In this source the peak of the first component lies in the X-ray band.

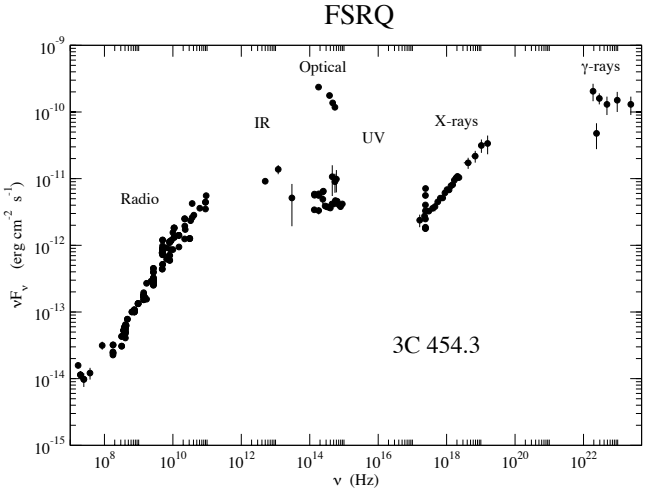

Figure 1.5: The spectral energy distribution of 3C 454.3, an example of a Flat Spectrum Radio Quasar.

sically curved spectra, in the shape of a log-parabola, that is

$$F_\nu = F_0 \left(\frac{\nu}{\nu_0} \right)^{-a-b\log\left(\frac{\nu}{\nu_0}\right)}.$$

Such spectra has been first proposed as a fitting tool for BL Lac spectra by Landau R. et al. (1986), In fact, precise X-ray measurements (with instruments onboard satellites like *XMM-Newton*, *Swift*, *BeppoSAX*, *Chandra*, etc.) allow a refinement of the classical power-law spectra, to introduce second order features. Later, Massaro E. et al. proposed log-parabolic to originate from curved electrons distributions (Massaro et al., 2004a,b, 2006)

$$N(\gamma) = N_0 \left(\frac{\gamma}{\gamma_0} \right)^{-s-r\log\left(\frac{\gamma}{\gamma_0}\right)},$$

and investigated properties and predictions based on those models (Tramacere et al., 2007, 2009). Recently, log-parabolic model has been recently used to describe the spectra of several jet dominated sources, as plerions (Campana et al., 2009), high frequency peaked radio sources (Maselli & Massaro, 2009), and recently Gamma-Ray Bursts (GRBs) (Massaro et al., 2010a). Making use of such a model I refined the classical SSC model and pushed it to its very limits to test it in BL Lacs flares, both in Thomson and Klein-Nishina inverse Compton regime; this model allows predictions on the correlated variability on different wavelengths. Moreover, study of spectral variations during flare allows a deeper insight on the central engine powering AGNs.

In this thesis I therefore addressed a key problem in Blazar physics, that is, their flaring activity. What does cause a Blazar flare? And how are flares related to Blazar physical features? This work aims to a search for answers to these questions.

2

Distributions of electron energies and emitted spectra

2.1 Electron energy distributions

Classical description for electron energy distribution (see Appendix A.1) is in the form of a power law

$$N(\gamma) = N_0 \left(\frac{\gamma}{\gamma_0}\right)^{-s}$$

where $\gamma = E/mc^2$ is the total adimensional electron energy. Such a distribution obtains, for example, from first order Fermi acceleration process (see Appendix A.5.2, Eq. A.49). A more refined model is provided by a distribution in the form

$$N(\gamma) = N_0 \left(\frac{\gamma}{\gamma_0}\right)^{-s-r\log\left(\frac{\gamma}{\gamma_0}\right)}, \tag{2.1}$$

where, besides the index s, we consider a curvature r (Massaro et al., 2004b); such a distribution originates from a number of acceleration processes, as shown in Sect. 2.1.1, 2.1.3. Normalization constant N_0 is related to electron density n via

$$n = \frac{d\mathcal{N}}{dV} = \int_0^\infty N(\gamma)\, d\gamma = N_0\, \gamma_0\, 10^{\frac{(s-1)^2}{4r}} \sqrt{\frac{\pi}{r}}\, \sqrt{\ln 10}\,,$$

that is,

$$N_0 = \frac{n}{\gamma_0}\, 10^{-\frac{(s-1)^2}{4r}} \sqrt{\frac{r}{\pi}}\, \frac{1}{\sqrt{\ln 10}}\,.$$

In general, a function of the form

$$f(x) = f_0 \left(\frac{x}{x_0}\right)^{-\alpha-\beta\ln\left(\frac{x}{x_0}\right)} \tag{2.2}$$

is called *log-parabola*, because in double logarithmic plot appear as a parabola, being

$$\ln\left(\frac{f(x)}{f_0}\right) = -\alpha \ln\left(\frac{x}{x_0}\right) - \beta \ln^2\left(\frac{x}{x_0}\right).$$

Function given in Eq. 2.2 reaches its maximum $f_p = f_0\, \mathrm{e}^{\frac{\alpha^2}{4\beta}}$ at $x_p = x_0\, \mathrm{e}^{-\frac{\alpha}{2\beta}}$. In general the normalization constant f_0 and the index α depend on x_0, so if we chose $x_0 = x_p$ we can write

$$f = f_p \left(\frac{x}{x_p}\right)^{-\beta\ln\left(\frac{x}{x_p}\right)}. \tag{2.3}$$

Besides the distribution given in Eq. 2.1 we can consider

$$N_k(\gamma) = \gamma^k N(\gamma)\,, \tag{2.4}$$

peaking at

$$\gamma_k = \gamma_0 10^{\frac{k-s}{2r}} ;$$

so we define

$$\gamma_p \equiv \gamma_2 = \gamma_0 10^{\frac{2-s}{2r}} , \tag{2.5}$$

$$\gamma_{3p} \equiv \gamma_3 = \gamma_0 10^{\frac{3-s}{2r}} . \tag{2.6}$$

Eq. 2.4 satisfies

$$\int_0^\infty \gamma^k N(\gamma) d\gamma = N_0 {\gamma_0}^{k+1} 10^{\frac{(s-k-1)^2}{4r}} \sqrt{\frac{\pi}{r}} \sqrt{\ln 10} ,$$

so we can calculate various momenta of the distribution

$$\langle \gamma^k \rangle = \frac{\int_0^\infty \gamma^k N(\gamma)\, d\gamma}{\int_0^\infty N(\gamma)\, d\gamma} = \gamma_0^k \, 10^{\frac{k^2-2k(s-1)}{4r}} .$$

In particular we have the electron mean energy

$$\langle \gamma \rangle = \gamma_0 10^{\frac{3-2s}{4r}} , \tag{2.7}$$

and the mean square energy

$$\langle \gamma^2 \rangle = {\gamma_0}^2 10^{\frac{2-s}{r}} ;$$

note that the root mean square (rms) energy satisfies $\sqrt{\langle \gamma^2 \rangle} = \gamma_p$.

2.1.1 Fokker-Planck equation

A log-parabolic electron energy distribution can arise from diffusion equation in the presence of systematic and stochastic acceleration processes described by Fermi acceleration (see Appendix A.5.2); in fact, the evolution of an electron distribution is described by a Fokker-Planck equation (Kaplan, 1956)

$$\frac{\partial N(E,t)}{\partial t} = -\frac{\partial}{\partial E}\left[\left(\frac{dE}{dt}\right) N\right] + \frac{\partial^2}{\partial E^2}\left[D(E,t) N\right] , \tag{2.8}$$

where $D(E,t)$ is the energy diffusion coefficient. First order Fermi acceleration process (Fermi, 1954) yields a systematic acceleration (see Eq. A.48)

$$\left\langle \frac{\Delta E}{E} \right\rangle \approx \frac{V_s}{c} ,$$

so we can write

$$\left(\frac{dE}{dt}\right)_{\rm syst} \backsimeq v\left(\frac{V_S}{c\bar{\ell}}\right) E \approx \left(\frac{V_S}{\bar{\ell}}\right) E ,$$

where $\bar{\ell}$ is the typical scale on which electrons vary their energy. Denoting

$$\lambda_1(t) = \frac{V_S}{\bar{\ell}}$$

we can write

$$\left(\frac{dE}{dt}\right)_{\rm syst} \backsimeq \lambda_1(t) E .$$

On the other hand, second order Fermi acceleration process yields a stochastic acceleration; in fact, if the electron moves with velocity v and gas clouds move with velocity V, we have (see Eq. A.46)

$$\left\langle \frac{\Delta E}{E} \right\rangle \approx \frac{4}{3}\beta^2 ;$$

so, if $v \approx c$ and ℓ is the typical cloud size, we have

$$\left(\frac{dE}{dt}\right)_{\rm stoch} \backeq v \, \frac{\langle \Delta E \rangle}{E} \, \frac{E}{\ell} \approx \left(\frac{V^2}{c\ell}\right) E \, ,$$

while the energy diffusion coefficient is

$$D(E,t) = v \frac{\left\langle \Delta E^2 \right\rangle}{2\ell} \backeq \frac{v^3 V^2}{c^4} \frac{E^2}{2\ell} \approx \frac{V^2}{2c\ell} E^2 \, .$$

Denoting

$$\lambda_2(t) = \frac{V^2}{2c\ell}$$

we can write

$$\left(\frac{dE}{dt}\right)_{\rm stoch} \approx 2\lambda_2(t) E,$$
$$D(E,t) \backeq \lambda_2(t) E^2 \, .$$

So Eq.2.8 can be rewritten as

$$\frac{\partial N(\gamma,t)}{\partial t} = \lambda_2(t) \frac{\partial}{\partial \gamma} \left(\gamma^2 \frac{\partial N}{\partial \gamma} \right) - \lambda_1(t) \frac{\partial}{\partial \gamma} \left(\gamma N \right) \, , \tag{2.9}$$

where λ_1 is the systematic acceleration rate and λ_2 is the stochastic acceleration rate; as shown by Kardashev (1962) the solution of this equation for an initially monoenergetic electron distribution is a log-parabola. In fact, if we have

$$N(\gamma, 0) = n \, \delta \left(\gamma - \gamma_0 \right) \, ,$$

we can obtain, as shown in Appendix B.1,

$$N(\gamma,t) = \frac{1}{2\sqrt{\pi}} \frac{n}{\gamma_0} \frac{1}{\sqrt{\Lambda_2}} \mathrm{e}^{-\frac{(\Lambda_1+\Lambda_2)^2}{4\Lambda_2}} \left(\frac{\gamma}{\gamma_0} \right)^{-\frac{1}{2}\left(1-\frac{\Lambda_1}{\Lambda_2}\right) - \frac{\ln 10}{4\Lambda_2} \log\left(\frac{\gamma}{\gamma_0}\right)} \, , \tag{2.10}$$

where

$$\Lambda_1(t) = \int^t \lambda_1(t') \, dt' \, ,$$
$$\Lambda_2(t) = \int^t \lambda_2(t') \, dt' \, .$$

Comparing Eq. 2.10 with Eq. 2.1 we can identify

$$s = \frac{1}{2}\left(1 - \frac{\Lambda_1}{\Lambda_2}\right) ,$$
$$r = \frac{\ln 10}{4\Lambda_2},$$
$$N_0 = \frac{1}{2\sqrt{\pi}} \frac{n}{\gamma_0} \frac{1}{\sqrt{\Lambda_2}} \, \mathrm{e}^{-\frac{(\Lambda_1+\Lambda_2)^2}{4\Lambda_2}} \, .$$

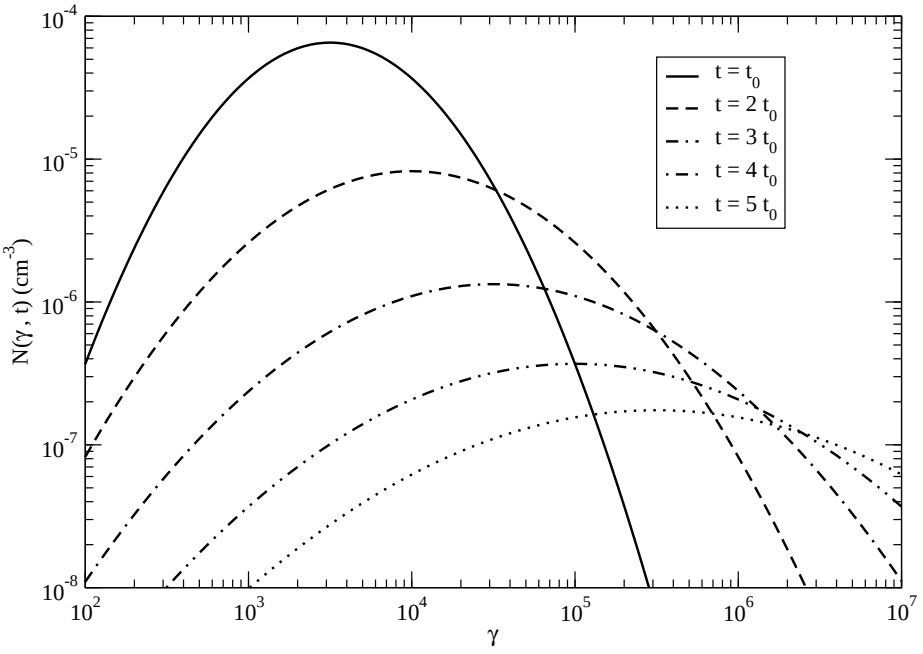

Figure 2.1: Electron energy distribution as given in Eq. 2.10 at different times t for $\Lambda_1(t) = \lambda_1 t$, $\Lambda_2(t) = \lambda_2 t$, $\lambda_1 > \lambda_2$.

While the peak of this distribution may shifts to higher or lower energies depending on relative strength of acceleration, being

$$\gamma_{max} = \gamma_0 \, \mathrm{e}^{\Lambda_1 - \Lambda_2} \,,$$

curvature s irreversibly decreases under the effect of stochastic acceleration, as shown in Fig. 2.1.

Electron energy losses by adiabatic expansion (at a constant rate) can be accounted for by adding to the Fokker-Planck equation a negative term that combines with the systematic acceleration rate into an overall coefficient $\lambda_1 \rightarrow \lambda_1 - \frac{1}{t}$, with the size of the source growing as $R \propto t$ (Kardashev, 1962).

2.1.2 Radiative cooling

It is possible to obtain analytical solutions for Eq. 2.9 in presence of radiative cooling processes causing energy losses that can be expressed in the form $\frac{dE}{dt} \propto \gamma^2$, such as synchrotron emission (see Eq. A.12)

$$\left(\frac{dE}{dt}\right)_{\mathrm{sync}} = -\frac{4}{3}\sigma_T c \beta^2 \gamma^2 \varepsilon_B \,,$$

or inverse Compton radiation in the Thomson regime (see Eq. A.35)

$$\left(\frac{dE}{dt}\right)_{\mathrm{IC}} = -\frac{4}{3}\,\sigma_T\,\gamma^2\,\beta^2\,c\,\varepsilon_\nu \,.$$

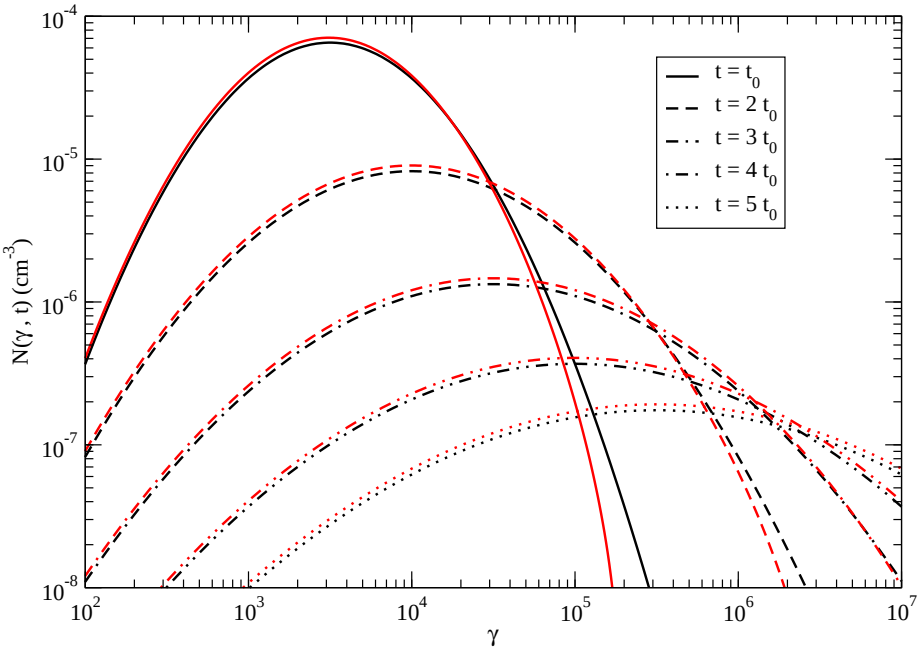

Figure 2.2: Comparison between electron energy distribution with (red lines) and without (black line) radiative cooling, according to Eq. 2.11, at different times t for $\Lambda_1(t) = \lambda_1 t$, $\Lambda_2(t) = \lambda_2 t$, $\lambda_1 > \lambda_2$.

with radiation energy density ε_ν not depending on γ (like for example in the EC process). In general, if we have

$$\frac{dE}{dt} = -\xi(t)\, m\, c^2\, \gamma^2$$

we can rewrite Eq. 2.9 as

$$\frac{\partial N(\gamma,\, t,)}{\partial t} = \lambda_2(t)\frac{\partial}{\partial \gamma}\left(\gamma^2 \frac{\partial N}{\partial \gamma}\right) - \lambda_1(t)\frac{\partial}{\partial \gamma}\left(\gamma N\right) + \xi(t)\frac{\partial}{\partial \gamma}\left(\gamma^2 N\right).$$

This equation can be solved for λ_1, λ_2 and ξ not depending on t as shown in Appendix B.2; for $\gamma_0\, \xi/\lambda_1 \ll 1$ we obtain

$$N(\gamma, t) \approx N_0 \left(\frac{\gamma}{\gamma_0}\right)^{-s-r\log\left(\frac{\gamma}{\gamma_0}\right)} \left[1 + q\left(1 - \frac{\gamma}{\langle\gamma\rangle}\right)\right], \tag{2.11}$$

where $\langle\gamma\rangle$ is defined by Eq. 2.7 and $q = \gamma_0\, \xi/2\, \lambda_2$. As shown in Fig. 2.2, the effect of radiative cooling is to move high energy electrons to lower energies, resulting in an increased curvature and a steepened electron distribution at high energies; on the other hand, $\langle\gamma\rangle$ increases with time for $\Lambda_1 > \Lambda_2$, and so in this case the deviations from Eq. 2.10 move to higher and higher energies.

Note that q is essentially the ratio between the stochastic acceleration time $t_2 = 1/\lambda_2$ and the cooling

time $t_{\rm cool} = 1/(\gamma_0\,\xi)$; for example, if we have synchrotron and IC radiative cooling we have

$$\frac{1}{t_{\rm cool}} = \frac{4}{3}\frac{\sigma_T\, c\beta^2\,\gamma_0\,\varepsilon_B}{mc^2} + \frac{4}{3}\frac{\sigma_T\, c\beta^2\,\gamma_0\,\varepsilon_\nu}{mc^2} = \frac{1}{t_S} + \frac{1}{t_C}\,.$$

2.1.3 Statistical acceleration

Log parabolic electron energy distribution can arise in a statistical acceleration scenario, as proposed by Massaro et al. (2004b); if we discretize electron energies γ_n, acceleration increase their energy by a factor independent on energy

$$\frac{\gamma_n}{\gamma_{n-1}} = \varepsilon\,, \tag{2.12}$$

and we express the probability p for an electron to be accelerated by a factor ε as a power law $p = \varepsilon^\rho$.

If p does not depend on energy, we have

$$N(>\gamma_n) = pN(>\gamma_{n-1}) = \cdots = n\,p^n = n\,\varepsilon^{n\rho} = n\left[\left(\frac{\gamma_n}{\gamma_{n-1}}\right)\left(\frac{\gamma_{n-1}}{\gamma_{n-2}}\right)\cdots\left(\frac{\gamma_1}{\gamma_0}\right)\right]^\rho = n\left(\frac{\gamma_n}{\gamma_0}\right)^\rho,$$

and so the electron differential energy distribution is a power law

$$N(\gamma_n) = \frac{dN(>\gamma_n)}{d\gamma_n} = \frac{n}{\gamma_0}\rho\left(\frac{\gamma_n}{\gamma_0}\right)^{-(1-\rho)}.$$

If p depends on energy as

$$p_n = \frac{g}{{\gamma_n}^q}\,, \tag{2.13}$$

where g and q are positive constants. Electron integrated energy distribution will therefore be

$$N(>\gamma_n) = p_{n-1}N(>\gamma_{n-1}) = \cdots = n\prod_{i=0}^{n} p_i = n\,\frac{g^n}{\left(\prod_{i=0}^{n}\gamma_i\right)^q} =$$

$$= n\,\frac{g^n}{\left({\gamma_0}^n\prod_{i=0}^{n}\varepsilon^i\right)^q} = n\,\frac{g^n}{\left({\gamma_0}^n\varepsilon^{n\frac{(n-1)}{2}}\right)^q} = n\left(\frac{g}{{\gamma_0}^q}\right)^n\varepsilon^{-qn\frac{(n-1)}{2}}.$$

From Eq. 2.12 we obtain

$$\varepsilon^n = \frac{\gamma_n}{\gamma_0} \Longrightarrow n = \frac{\log\left(\frac{\gamma_n}{\gamma_0}\right)}{\log\varepsilon}\,,$$

and so

$$N(>\gamma_n) = n\left(\frac{\gamma_n}{\gamma_0}\right)^{\frac{q}{2}+\frac{\log\left(\frac{g}{{\gamma_0}^q}\right)}{\log\varepsilon}-\frac{q}{2}\frac{1}{\log\varepsilon}\log\left(\frac{\gamma_n}{\gamma_0}\right)}.$$

Differential energy distribution will therefore be

$$N(\gamma_n) = \frac{n}{\gamma_0}\left[\frac{q}{2} + \frac{\log\left(\frac{g}{{\gamma_0}^q}\right)}{\log\varepsilon} - q\frac{1}{\log\varepsilon}\log\left(\frac{\gamma_n}{\gamma_0}\right)\right]\left(\frac{\gamma_n}{\gamma_0}\right)^{\frac{q}{2}+\frac{\log\left(\frac{g}{{\gamma_0}^q}\right)}{\log\varepsilon}-1-\frac{q}{2}\frac{1}{\log\varepsilon}\log\left(\frac{\gamma_n}{\gamma_0}\right)},$$

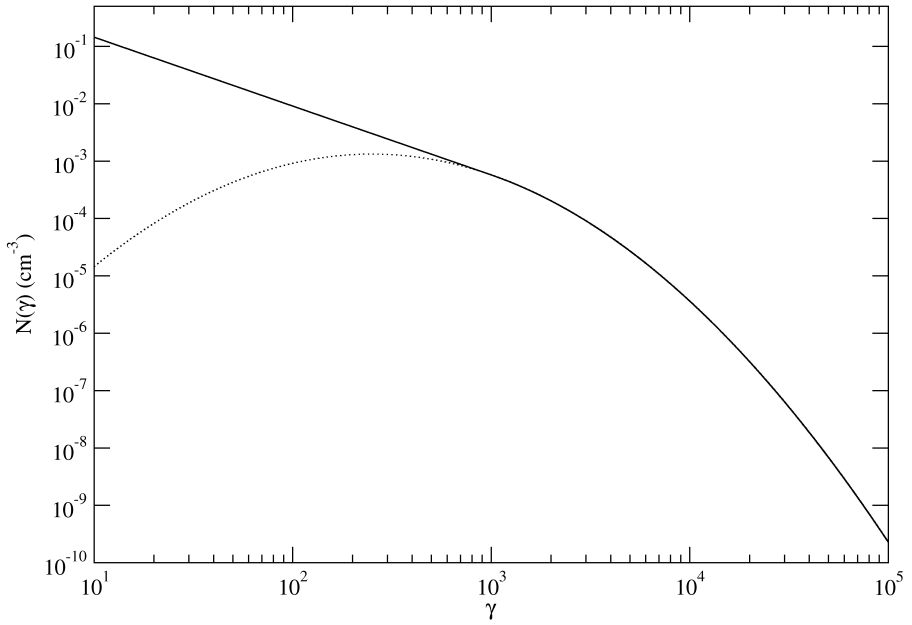

Figure 2.3: Comparison between the electron energy distribution given by Eq. 2.14 (full line) and that given by Eq. 2.1 (dashed line).

and neglecting the weak logarithmic dependence we can write

$$N(\gamma_n) \approx \frac{n}{\gamma_0}\left[\frac{q}{2}+\frac{\log\left(\frac{g}{\gamma_0{}^q}\right)}{\log\varepsilon}\right]\left(\frac{\gamma_n}{\gamma_0}\right)^{\frac{q}{2}+\frac{\log\left(\frac{g}{\gamma_0{}^q}\right)}{\log\varepsilon}-1-\frac{q}{2}\frac{1}{\log\varepsilon}\log\left(\frac{\gamma_n}{\gamma_0}\right)}. \tag{2.14}$$

On comparing Eq. 2.14 with Eq. 2.1 we can identify

$$s = 1-\frac{q}{2}-\frac{\log\left(\frac{g}{\gamma_0{}^q}\right)}{\log\varepsilon},$$
$$r = \frac{q}{2}\frac{1}{\log\varepsilon},$$
$$N_0 = \frac{n}{\gamma_0}\left[\frac{q}{2}+\frac{\log\left(\frac{g}{\gamma_0{}^q}\right)}{\log\varepsilon}\right].$$

In this framework it is also possible to obtain *asymmetric* electron energy distributions; in fact, if p

depends on energy only for $\gamma > \gamma_0$, we obtain

$$N(\gamma) = \begin{cases} N_0\left(\frac{\gamma}{\gamma_0}\right)^{-s} & \gamma \leqslant \gamma_0 \\ N_0\left(\frac{\gamma}{\gamma_0}\right)^{-s-r\log\left(\frac{\gamma}{\gamma_0}\right)} & \gamma \geqslant \gamma_0 \end{cases} . \tag{2.15}$$

Distributions described in Eq. 2.15 and 2.10 are compared in Fig. 2.3.

2.2 Log-parabolic spectra

Emission processes most relevant in Blazar sources are synchrotron and inverse Compton; as we will show in the next sections, synchrotron and inverse Compton emission from log-parabolic electron energy distributions are still log-parabolic. In general, log parabolic energy spectra can be expressed as (see Appendix A.1)

$$F_\nu = F_0\left(\frac{\nu}{\nu_0}\right)^{-a-b\log\left(\frac{\nu}{\nu_0}\right)}, \tag{2.16}$$

where ν is the photon frequency and ν_0 is a reference frequency; we can also use photon spectra in the form

$$\phi_\nu = \phi_0\left(\frac{\nu}{\nu_0}\right)^{-(a+1)-b\log\left(\frac{\nu}{\nu_0}\right)} . \tag{2.17}$$

Through Eqs. A.2 and A.4 we can express the emissivity of an optically thins, spherical source with radius R as

$$j_\nu = 3\,\frac{D^2}{R^3}\,F_\nu = j_0\left(\frac{\nu}{\nu_0}\right)^{-a-b\log\left(\frac{\nu}{\nu_0}\right)}, \tag{2.18}$$

where D is the observing distance. On the other hand the SED will be

$$S_\nu = \nu F_\nu = S_0\left(\frac{\nu}{\nu_0}\right)^{-(a-1)-b\log\left(\frac{\nu}{\nu_0}\right)};$$

such SED peaks at a frequency

$$\nu_P = \nu_0 10^{\frac{1-a}{2b}} \tag{2.19}$$

reaching a peak value

$$S_P = S_0 10^{\frac{(1-a)^2}{4b}} . \tag{2.20}$$

Using Eq. 2.3 we can write

$$S_\nu = S_P\left(\frac{\nu}{\nu_P}\right)^{-b\log\left(\frac{\nu}{\nu_P}\right)} . \tag{2.21}$$

2.2.1 Synchrotron emission

As anticipated, electron populations with a log-parabolic energy distribution emit log-parabolic synchrotron spectra; in this section we will obtain synchrotron spectral observables dependencies on source parameters. In the following primed quantities refer to the source rest frame, while unprimed quantities refer to observer frame.

For isotropically distributed synchrotron emission in a optically thin, spherical source with radius R we have, making use of the delta approximation (see Eq. A.19),

$$F'_{\nu' S} \propto \frac{R^3}{D^2}\,B\,\sqrt{\frac{\nu'}{\nu_c}}\,N\left(\sqrt{\frac{\nu'}{\nu_c}}\right),$$

where $\nu_c \propto B$. If N is given by Eq. 2.1 we have

$$F'_{\nu' S} \propto \frac{R^3}{D^2}\, B\, n\, \sqrt{r}\, 10^{-\frac{(s-1)^2}{4r}} \left(\frac{\nu'}{\nu'_0}\right)^{-\frac{(s-1)}{2}-\frac{r}{4}\log\left(\frac{\nu'}{\nu'_0}\right)},$$

where $\nu'_0 = \nu_c {\gamma_0}^2$. Taking into account beaming effects for moving sources (see Eq. A.51) and the effects of universe expansion we have

$$F_{\nu S} = F'_{\nu' S}\, \delta^3 \propto \frac{R^3}{D^2\,(1+z)}\, B\, n\, \delta^3\ \sqrt{r}\, 10^{-\frac{(s-1)^2}{4r}} \left(\frac{\nu}{\nu_0}\right)^{-\frac{(s-1)}{2}-\frac{r}{4}\log\left(\frac{\nu}{\nu_0}\right)}, \tag{2.22}$$

where $\nu_0 = \nu'_0\, \delta/(1+z)$. On comparing Eq. 2.22 with Eq. 2.16 we can identify

$$a_S = \frac{s-1}{2},$$
$$b_S = \frac{r}{4}.$$

Numerical simulations that instead of the delta approximation make use of the full Compton kernel (see Eq. A.38) yield less curved spectra with $b \approx r/5$ (Massaro et al., 2004b). The emitted bolometric flux will therefore be

$$F'_S = \int d\nu'\, F_{\nu' S} \propto \frac{R^3}{D^2}\, B^2\, \gamma_p^2\, n,$$

while the observed one will be

$$F_S \propto \frac{R^3}{D^2}\, B^2\, \gamma_p^2\, n\, \frac{\delta^4}{(1+z)^2}, \tag{2.23}$$

where γ_p is defined by Eq. 2.5.

For the emitted SED we have

$$S'_{\nu' S} = \nu' F'_{\nu'} \propto \frac{R^3}{D^2}\, B^2\, \gamma_0^2\, n\ \sqrt{r}\, 10^{-\frac{(s-1)^2}{4r}} \left(\frac{\nu'}{\nu'_0}\right)^{-\frac{(s-3)}{2}-\frac{r}{4}\log\left(\frac{\nu'}{\nu'_0}\right)},$$

while the observed SED will be, according to Eq. A.52,

$$S_{\nu S} \propto \frac{R^3}{D^2\,(1+z)^2}\, B^2\, \gamma_0^2\, n\, \delta^4\ \sqrt{r}\, 10^{-\frac{(s-1)^2}{4r}} \left(\frac{\nu}{\nu_0}\right)^{-\frac{(s-3)}{2}-\frac{r}{4}\log\left(\frac{\nu}{\nu_0}\right)}, \tag{2.24}$$

peaking at a frequency (see Eq. 2.19)

$$\nu_S = \nu_0 10^{\frac{3-s}{r}}\, \frac{\delta}{1+z} = \nu_c {\gamma_p}^2 10^{\frac{1}{r}}\, \frac{\delta}{1+z} = \nu_c {\gamma_{3p}}^2\, \frac{\delta}{1+z}, \tag{2.25}$$

where γ_{3p} is defined by Eq. 2.6. On using Eq. 2.20 we obtain for the SED peak

$$S \propto \frac{R^3}{D^2}\, B^2\, \gamma_p^2\, n\, \delta^4\ \sqrt{r}. \tag{2.26}$$

Note that $S \propto \sqrt{r}\, F_S$, so the SED peak value is closely proportional to the total flux.

To sum up, we have for the synchrotron SED peak flux

$$\boxed{S \propto R^3\, B^2\, \gamma_p^2\, n\, \frac{\delta^4}{(1+z)^2}}, \tag{2.27}$$

while the SED peak frequency will be

$$\boxed{\nu_S \propto B\, {\gamma_p}^2\, 10^{\frac{1}{r}}\, \frac{\delta}{1+z}}. \tag{2.28}$$

2.2.2 Synchrotron-self Compton radiation

We now proceed to obtain how spectral observables for the SSC SED depend on source parameters (see Appendix A.4.3).

We start to examine the SSC process in the Thomson regime: we recall that the IC emitted power by an electron with energy γmc^2 (see Eq. A.35) is

$$P_{\rm C} = \frac{4}{3} c \sigma_T \gamma^2 \beta^2 \varepsilon_{\widetilde{\nu}'}$$

where $\varepsilon_{\widetilde{\nu}'}$ is the photon energy density; we have

$$P_{\rm C} = \frac{d(h\nu')}{dt},$$
$$c\,\sigma_T\,\varepsilon_{\widetilde{\nu}'} = h\widetilde{\nu}'\,\dot{N}'_\nu\,,$$

where ν' is the frequency of the scattered photons and $\dot{N}'_\nu$ is the number of scattered photons per time unit. So we can conclude that the mean energy of the scattered photons is (Longair, 1997)

$$\bar{\nu}' = \frac{4}{3}\gamma^2\beta^2\widetilde{\nu}'\,.$$

Looking at Eq. 2.25 we can conclude that the majority of the synchrotron power is radiated by electrons with energy $\gamma_{3p}\,m\,c^2$ (Tavecchio et al., 1998), while synchrotron emission is dominated by photons with frequency $\nu'_S = \nu_c\gamma_{3p}^2$ (see Eq. 2.25). We can so conclude that SSC power will be dominated by photons produced by IC scattering of electrons with energy $\gamma_{3p}mc^2$, with photons with frequency ν_S, that is

$$\nu_{p\,C} \approx \frac{4}{3}\gamma_{3p}^2\nu_{p\,S} = \frac{4}{3}\nu_c\gamma_{3p}^4\,;$$

we can therefore write

$$\frac{dP}{d\nu} \approx P_C\,\delta\left(\nu - \frac{4}{3}\gamma^2\nu_{PS}\right).$$

The IC emissivity will be

$$j'_{\nu'\,C} = \int d\gamma\,N(\gamma)\,\frac{dP'}{d\nu'} \approx \frac{4}{3}\,c\,\beta^2\,\sigma_T\varepsilon_{\widetilde{\nu}'}\int d\gamma\,N(\gamma)\,\gamma^2\,\delta\left(\nu' - \frac{4}{3}\gamma^2\nu'_{p\,S}\right). \tag{2.29}$$

If $\varepsilon_{\widetilde{\nu}'}$ is given by synchrotron radiation from a log-parabolic electron distribution (see Eq. 2.22) in an optically thin, spherical source with radius R we have, on using Eq. A.6

$$\varepsilon_{\widetilde{\nu}'} \propto R\,B^2\,n\,\gamma_0^2 10^{\frac{2-s}{r}}\,,$$

and so Eq. A.43 will give us

$$j'_{\nu'\,C} \propto R\,B\,n^2\,\sqrt{r}\,10^{-\frac{1}{r}}\,10^{-\frac{(s-1)^2}{4r}}\left(\frac{\nu'}{\widehat{\nu}'_0}\right)^{-\frac{(s-1)}{2}-\frac{r}{4}\log\left(\frac{\nu'}{\widehat{\nu}'_0}\right)},$$

where $\widehat{\nu}'_0 = 4/3\,{\gamma_0}^2\nu'_{p\,S} = 4/3\,\nu_c{\gamma_0}^4 10^{\frac{3-s}{r}}$. On using Eqs. A.4 and A.2 we have

$$F'_{\nu'\,C} \propto \frac{R^4}{D^2}\,B\,n^2\,\sqrt{r}\,10^{-\frac{1}{r}}\,10^{-\frac{(s-1)^2}{4r}}\left(\frac{\nu'}{\widehat{\nu}'_0}\right)^{-\frac{(s-1)}{2}-\frac{r}{4}\log\left(\frac{\nu'}{\widehat{\nu}'_0}\right)},$$

where D is the observing distance; on considering beaming effects due to a moving source and effects of universe expansion (see Eq. A.51) we have for the observed flux

$$F_{\nu C} \propto \frac{R^4}{D^2}\, B\, n^2\, \frac{\delta^3}{1+z}\, \sqrt{r}\, 10^{-\frac{1}{r}}\, 10^{-\frac{(s-1)^2}{4r}} \left(\frac{\nu}{\widehat{\nu}_0}\right)^{-\frac{(s-1)}{2}-\frac{r}{4}\log\left(\frac{\nu}{\widehat{\nu}_0}\right)}. \tag{2.30}$$

where $\widehat{\nu}_0 = \widehat{\nu}'_0\, \frac{\delta}{1+z}$. On comparing Eq. 2.30 with Eq. 2.16 we can identify

$$a_C = \frac{s-1}{2}\,,$$
$$b_C = \frac{r}{4}\,.$$

Again, numerical simulations involving the full Compton kernel yield less curved spectra, that is, $b_C \approx r/10$. As usual the bolometric flux will be

$$F_C \propto \frac{R^4}{D^2}\, B^2\, \gamma_p^4\, n^2\, \frac{\delta^4}{(1+z)^2}\,. \tag{2.31}$$

On the other hand the emitted SED will be

$$S'_{\nu' C} = \nu' F'_{\nu' C} \propto \frac{R^4}{D^2}\, B^2\, \gamma_0^4\, n^2\, \sqrt{r}\, 10^{\frac{2-s}{r}}\, 10^{-\frac{(s-1)^2}{4r}} \left(\frac{\nu'}{\widehat{\nu}'_0}\right)^{-\frac{(s-3)}{2}-\frac{r}{4}\log\left(\frac{\nu'}{\widehat{\nu}'_0}\right)},$$

while the observed SED, according to Eq. A.52, will be

$$S_{\nu C} \propto \frac{R^4}{D^2}\, B^2\, \gamma_0^4\, n^2\, \frac{\delta^4}{(1+z)^2}\, \sqrt{r}\, 10^{\frac{2-s}{r}}\, 10^{-\frac{(s-1)^2}{4r}} \left(\frac{\nu}{\widehat{\nu}_0}\right)^{-\frac{(s-3)}{2}-\frac{r}{4}\log\left(\frac{\nu}{\widehat{\nu}_0}\right)}, \tag{2.32}$$

peaking at frequency

$$\nu_{pC} = \widehat{\nu}_0\, 10^{\frac{3-s}{r}} = \frac{4}{3}\, \nu_c\, \gamma_p^4\, \frac{\delta}{1+z}\, 10^{\frac{2}{r}} = \frac{4}{3}\, \nu_c\, \gamma_{3p}^4\, \frac{\delta}{1+z}\,, \tag{2.33}$$

where it reaches a peak value of

$$C \propto \frac{R^4}{D^2}\, B^2\, \gamma_p^4\, n^2\, \frac{\delta^4}{(1+z)^2}\, \sqrt{r}\,, \tag{2.34}$$

again proportional to Eq. 2.31.

To sum up, we have for the SSC SED in Thomson regime we have a peak flux

$$\boxed{C \propto R^4\, B^2\, \gamma_p^4\, n^2\, \frac{\delta^4}{(1+z)^2}}\,, \tag{2.35}$$

attained at a peak frequency

$$\boxed{\nu_{pC} \propto B\, \gamma_p^4\, 10^{\frac{1}{r}}\, \frac{\delta}{1+z}}\,. \tag{2.36}$$

We now calculate SSC radiation in the extreme Klein-Nishina regime: using Eq. A.42 we can approximate the Compton kernel as

$$K(\nu, \widetilde{\nu}, \gamma) \propto \frac{\nu}{\gamma^2}\, \delta\left(\gamma - \frac{h\nu}{mc^2}\right).$$

Again, if we consider synchrotron emission from a log-parabolic electron energy distribution in an optically thin, spherical source with radius R, we can write Eq. A.43 as

$$j'_{\nu' C} \propto R\, B\, \frac{1}{\gamma_0}\, n^2\ \sqrt{r}\, 10^{-\frac{(s-1)^2}{4r}} \left(\frac{\nu'}{\widehat{\nu'}_0}\right)^{-s-r\log\left(\frac{\nu'}{\widehat{\nu'}_0}\right)},$$

where $\widehat{\nu'}_0 = \gamma_0\, m\, c^2/h$. The emitted spectrum of SSC radiation will therefore be

$$F'_{\nu' C} \propto \frac{R^4}{D^2}\, B\, \frac{1}{\gamma_0}\, n^2\ \sqrt{r}\, 10^{-\frac{(s-1)^2}{4r}} \left(\frac{\nu'}{\widehat{\nu'}_0}\right)^{-s-r\log\left(\frac{\nu'}{\widehat{\nu'}_0}\right)},$$

where D is the observing distance, and taking into account beaming effects and universe expansion effects we have for the observed spectra

$$F_{\nu C} \propto \frac{R^4}{D^2}\, B\, \frac{1}{\gamma_0}\, n^2\, \frac{\delta^3}{1+z}\ \sqrt{r}\, 10^{-\frac{(s-1)^2}{4r}} \left(\frac{\nu}{\widehat{\nu}_0}\right)^{-s-r\log\left(\frac{\nu}{\widehat{\nu}_0}\right)}. \tag{2.37}$$

On comparing Eq. 2.37 with Eq. 2.16 we can identify

$$a_C = s\,,$$
$$b_C = r\,.$$

The observed bolometric flux will be

$$F_C = \int d\nu\, F_{\nu C} \propto \frac{R^4}{D^2}\, B\, n^2\, \frac{\delta^4}{(1+z)^2}\,. \tag{2.38}$$

On the other hand, the emitted SED will be

$$S'_{\nu' C} \propto \frac{R^4}{D^2}\, B\, n^2\ \sqrt{r}\, 10^{-\frac{(s-1)^2}{4r}} \left(\frac{\nu'}{\widehat{\nu'}_0}\right)^{-(s-1)-r\log\left(\frac{\nu'}{\widehat{\nu'}_0}\right)}.$$

while the observed SED will be, according to Eq. A.52

$$S_{\nu C} \propto \frac{R^4}{D^2}\, B\, n^2\, \frac{\delta^4}{(1+z)^2}\ \sqrt{r}\, 10^{-\frac{(s-1)^2}{4r}} \left(\frac{\nu}{\widehat{\nu}_0}\right)^{-(s-1)-r\log\left(\frac{\nu}{\widehat{\nu}_0}\right)}, \tag{2.39}$$

peaking at

$$\nu_C = \widehat{\nu}_0 10^{\frac{1-s}{2r}} = \frac{mc^2}{h}\gamma_p 10^{-\frac{1}{2r}}\, \frac{\delta}{1+z} = \frac{mc^2}{h}\gamma_{3p} 10^{-\frac{1}{r}}\, \delta 1+z\,, \tag{2.40}$$

where the SED attains the peak value

$$C \propto \frac{R^4}{D^2}\, B\, n^2\, \frac{\delta^4}{(1+z)^2}\ \sqrt{r}\,, \tag{2.41}$$

again proportional to Eq. 2.38.

So, for the SSC SED in the extreme Klein-Nishina regime we have a peak flux

$$\boxed{C \propto R^4\, B\, n^2\, \frac{\delta^4}{(1+z)^2}}\,, \tag{2.42}$$

attained at a peak frequency

$$\boxed{\nu_C \propto \gamma_p \, 10^{-\frac{1}{2r}} \, \frac{\delta}{1+z}} \, . \tag{2.43}$$

To conclude we can evaluate a threshold for the peak frequency of the synchrotron SED when the transition between the two IC regimes occurs, that is, when

$$2\gamma_{3p} \, h \, \nu'_S \approx m \, c^2 \, ,$$

to yield

$$\nu_T \approx 7.15 \, 10^{15} \left(\frac{B}{0.1 \text{ G}} \right)^{\frac{1}{3}} \left(\frac{\delta}{10} \right) (1+z)^{-1} \text{ Hz} \, , \tag{2.44}$$

or equivalently

$$\nu_T \approx 1.96 \, 10^{16} \left(\frac{\gamma_p}{10^4} \right)^{-1} 10^{\frac{1}{2}\left(1-\frac{1}{5b}\right)} \left(\frac{\delta}{10} \right) (1+z)^{-1} \text{ Hz} \, . \tag{2.45}$$

3

Spectral correlations

3.1 Introduction

The synchrotron-self Compton (SSC) radiation process is widely held to provide a close representation of the double peaked spectral energy distributions from BL Lac Objects (BL Lacs), which are marked by non-thermal beamed radiations, highly variable on timescales of days or less. Their outbursts in the γ rays relative to the optical/X rays might be surmised to be enhanced in BL Lacs as these photons are upscattered via the inverse Compton (IC) process. In this chapter I will show how, from the observed correlations among the spectral parameters during optical/X-ray variations in BL Lac flares it is possible to predict corresponding correlations in the γ-ray band, and the actual relations between the γ-ray and the X-ray variability consistent with the SSC emission process. The homogeneous single zone (HSZ) SSC model (based, in particular, on a single electron population) constitutes an attractively simple source structure worth to be extensively tested and pushed to its very limits (Katarzyński et al., 2005; Tramacere et al., 2007). Staring from the HSZ SSC source model with the realistic log-parabolic energies distributions of the electrons radiating the synchrotron photons (Landau et al., 1986; Tanihata et al., 2004; Massaro et al., 2004a; Tramacere et al., 2007; Nieppola et al., 2006; Donnarumma et al., 2009), and upscattering them by IC in either the Thomson or the Klein Nishina (KN) regime, I find relations among spectral parameters of the IC radiation in both the Thomson (for Low energy BL Lacs) and the Klein-Nishina regimes (mainly for High energy BL Lacs); whence I will compute how variability is driven by a smooth increase of key source parameters, primarily the root mean square electron energy. In the Klein-Nishina regime the model predicts for HBLs lower inverse Compton fluxes relative to synchrotron, and milder γ-ray relative to X-ray variations. Stronger γ-ray flares observed in some HBLs like Mrk501 are understood in terms of additional, smooth increases also of the emitting electron density. However, episodes of rapid flares as recently reported at TeV energies are beyond the reach of the single component SSC model with one dominant varying parameter. Furthermore, spectral correlations at variance with these predictions, as well as TeV emissions in LBL objects (like BL Lacertae itself) cannot be explained in terms of the simple HSZ SSC model, and in these cases the source may require additional electron populations in more elaborate structures like decelerated relativistic outflows or sub-jet scenarios. These findings provide therefore a comprehensive benchmark to straightforwardly gauge the capabilities and effectiveness of the SSC radiation process. The single component SSC source model in the Thomson regime turns out to be adequate for many LBL sources. In the mild Klein-Nishina regime it covers HBL sources undergoing variations driven by smooth increase of a number of source parameters. However, the simple model meets its limits with the fast/strong flares recently reported for a few sources in the TeV range; these require sudden accelerations of emitting electrons in a second source component.

3.2 Source parameters

Let us recall the main results of the previous chapter; log-parabolic spectra are radiated by electron populations with a log-parabolic energy distribution, namely

$$N(\gamma) = N_0 \left(\frac{\gamma}{\gamma_0} \right)^{-s - r \log\left(\frac{\gamma}{\gamma_0}\right)} . \tag{3.1}$$

For the synchrotron SED we have from Eq. 2.24

$$S_\nu^s = S_0^s \left(\frac{\nu}{\nu_0}\right)^{-(a_s-1)-b_s \log\left(\frac{\nu}{\nu_0}\right)}; \tag{3.2}$$

here a_s gives the constant component of the spectral index for the energy flux and b_s is the spectral curvature. Spectral curvature values are observed to be around 0.2 (Massaro et al., 2004b) and decreasing with time and/or frequency as given by Eqs. 3.31 and 3.33 (see Sect 3.4); since the decrease is mild during flares (which are essentially dominated by systematic acceleration processes), we can consider a nearly constant spectral curvature to a first approximation. Then the scaling relations 2.27 and 2.28 may be therefore rewritten as $\nu_S \propto B\,\gamma_p^2\,\delta$ and $S \propto B^2\,\gamma_p^2\,n\,R^3\,\delta^4$.

The analogous expression for the inverse Compton radiation is given by Eq. 2.32 or Eq. 2.39

$$S_\nu^c \approx S_0^c \left(\frac{\nu}{\widetilde{\nu_0}}\right)^{-(a_c-1)-b_c \log\left(\frac{\nu}{\widetilde{\nu_0}}\right)} \tag{3.3}$$

note that in the Thomson regime the IC has *less* curved spectra with $b_c \approx b_s/2$. At nearly constant curvature Eqs. 2.35 and 2.36 may be rewritten as $\nu_C \propto B\,\gamma_p^4\,\delta$ and $C \propto B^2\,\gamma_p^4\,n^2\,R^4\,\delta^4$. In the extreme Klein-Nishina regime we have *more* curved spectra with $b_c \approx 5\,b_s$, and Eqs. 2.42 and 2.43 may be rewritten as $\nu_C \propto \gamma_p\,\delta$ and $C \propto B\,n^2\,R^4\,\delta^4$ (Massaro et al., 2008a,b).

These results are found to hold for the spectral shapes obtained with the numerical simulations outlined in Fig. 3.1, and reported in full detail in Figs. 3.7.

Using the previous scalings, with the relation $R = c\,\Delta t\,\delta/(1+z)$ between the observed variation time Δt and the size R of the emitting region (assuming spherical symmetry in the rest frame), we obtain relations to constrain the five source parameters by the five observables, that we denote with

$$S_i \equiv \frac{S}{10^i \frac{\mathrm{erg}}{\mathrm{cm^2\ s}}}, \qquad C_j \equiv \frac{C}{10^j \frac{\mathrm{erg}}{\mathrm{cm^2\ s}}}, \tag{3.4}$$

$$\nu_{S\,k} \equiv \frac{\nu_S}{10^k\ \mathrm{Hz}}, \qquad \nu_{C\,h} \equiv \frac{\nu_C}{10^h\ \mathrm{Hz}}, \tag{3.5}$$

where the indexes i, j, k, h express the normalizations as demonstrated below; in addition, we denote with Δt_d the time in days for the source variations, and with D the distance of the source in Gpc.

In the Thomson regime we find

$$B = 10^{-1} \times \left[b^{\frac{1}{8}}\, D^{-\frac{1}{2}}\, (1+z)^{\frac{1}{2}}\, {\nu_{S\,14}}^3 {C_{-11}}^{\frac{1}{4}}\, {\Delta t_d}^{\frac{1}{2}}\, {\nu_{C22}}^{-\frac{3}{2}}\, {S_{-11}}^{-\frac{1}{2}}\right] \mathrm{G} \tag{3.6}$$

$$\delta = 13.5 \times \left[D^{\frac{1}{2}}\, b^{-\frac{1}{8}}\, (1+z)^{\frac{1}{2}}\, {\nu_{C22}}^{\frac{1}{2}}\, {S_{-11}}^{\frac{1}{2}}\, {\nu_{S\,14}}^{-1}\, {C_{-11}}^{-\frac{1}{4}} {\Delta t_d}^{-\frac{1}{2}}\right] \tag{3.7}$$

$$R = 3.5\,10^{16} \times \left[D^{\frac{1}{2}}\, b^{-\frac{1}{8}}\, (1+z)^{-\frac{1}{2}}\, {\nu_{C22}}^{\frac{1}{2}}\, {S_{-11}}^{\frac{1}{2}}\, {\Delta t_d}^{\frac{1}{2}}\, {\nu_{S\,14}}^{-1}\, {C_{-11}}^{-\frac{1}{4}}\right] \mathrm{cm} \tag{3.8}$$

$$n = 5.7 \times \left[b^{\frac{1}{8}}\, D^{\frac{1}{2}}\, (1+z)^{\frac{1}{2}}\, 10^{\left(\frac{1}{5b}-1\right)}\, {\nu_{S\,14}}^2\, {C_{-11}}^{\frac{5}{4}}\, {\nu_{C22}}^{-\frac{3}{2}}\, {S_{-11}}^{-\frac{3}{2}}\, {\Delta t_d}^{-\frac{1}{2}}\right] \mathrm{cm^{-3}} \tag{3.9}$$

$$\gamma_p = 2.7\,10^3 \times \left[10^{\frac{1}{2}\left(1-\frac{1}{5b}\right)}\, {\nu_{C22}}^{\frac{1}{2}}\, {\nu_{S\,14}}^{-\frac{1}{2}}\right]. \tag{3.10}$$

In the extreme KN regime we obtain

$$B = 1.7\,10^{-2} \times \left[D^{\frac{2}{5}}\, b^{\frac{1}{10}}\, (1+z)^{-\frac{2}{5}}\, {\nu_{S\,18}}^{\frac{2}{5}}\, {S_{-10}}^{\frac{2}{5}}\, {\nu_{C26}}^{-\frac{8}{5}}\, {C_{-11}}^{-\frac{1}{5}}\, {\Delta t_d}^{-\frac{2}{5}}\right] \mathrm{G} \tag{3.11}$$

$$\delta = 4.2 \times \left[D^{\frac{2}{5}}\, b^{-\frac{1}{10}}\, 10^{\frac{4}{5}\left(\frac{1}{5b}-1\right)}\, (1+z)^{\frac{3}{5}}\, {\nu_{C26}}^{\frac{2}{5}}\, {S_{-10}}^{\frac{2}{5}}\, {\nu_{S\,18}}^{-\frac{3}{5}}\, {C_{-11}}^{-\frac{1}{5}}\, {\Delta t_d}^{-\frac{2}{5}}\right] \tag{3.12}$$

$$R = 1.1\,10^{16} \times \left[D^{\frac{2}{5}}\, b^{-\frac{1}{10}}\, 10^{\frac{4}{5}\left(\frac{1}{5b}-1\right)}\, (1+z)^{-\frac{2}{5}}\, {\nu_{C26}}^{\frac{2}{5}}\, {S_{-10}}^{\frac{2}{5}}\, {\Delta t_d}^{\frac{3}{5}}\, {\nu_{S\,18}}^{-\frac{3}{5}}\, {C_{-11}}^{-\frac{1}{5}}\right] \mathrm{cm} \tag{3.13}$$

$$\gamma_p = 6.1\,10^5 \times \left[b^{\frac{1}{10}}\, D^{-\frac{2}{5}}\, 10^{\frac{3}{10}\left(1-\frac{1}{5b}\right)}\, (1+z)^{\frac{2}{5}}\, {\nu_{S\,18}}^{\frac{3}{5}}\, {\nu_{C26}}^{\frac{3}{5}}\, {C_{-11}}^{\frac{1}{5}}\, {\Delta t_d}^{\frac{2}{5}}\, {S_{-10}}^{-\frac{2}{5}}\right] \tag{3.14}$$

$$n = 9.5\,10^2 \times \left[b^{\frac{1}{5}}\, D^{-\frac{4}{5}}\, 10^{\frac{13}{5}\left(1-\frac{1}{5b}\right)}\, (1+z)^{\frac{4}{5}}\, {\nu_{S\,18}}^{\frac{11}{5}}\, {C_{-11}}^{\frac{7}{5}}\, {\nu_{C26}}^{-\frac{4}{5}}\, {S_{-10}}^{-\frac{9}{5}}\, {\Delta t_d}^{-\frac{1}{5}}\right] \mathrm{cm^{-3}} \tag{3.15}$$

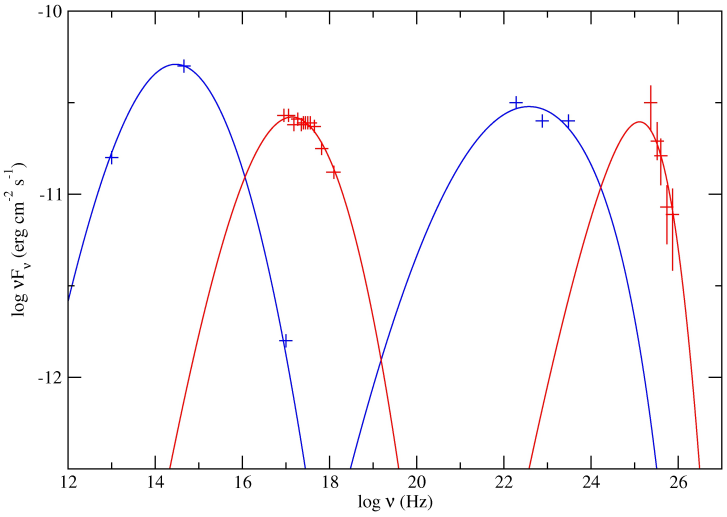

Figure 3.1: Two examples of exact, steady SEDs provided by numerical simulations (code by Massaro 2007) after the HSZ SSC model from relativistic electrons with a log-parabolic energy distribution $N(\gamma) \propto \gamma^{-s-r\log\gamma}$.The two characteristic humps correspond to synchrotron emission (left) and to inverse Compton scattering (right), either in the Thomson regime (blue line) or in the KN regime (red line). Standard sources that are so fitted include the low state of S5 0716+714 (an IBL, blue crosses) observations of November 1996 by *BeppoSAX*, AIT and EGRET (Tagliaferri et al., 2003) and 1ES 1553+113 (a HBL, red crosses) observations of April 2005 by *Swift* and April-May 2005 by MAGIC (Massaro, 2007).

Note that a delay of the order of Δt may elapse between synchrotron and IC spectral variations.

Values of physical parameters for some sources are given in Tab. 3.1. Note that the simple Eqs. (3.6) - (3.10) provide parameter values in close agreement with the ones needed to fit the observations of LBL or IBL sources in Thomson regime; on the other hand the extreme KN limit underlying Eqs. (3.11) - (3.15) would yield disagreement for HBLs, indicating that these sources just border the KN regime.

Source name	z	γ_p	$R\,(\mathrm{cm})$	$B\,(\mathrm{G})$	δ	$n\,(\mathrm{cm}^{-3})$	r
1ES 1553+113	0.25	$3.39\,10^4$	$0.64\,10^{16}$	$9.80\,10^{-1}$	10	2.04	1.49
S5 0716+714 (low state)	0.31	9.1×10^2	$2.70\,10^{16}$	$8.49\,10^{-1}$	12	$1.01\,10^2$	1.31
S5 0716+714 (high state)	,,	2.8×10^3	$6.96\,10^{15}$	3.34	19	22.7	2.10
Mrk501 (low state)	0.034	1.4×10^5	$3.53\,10^{15}$	$1.11\,10^{-1}$	15	1.07	0.82
Mrk501 (high state)	,,	1.9×10^5	$7.49\,10^{14}$	$3.68\,10^{-1}$	15	23.0	0.75
Mrk 421 (2000, low)	0.031	5.2×10^4	$2.97\,10^{16}$	$3.59\,10^{-2}$	20	$6.46\,10^{-2}$	1.52
Mrk 421 (2000, high)	,,	6.1×10^4	$2.83\,10^{16}$	$3.59\,10^{-2}$	20	$1.06\,10^{-}$	1.23
Mrk 421 (2008, low)	,,	2.5×10^4	$1.78\,10^{16}$	$1.17\,10^{-1}$	20	$4.17\,10^{-1}$	2.90
Mrk 421 (2008, high)	,,	3.4×10^4	$1.57\,10^{16}$	$1.17\,10^{-1}$	20	$4.37\,10^{-1}$	2.80

Table 3.1: Source parameters for some BL Lac sources.

We recall Eqs. 2.44 and 2.45, expressing the frequency ν_T of the synchrotron peak when the transition between the two IC regimes occurs, that is

$$\nu_T \approx 7.15\,10^{15}\left(\frac{B}{0.1\ \mathrm{G}}\right)^{\frac{1}{3}}\left(\frac{\delta}{10}\right)(1+z)^{-1}\ \mathrm{Hz}\,, \tag{3.16}$$

or equivalently

$$\nu_T \approx 1.96\,10^{16}\left(\frac{\gamma_p}{10^4}\right)^{-1}\ 10^{\frac{1}{2}\left(1-\frac{1}{5b}\right)}\left(\frac{\delta}{10}\right)(1+z)^{-1}\ \mathrm{Hz}\,. \tag{3.17}$$

So we conclude that in LBLs, which feature the synchrotron peak at optical/IR frequencies with $\nu_S \approx 10^{14}$ Hz, the majority of photons of the IC peak are upscattered in the Thomson regime; whereas in extreme HBLs, which show the synchrotron peak in the X-ray band with $\nu_S \approx 10^{18}$ Hz, the majority of IC peak photons are upscattered in the Klein-Nishina regime.

3.2.1 Spectral correlations during X-ray spectral variations

Correlations in the synchrotron emission between S and b_s with ν_S can be used to pinpoint the main *driver* of the spectral changes during X-ray variations (see also Tramacere et al. 2007). In fact, the synchrotron SED peak scales (for nearly constant spectral curvature as anticipated in Sect. 3.2) as $S \propto n\,R^3\,\gamma_p^2\,B^2\,\delta^4$ at the peak frequency itself scaling as $\nu_S \propto \gamma_p^2\,B\,\delta$.

Thus on writing the dependence of S on ν_S in the form of a powerlaw $S \propto {\nu_S}^\alpha$, we expect $\alpha = 1$ to apply when the spectral changes are driven mainly by variations of the electrons r.m.s. energy; $\alpha = 2$ for dominant changes of the magnetic field; $\alpha = 4$ if changes in the beaming factor dominate; $\alpha = \infty$ formally applies for changes only in the number density of the emitting particles. Results by the latter authors focus on γ_p and B as dominant drivers. Starting from such correlations I aim at predicting the expected correlations and flux variations in the γ-ray band.

Particle r.m.s. energy variations are of particular interest because they naturally arise as a consequence of systematic plus stochastic acceleration of the electron population (see Eq. 3.32).

3.3 γ-ray spectra

3.3.1 Spectral correlations

The above results lead us to expect specific correlations between SED peak frequencies and fluxes as follows. In the case of dominant r.m.s. particle energy variations I expect for the synchrotron emission

$$S \propto \nu_S \,, \tag{3.18}$$

while for the IC we have

$$C \propto \nu_C \tag{3.19}$$

for LBL objects, and

$$C \approx const \tag{3.20}$$

for extreme HBLs. In the case of magnetic field variations we have for the synchrotron emission

$$S \propto {\nu_S}^2 \,, \tag{3.21}$$

while for the IC we have

$$C \propto {\nu_C}^2 \tag{3.22}$$

for LBL objects, and

$$C \propto {\nu_C}^\tau \tag{3.23}$$

formally with $\tau = \infty$ for extreme HBLs.

To complete the above picture, we consider how saturation affects correlations. I have already stated in Sect. 3.2 the shapes of the spectra (synchrotron, and IC in both the Thomson and KN regimes) emitted by the distribution given in Eq. 3.1; here I stress the time dependence of their main spectral features. We can write for the synchrotron emission[1]

$$S \propto \frac{e^{2\int(\lambda_1+3\lambda_2)dt}}{\sqrt{\int \lambda_2\, dt}} \propto \gamma_p^2 \sqrt{r}, \qquad \nu_S \propto e^{2\int(\lambda_1+5\lambda_2)dt} \propto \gamma_p^2\, 10^{\frac{1}{r}} \,; \tag{3.24}$$

for IC emission we have in the Thomson regime

$$C \propto \frac{e^{4\int(\lambda_1+3\lambda_2)dt}}{\sqrt{\int \lambda_2\, dt}} \propto \gamma_p^4 \sqrt{r}, \qquad \nu_C \propto e^{4\int(\lambda_1+5\lambda_2)dt} \propto \gamma_p^4 \,, \tag{3.25}$$

and in the extreme KN regime

$$C \propto \frac{1}{\sqrt{\int \lambda_2\, dt}} \propto \sqrt{r}, \qquad \nu_C \propto e^{\int(\lambda_1+\lambda_2)dt} \propto \gamma_p\, 10^{-\frac{1}{2r}}. \tag{3.26}$$

If the total energy available to the jet is limited we expect that $\int dt\, \lambda_1$ and $\int dt\, \lambda_2$ cannot grow indefinitely, but are to attain a *limiting* value. At low energies where $\int dt\, \lambda_1 \gg \int dt\, \lambda_2$ holds, we have $S \propto \nu_S$ and $C \propto \nu_C$ as before; at higher energies when $\int dt\, \lambda_1$ reaches its limit, $\int dt\, \lambda_1 \ll \int dt\, \lambda_2$ holds, leading to $S \propto {\nu_S}^{0.6}$ and $C \propto {\nu_C}^{0.6}$. Eventually also $\int dt\, \lambda_2$ reaches its limit, and both the fluxes and the peak frequencies cannot grow any more. The data analyses by Tramacere et al. (2007; 2009) for

[1] Note that singular behaviors of S and C for $t = 0$ are a consequence of the (differential) definition of the SED as νF_ν, and relate to the initial singularity of the particle energy distribution. Integrated quantities like $F = \int d\nu\, F_\nu$ behave regularly.

the variations of Mrk501 are consistent with the beginning of such a saturation effect, as they show a declining value of α when the peak moves toward the highest energies and approaches $L \approx 10^{46}$ erg s^{-1}.

To conclude this discussion on saturation effects, I briefly discuss the issue of total limiting power: denoting the total number of particles with N_T, in the jet frame we have for the synchrotron luminosity $L_s \propto N_T\,\gamma_p^2$, while for IC luminosity we have $L_C \propto \left(N_T\,\gamma_p^2\right)^2$ and $L_C \propto N_T^2$ in Thomson and KN regime, respectively. Consider the case where the total power available to the jet is limited, e. g., in the BZ mechanism (Blandford & Znajek, 1977) of power extraction from a maximally rotating black hole with an extreme, radiation pressure dominated disk that holds the pressure of the magnetic field facing the black hole horizon (see discussion by Cavaliere & D'Elia, 2002, and references therein). Then the power has an upper bound $L_{BZ} \approx 2\,10^{45} M_9$ erg s^{-1}; as a consequence, we expect an effect of saturation on the SED peaks as the emitted power, which represents a substantial fraction of the total jet power (see Celotti & Ghisellini, 2008), approaches L_{BZ}. For the total power, including radiative, kinetic and magnetic components, $L_{tot} \approx L_{BZ}$ we envisage $N_T \sim \gamma_p^{-2}$, that is, the particles effectively accelerated to the increasing γ_p decrease in number on approaching the BZ limit. Such an effect will be discussed in detail in the next Chapter.

3.3.2 Related variabilities

We now focus on related variabilities between IC and synchrotron fluxes; here we are mainly interested on increases of peak frequencies and fluxes, as driven by acceleration processes of the emitting particles or by a growing magnetic field (see also Katarzyński et al., 2005); in Sect. 3.5 I will briefly discuss the problems posed by the decay phase as stressed by Katarzyński et al.

For LBLs, that radiate mostly in the Thomson regime, we predict from Eqs. (3.18) - (3.23) a quadratic or linear variation of C with respect to S, depending on the parameter that mainly drives source variations. That is to say, we expect

$$\Delta \ln C \approx 2\,\Delta \ln S \tag{3.27}$$

in the case of dominant particle r.m.s. energy variations, or

$$\Delta \ln C \approx \Delta \ln S \tag{3.28}$$

for dominant magnetic field variations (see also Figs. 3.2 and 3.4).

Instead, for HBLs that radiate closer to the Klein-Nishina regime, we obtain a weaker γ-ray variability due to the decreasing KN cross section, leading in the extreme to

$$\Delta \ln C \approx 0 \tag{3.29}$$

in case of dominant particle r.m.s. energy variations, or

$$\Delta \ln C \approx \frac{1}{2}\,\Delta \ln S \tag{3.30}$$

for dominant magnetic field variations. Expected correlations are summarized in Table 3.2.

From Figs. 3.2 and 3.4 it is seen that the transition to the KN regime has three effects on the IC spectrum: first, it *brakes* the peak frequency increase, because the energy the photon can gain is limited to the total electron energy $\gamma\, m\, c^2$; second, it *reduces* the flux increase at the SED peak, as a consequence of reduced cross section; third, it *increases* the spectral curvature near the peak as a consequence of frequency compression.

Viceversa, variations observed in IC section of the spectrum are related via Eqs. (3.27) - (3.30) to variations expected in the synchrotron emission; in particular, in HBLs γ-ray variations ought to have enhanced counterparts in X rays.

Up to now Figs. 3.2 and 3.4 may be interpreted as a collection of different sources or of unrelated states of a single source; henceforth I will focus on the interpretation in terms of *evolution* in a flaring source where the parameters vary in a continuous fashion; in particular, γ_p increases under the drive of systematic and stochastic electron accelerations, in keeping with the description in terms of a continuity or kinetic equation of the Fokker-Planck type. Signatures of such an evolution are provided not only by continuous growth of the peak frequencies, but even more definitely by the *irreversible* decrease of the spectral curvature (in terms of time or frequency) under the drive of the stochastic acceleration, see Eq. 3.33 and the observations by Tramacere et al. (2007; 2009). In fact, for a single electron population the curvature is to slowly decrease or stay nearly constant on the timescale of the systematic acceleration. So a sudden increase of curvature signals the injection of a new population/component.

In the following I will neglect radiative cooling, which does not strongly affect the spectral shape around the peaks; such a process will be particularly relevant when the source, after flaring up, relaxes back to a lower state upon radiating away its excess energies from high frequencies downwards (see Eq. 2.11).

process	peak flux and frequency	flux-frequency correlation	$S - C$ correlation
synchrotron	$S \propto R^3 B^2 \gamma_p^2 n \delta^4$ $\nu_S \propto B \gamma_p^2 \delta$	$S \propto {\nu_S}^\alpha \begin{cases} \alpha = 1 \ (\gamma_p) \\ \alpha = 2 \ (B) \end{cases}$	
IC Thomson	$C \propto R^4 B^2 \gamma_p^4 n^2 \delta^4$ $\nu_C \propto B \gamma_p^4 \delta$	$C \propto {\nu_C}^\alpha \begin{cases} \alpha = 1 \ (\gamma_p) \\ \alpha = 2 \ (B) \end{cases}$	$C \propto S^2$ $C \propto S$
IC KN	$C \propto R^4 B n^2 \delta^4$ $\nu_C \propto \gamma_p \delta$	$C \propto {\nu_C}^\alpha \begin{cases} \alpha = 0 \ (\gamma_p) \\ \alpha = \infty \ (B) \end{cases}$	$C \approx const$ $C \propto S^{1/2}$

Table 3.2: Spectral correlations (for $r \backsimeq const$). We have denoted with (γ_p) or (B) the variations driven by increases of rms electron energy or magnetic field, respectively.

3.3.3 Specific sources

I have applied the above simple expectations to three sources, Mrk501, Mrk 421 (HBLs) and S5 0716+714 (IBL), among the few to date to provide extended simultaneous coverage of two different source states in X rays and γ rays.

For the HBL source Mrk501 I consider the two states described by Massaro et al. (2006), with simultaneous *BeppoSAX* and CAT observations of April 7 and 16 1997. For Mrk 421 I consider low and high states in 2000 from BeppoSAX and HEGRA data (Konopelko et al., 2003), and multi-wavelength observations performed with GASP-WEBT, *RXTE*/ASM, *Swift*, SuperAGILE, *AGILE*-GRID, ARGO-YBJ, and VERITAS in June 2008 (Donnarumma et al., 2009; Di Sciascio et al., 2010). To understand the behavior of this sources, from Figs. 3.3 and 3.5 it is seen that variations of B alone are ineffective and require complementary n increase by a factor of about 30; variations of γ_p are adequate in the KN regime, and only require a complementary doubling of n (which by itself would yield $\Delta \ln C \approx 2 \Delta \ln S$ in both scattering regimes) to yield higher γ-ray flux increase. Note that in going to higher energies the spectral curvature *decreases* somewhat (from $b = 0.161 \pm 0.007$ to $b = 0.148 \pm 0.005$ for the low and high state of Mrk 501, respectively, and from $b = 0.291 \pm 0.005$ to $b = 0.190 \pm 0.007$ for the low and high state of Mrk 421 in 2008, respectively) in keeping with model predictions; such a behavior is interesting as it marks a *smooth* growth, if anything, in the number of emitting particles as contrasted with sudden, substantial re-injection of nearly monoenergetic electrons that would suddenly *reverse* the otherwise *irreversible* decrease of r and b. Such a smooth growth may obtains in a scenario of an expanding blast-wave that progressively involves more electrons (see, e. g., Ostriker & McKee, 1988; Lapi et al., 2005; Vietri, 2006).

The source S5 0716+714 is widely considered to be an IBL. In the low state observed by Automatic

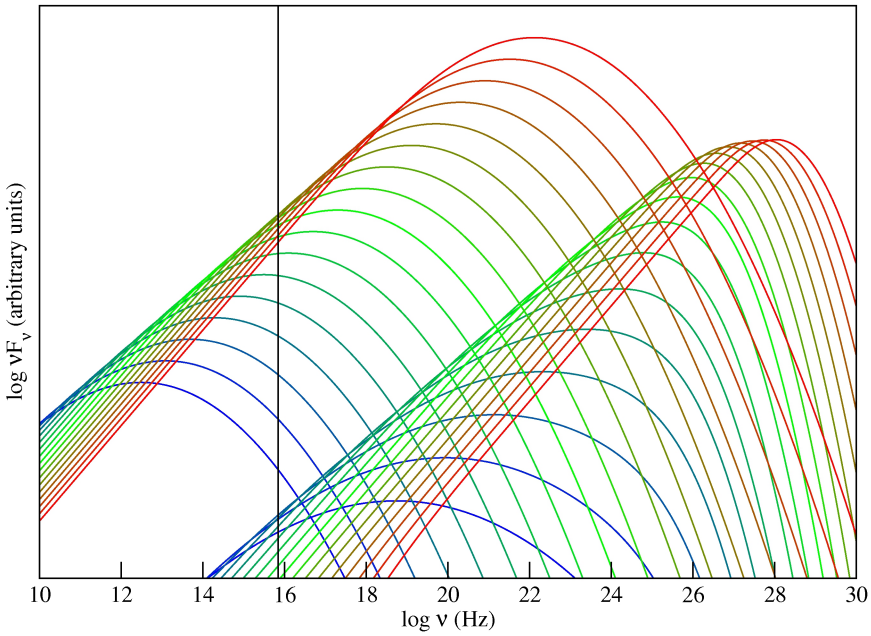

Figure 3.2: To illustrate the differences of the IC SEDs in the Thomson and in the extreme KN regime, we show the results of numerical simulations (code by Massaro, 2007) after the HSZ SSC model, for different sources with larger and larger r.m.s. energy of the radiating particles and other parameters kept constant (including the curvature of the particle energy distribution). The vertical line indicates the frequency of the synchrotron peak where the IC scattering changes over the Thomson to the KN regime (see Eq. 3.16). Actual sources in their evolution (represented in Fig. 3.7) vary their spectral curvature somewhat and only span a limited range in frequency and flux to the left (LBLs) or to the right (HBLs) of the line, with only the IBLs likely to cross it.

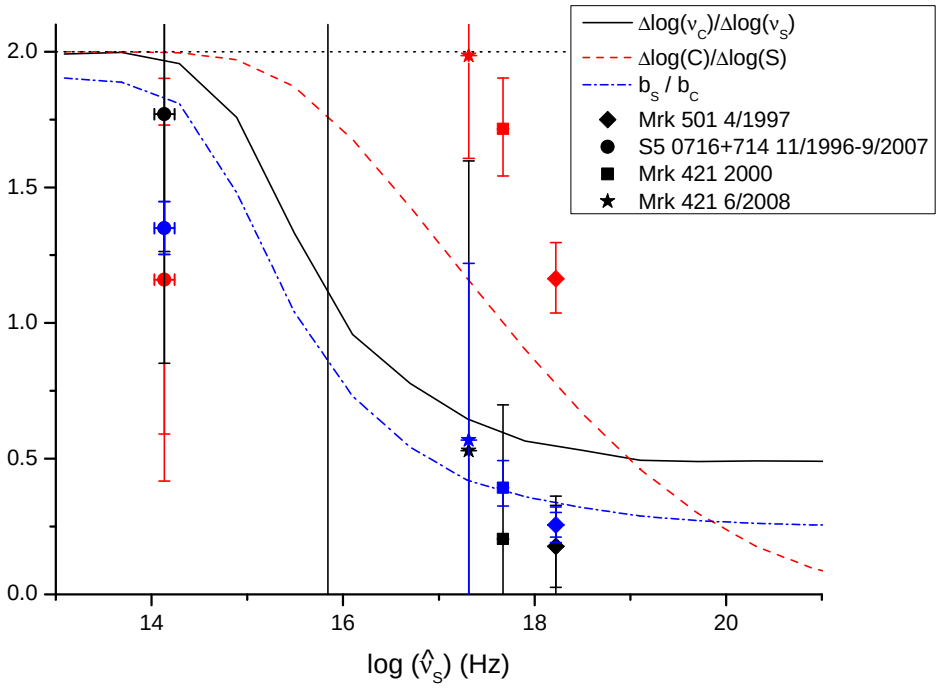

Figure 3.3: Computed changes of spectral parameters corresponding to extended increase of r.m.s. particle energy with the other source parameters kept constant. As functions of $\widehat{\nu_S} = \nu_S\,(B/0.1\text{ G})^{-1/3}(\delta/10)^{-1}(1+z)$ (where ν_S is the synchrotron SED peak frequency, see Eq. 3.16), the full line represents the ratio $\Delta\ln\nu_C/\Delta\ln\nu_S$, the dashed line the ratio $\Delta\ln C/\Delta\ln S$ and the dot-dashed line the curvature ratio b_s/b_c at the peaks. Circles represent the parameters of S5 0716+714 as observed on November 1996 and September 2007 (Tagliaferri et al., 2003; Chen et al., 2008); diamonds represent Mrk501 observations of April 1997 (Djannati-Atai et al., 1999; Massaro et al., 2006); squares represents Mrk 421 observations in 2000 from BeppoSAX and HEGRA (Konopelko et al., 2003); and stars represent Mrk 421 observations performed with GASP-WEBT, *RXTE*/ASM, *Swift*, SuperAGILE, *AGILE*-GRID, ARGO-YBJ, and VERITAS in June 2008 (Donnarumma et al., 2009; Di Sciascio et al., 2010). Each symbol is represented with the same colours as the lines. Changes of n only would yield $\Delta\ln C = 2\,\Delta\ln S$ at all frequencies, represented by the horizontal dotted line; added to a pure r.m.s. energy increase, a moderate increase of n can account for the upward deviations of observed values.

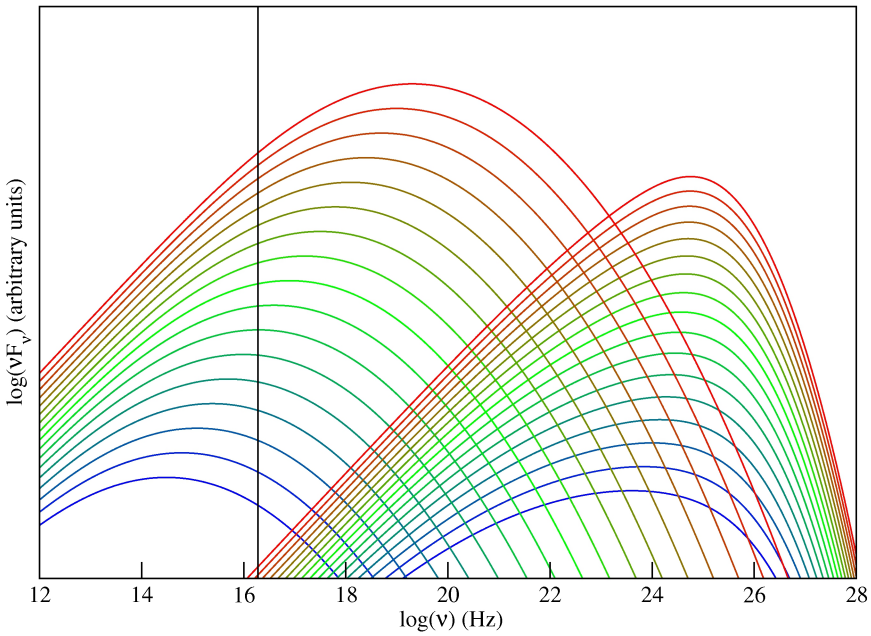

Figure 3.4: As in Fig. 3.2, we show SEDs obtained from numerical simulations (code by Massaro, 2007) of HSZ SSC radiations, for different sources with larger and larger magnetic field B and other parameters kept constant. The vertical line again indicates the transition frequency from the Thomson to the KN regime (see Eq. 3.17); as B increases, the IC scattering changes its regime, and reduced cross section yields similar compression effects as in Fig. 3.2.

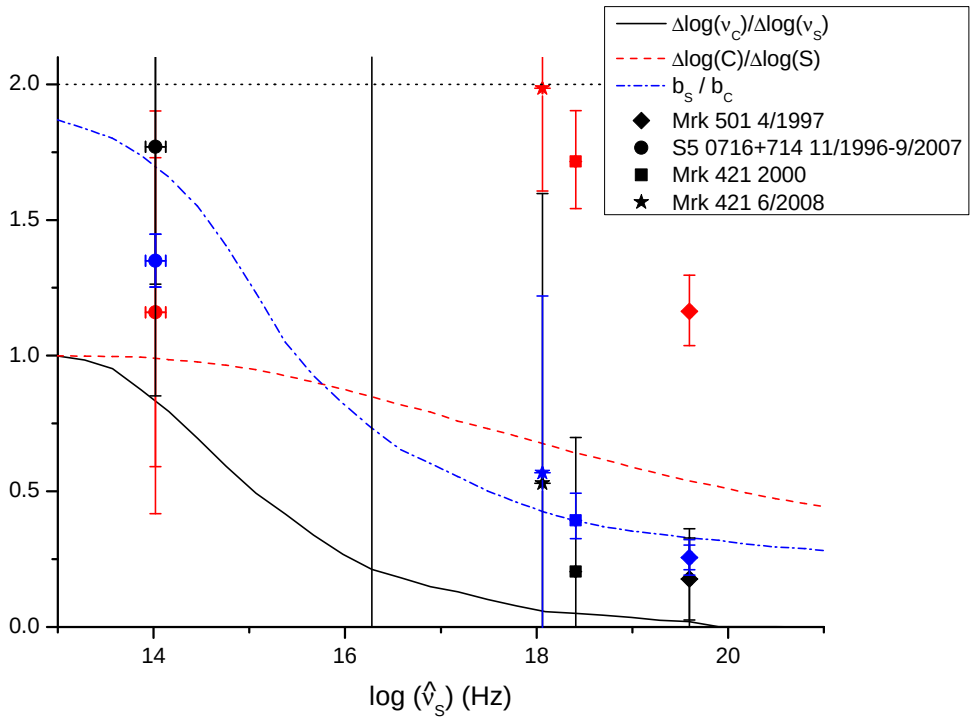

Figure 3.5: Computed changes of spectral parameters as driven by an extended increase of the magnetic field with the other source parameters kept constant. The black full line represents the value of the ratio $\Delta \ln \nu_C / \Delta \ln \nu_S$, the red dashed line represents the value of the ratio $\Delta \ln C / \Delta \ln S$ and the blue dot-dashed line represents the ratio b_s/b_c, for different values of $\widehat{\nu_S} = \nu_S\,(\gamma_p/10^4)10^{(1-1/5b)/2}(\delta/10)^{-1}(1+z)$ (where ν_S is the synchrotron SED peak frequency, see Eq. 3.17), data points are the same as in Fig. 3.3; compared with the latter considerably larger changes of n are needed to recover the observed values.

Imaging Telescope (AIT) in November 14 1996, the synchrotron peak at about at about $10^{14.5}$ Hz falls quite below the threshold frequency expressed by Eqs. 3.16 or 3.17, so we expect for this source the IC scattering to occur mostly in the Thomson regime; simultaneous γ-ray observations were carried out by *EGRET*. The source has shown similarly low flux levels during EGRET observations (Tagliaferri et al., 2003); so for flares with short duty cycle, it is not unreasonable to evaluate variations between the two distant states in the absence of closer observations. The high activity state of the source is described by data relative to GASP project of the WEBT and *AGILE*-GRID observations of 2007 September 7-12, marked by intense flares up to fluxes of 2×10^{-6} photons cm^{-2} s^{-1} in the $0.1 - 10$ GeV energy range. The multi-wavelength variations observed by Giommi et al. (2008) and the increased spectral curvature in 2007 are indicative of the injection of a second component. As shown in Figs. 3.3 and 3.5, peak flux and frequency variations of S5 0716+714 appear to be in between the lines representing increasing r.m.s. particle energy and increasing magnetic field, and so they may be described in terms of HSZ SSC with simultaneous variations of these two parameters.

I stress that in HBL sources even small flux variations in γ rays are expected to have enhanced and observable counterparts in X rays. I suggest that such variations should be checked upon γ-ray "alarms", the inverse triggering relative to usual. The absence of such lower energies counterparts will indicate, for example, a flare driven dominantly by a particle number density increase associated with a magnetic field decrease $n \propto B^{-2}$, causing $S \approx const$ but a decreasing synchrotron peak frequency; such a kind of flare may easily drown into the primary synchrotron component.

3.4 Spectral evolution

We now focus on the time evolution of the electron energy distribution and the related spectral evolution, and in particular on Eqs. 3.24, 3.25 and 3.26 in the simple case of time independent λ_1 and λ_2, when $\int \lambda_{1,2}\, dt \approx \lambda_{1,2}\, t$; then we have

$$s = \frac{1}{2}\left(1 - \frac{\lambda_1}{\lambda_2}\right), \qquad r = \frac{\ln 10}{4\,\lambda_2\, t} \approx \frac{0.58}{\lambda_2\, t}, \tag{3.31}$$

while for the r.m.s. energy we have

$$\gamma_p = \gamma_0\, e^{(\lambda_1 + 3\lambda_2)t}; \tag{3.32}$$

so for the peak frequency and the spectral curvature we have

$$\log\left(\frac{\nu_S}{\nu_{S\,0}}\right) = 2\,(\lambda_1 + 5\lambda_2)\, t, \qquad b_s = \frac{1}{10}\left(5 + \frac{\lambda_1}{\lambda_2}\right)\frac{1}{\log\left(\frac{\nu_S}{\nu_{S\,0}}\right)}, \tag{3.33}$$

where $\nu_{S\,0}$ is a normalization frequency. It is seen that soon after the injection the curvature b_s (proportional to r) *drops* rapidly, then progressively *decreases* more and more gently, while the peak frequency still *increases*.

The value of λ_2 can be evaluated from observing the synchrotron spectral curvatures b_2 and b_1 at two times t_2 and t_1, respectively (recall that $b_s \approx r/5$); denoting with $t_2 - t_1$ this time interval, we have

$$\lambda_2 = \frac{0.58}{t_2 - t_1}\left(\frac{1}{r_2} - \frac{1}{r_1}\right)\frac{1+z}{\delta}; \tag{3.34}$$

on the other hand, form observing the related synchrotron peaks $\nu_{S\,2}$ and $\nu_{S\,1}$, the value of λ_1 can be evaluated as

$$\lambda_1 = \left[\frac{1}{2\,(t_2 - t_1)}\ln\left(\frac{\nu_{S\,2}}{\nu_{S\,1}}\right) - \frac{2.88}{t_2 - t_1}\left(\frac{1}{r_2} - \frac{1}{r_1}\right)\right]\frac{1+z}{\delta}\,. \tag{3.35}$$

For example, in the case of Mrk501 in the states of 7 and 16 April 1997, we obtain (on assuming $B \approx$ const) $\lambda_1 = (2.3 \pm 1.1)$ yr^{-1} and $\lambda_2 = (1.8 \pm 1.7)10^{-1}$ yr^{-1}, corresponding to acceleration times

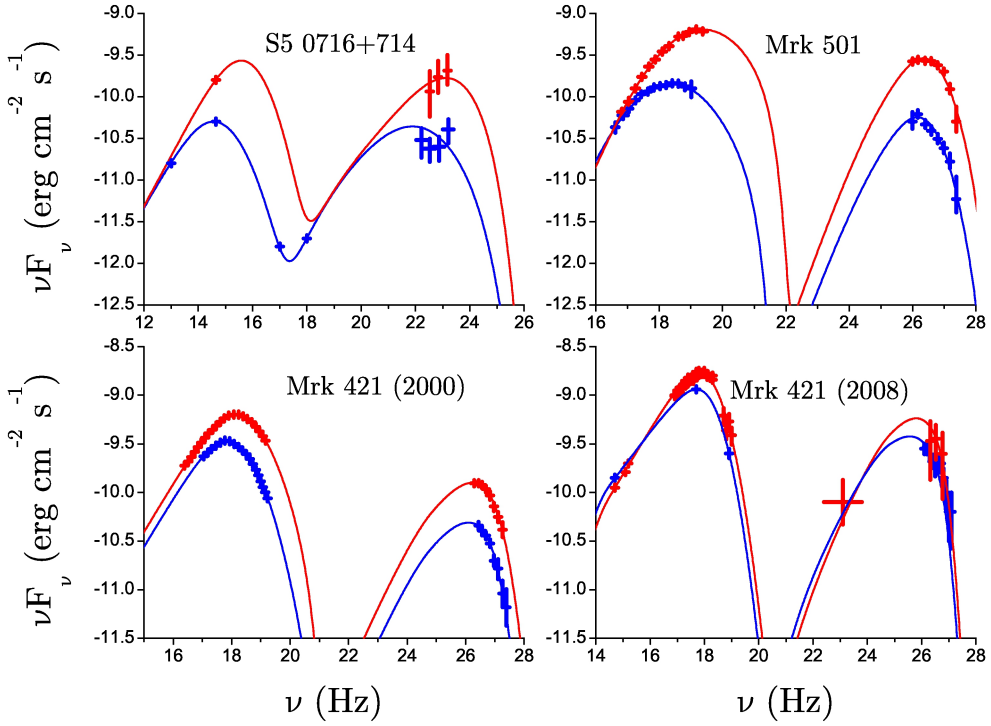

Figure 3.6: SEDs of the BL Lacs considered in the text: S5 0716+174 (upper-left frame), Mrk 501 (upper-right frame) and Mrk 421 (lower-left and lower-right frames), each in a low (blue line) and a high (red line) state. In terms of intrinsic luminosity S5 S5 0716+714 is the strongest source (data referenced in the main text.

$\tau_1 = 1/\lambda_1 = (4.3 \pm 2.0)10^{-1}$ yr and $\tau_2 = 1/\lambda_2 = (5.5 \pm 5.0)$ yr. Note that with the current data the evaluations of λ_1 and λ_2 turn out to be affected by uncertainties considerably larger than the single curvatures $b_1 = 0.161 \pm 0.007$ and $b_2 = 0.148 \pm 0.005$.

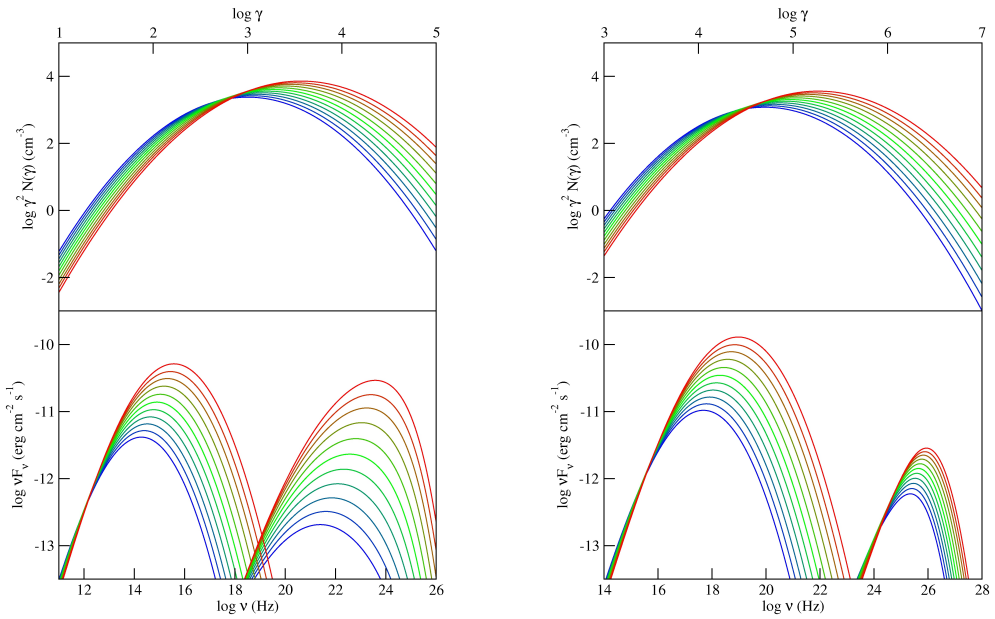

Figure 3.7: Example of time evolution of the $\gamma^2\, N(\gamma)$ distribution (with peak energy γ_p) due to stochastic and systematic accelerations (upper panel) with $\lambda_1 = 5\,10^{-3}$ days^{-1}, $\lambda_2 = 5\,10^{-4}$ days^{-1} from the initial value $\gamma_p = 10^3$ (left panel) and $\gamma_p = 5\,10^4$ (right panel), and of the related evolution for the SSC SEDs (lower panel). In terms of the stochastic acceleration time τ_2, the time interval between each pair of lines is $t_2 - t_1 = 10^{-2}\tau_2$, corresponding to an observed time interval of about two days.

3.4.1 Limiting timescales

Limits to the variability timescales Δt relate to the apparent size of the emission region by $\Delta t \geqslant R\,(1+z)/c\,\delta$ (see §3.2); rapid variations require small emitting sources, but these could be optically thick to the pair production process. In fact, γ-ray photons collide with less energetic ones to produce $e^{\pm}$ pairs, and the cross section of this process tops at a value around $\sigma_T/5$ (where σ_T is the Thomson cross section) when the γ-ray photon frequency ν and the target photons frequency ν_t satisfy the relation $\nu_t \approx m^2\, c^4\, \delta^2 / \left[h^2\,(1+z)^2\,\nu\right]$.

For the γ rays to escape from the emitting region the source "compactness" intervenes and can set lower bounds on the beaming factor (Cavaliere & Morrison, 1980; Massaro, 2007; Begelman et al., 2008). In fact the optical depth for this process is expressed in terms of observational quantities (primed quantities refer to the jet rest frame) as

$$\tau_{\gamma\gamma}\left(\nu'_\gamma\right) = R\,\frac{\sigma_T}{5}\,n'_{ph}\left(\nu'_t\right) \approx \frac{9}{20}\,\frac{\sigma_T\,h}{m^2\,c^6}\,\frac{D^2}{\delta^6}\,(1+z)^4\,\frac{S\,\nu}{\Delta t}\left(\frac{\nu_t}{\nu_S}\right)^{-\beta}, \tag{3.36}$$

where D is the source distance expressed in Gpc, with the shorthand $\beta \equiv b \log\left(\frac{\nu_t}{\nu_S}\right)$. Escaping γ-ray

radiation requires the source to be optically thin, that is, $\tau_{\gamma\gamma}\left(\nu'_\gamma\right) \leq 1$, resulting in

$$\delta \geq \left[\frac{9}{20}\frac{\sigma_T\, h^{1+2\beta}}{m^{2+2\beta}\, c^{6+4\beta}}\, D^2\, (1+z)^{4+2\beta}\, \frac{S\, \nu^{1+\beta}\, {\nu_S}^{\beta}}{\Delta t}\right]^{\frac{1}{6+2\beta}}. \tag{3.37}$$

Thus rapid flux variations set a lower bound on the beaming factor; the highest bound between the previous relation and $\delta \geqslant R\,(1+z)/c\,\Delta t$ is to be relevant.

The exponent β contains a weak logarithmic dependence on δ that may be neglected to a first approximation, and has a magnitude which depends on the source spectral properties; for definiteness, we use for b the typical value 0.2, and for $\nu \approx 10^{27}$ Hz. For a LBL with $\nu_S \sim 10^{14}$ Hz we obtain $\beta \approx 0.4$, while for an extreme HBL with $\nu_S \sim 10^{18}$ Hz, we obtain $\beta \approx -0.5$. A variation timescale $\Delta t \sim 5$ minutes for a LBL with $S \sim 10^{-11}$ erg cm^{-2} s^{-1} implies $\delta \geqslant 30$, while in an extreme HBL with $S \sim 10^{-10}$ erg cm^{-2} s^{-1} we find $\delta \geqslant 15$.

In the specific case of PKS 2155-304 discussed by Begelman et al. (2008), the emitted power $L \approx 10^{46}$ erg s^{-1} corresponds to $S \sim 4\,10^{-11}$ erg cm^{-2} s^{-1}, with $\nu_S \sim 10^{16}$ Hz, to give $\beta \approx 0.1$ and $\delta \geqslant 50$ for $\Delta t \sim 5$ minutes. We note that the source, even if widely considered a HBL, shows peculiar behaviors with respect to other TeV HBLs (see Massaro et al., 2008b); moreover, it does not satisfy the condition $\nu_S \gg \nu_T$ and so it cannot be considered an extreme HBL, as discussed below.

Extreme values of the beaming factor $\delta \sim 50$ have been proposed to account for large peak separations (Konopelko et al., 2003) or to explain very rapid spectral variations (Begelman et al., 2008), formally with $\Delta t \sim 5$ minutes for the γ-ray flares of PKS 2155-304 in 2006 July 28 (Aharonian et al., 2007) and Mrk501 in June 30 and July 9 2007 (Albert et al., 2007a). Note that with BL Lac spectra realistically curved, the observed flux variations may be enhanced due to a slope effect best legible on the differential flux F_ν; that is, when fluxes are measured at frequencies where the spectral slope is steep (as may be the case for PKS 2155-304), a strong observed flux variation implies only a mild variation of the peak flux and requires smaller values of δ. Otherwise, a peak variation on a scale $\Delta t \sim 5$ minutes would require in the SSC model $\delta \sim 100$ for LBLs where $\delta \propto \Delta t^{-\frac{1}{2}}$ (see Eq. 3.7), and $\delta \sim 20$ for an extreme HBL where $\delta \propto \Delta t^{-\frac{2}{5}}$ (see Eq. 3.12).

As stated under §3.3.3, in HBL sources even small flux variations in γ rays should have enhanced counterparts in X rays. These may become hard to observe for example in a flare dominantly driven by particle number density increase associated with a magnetic field decrease (i.e., with $n \propto B^{-2}$), leading to a synchrotron emission easily drowned into other components. On the other hand, components with $\delta > 20$ appearing in an HBL spectrum go beyond the HSZ SSC model with variations of one dominant parameter, and therefore require a more elaborate source structure.

In such cases the next natural scenarios are provided by decelerated relativistic outflows (Georganopoulos & Kazanas, 2003), or by nested spine-layer jets (Tavecchio & Ghisellini, 2008a) and jets in a jet (Giannios et al., 2009).

3.5 KN correlations in the decay stage

Here I briefly comment on the decay phase of a flare, when fluxes and frequencies decrease; the aim is at understanding the quadratic correlations between the γ-ray and the X-ray fluxes observed in HBL objects like Mrk421 and Mrk501 (see Katarzyński et al., 2005; Fossati et al., 2008). As anticipated in Sect. 2.1.1, electron energy losses by adiabatic expansion (at a constant rate) can be accounted for by adding to the Fokker-Planck equation a negative term that combines with the systematic acceleration rate into an overall coefficient $\lambda_1 \to \lambda_1 - \frac{1}{t}$.

Correspondingly, the size of the source grows as $R \propto t$; with the total particle number remaining constant, in the extreme Klein-Nishina regime Eqs. 3.24 and 3.26 may be rewritten as

$$S \propto \exp\left[2\int\left(\lambda_1 - \frac{1}{t}\right)dt\right],$$

$$C \propto \exp\left[-2\int \frac{1}{t}\,dt\right],$$

on neglecting the stochastic acceleration contribution.

If both front shock thickness and gas clouds size scale as $R(t)$ then $\lambda_1 = 1/(A\,t)$ holds. With $A \geq 1$ both the synchrotron and the IC flux will decrease. The particular choice $A = 2$ yields a quadratic correlation between the IC and the synchrotron peaks, that is, $\Delta \log C = 2\,\Delta \log S$. One should not quail at the fine tuning corresponding to $A = 2$ literally, because lower values of $1 < A < 2$ are more effective in a mild KN regime. On the other hand, A cannot be large lest the shock is stalled.

3.6 Beyond the SSC

In Table 3.2 I have provided a comprehensive *benchmark* to gauge the performance of the HSZ SSC model for flaring BL Lac objects. This allows us to easily recognize events that may be accounted for within the model with physical variations of key source parameters, or that instead require more complex source structures.

Toward that purpose, I have used realistic log-parabolic spectral shapes produced by log-parabolic energy distributions of the emitting electrons, and studied IC radiation both in the Thomson and the Klein-Nishina regimes.

In the model we expect S to dominate C fluxes; in fact, moving to higher energies in a collection of different sources or in a prolonged evolution of a given source, we expect the emission to drift out of the pure Thomson and approach the KN regime, where the cross section decreases and limits the IC fluxes enforcing $C \lesssim S$. Such a relation is found to hold in a number of sources, and in particular in HBLs (see for example Tagliaferri et al., 2008).

From Table 3.2 I stress here the source spectral *variations* predicted in γ rays. For LBLs, where the IC scattering mostly occurs in the Thomson regime, we recover the standard quadratic increase in γ-ray fluxes with respect to IR-optical ones, expressed by $\Delta \ln C \approx 2\,\Delta \ln S$ for dominant particle r.m.s. energy variations (see Eq. 3.27). Instead for HBLs, in which the IC scattering approaches the Klein-Nishina regime, we expect *smaller* or even vanishing increases of the γ-ray flux relative to X rays, that is, $\Delta \ln C \backsimeq 0$ for dominant particle r.m.s. energy variations (see Eq. 3.29).

Comparing with specific sources, we find the HSZ SSC model to be adequate for most LBLs at the present observational levels; whilst for example the HBL source Mrk501 in April 1997 showed a γ-ray flux increase appreciably stronger than expected if it were dominated by just one driving parameter. We explain this behavior within the model in terms of an additional, *smooth* and moderate increase (by a factor around 2) in number density of the electrons responsible for the emission (see §3.3.3). Such conditions can still be provided by a *single* electron population; this should be marked by a continuously *decreasing* spectral curvature b, as indicated by current data (Massaro et al., 2006), a feature providing a potentially powerful signature to closely check on further data. Instead, for dominant magnetic field variations we would expect $\Delta \ln C \approx \Delta \ln S$ for LBL sources (see Eq. 3.28), and $\Delta \ln C \approx \frac{1}{2}\Delta \ln S$ for HBL sources (see Eq. 3.30); but in that case the required increase in particle number density should be much *higher* by a factor of about 30, hard to interpret in terms of a single electron population.

On the other hand, on using the previous relations inversely, we see that even small γ-ray variations in HBL sources ought to have *enhanced* counterparts in the X rays, unless flare activity were driven by an additional jet component, for example one with higher magnetic field but lower particle density; thus the corresponding emission is easily overwhelmed by, or drowned into the main synchrotron, but then the rest frame acceleration times must be short enough to involve a significant fraction of the emitting region. I suggest this is as a critical test for the simple model.

Another limitation arises from *rapid* peak flux variations requiring large values of δ as shown in §3.4.1. In the extreme, the few sources with particularly fast γ-ray increases observed so far, like PKS 2155-304 in 2006 July 28 and Mrk501 in June 30 and July 9 2007 (see §3.4.1), require *additional* components with very high beaming factors that go definitely beyond the simple SSC model.

Finally, another problem for the model arises from LBL objects showing substantial emissions in the GeV-TeV range that cannot be explained it terms of the simple HSZ SSC model (considering that second order IC scattering is negligible, see Massaro 2007) because the IC peak falls for these sources around 0.1 GeV; this may be the case for BL Lacertae itself (Albert et al., 2007b) and possibly similar sources like M87 (Georganopoulos et al., 2005) and Cen A (Lenain et al., 2008; Aharonian et al., 2009a).

In all these cases the source may require more *elaborate* structure, like decelerated relativistic outflows or sub-jet scenarios (see Georganopoulos & Kazanas, 2003; Tavecchio & Ghisellini, 2008a; Giannios et al., 2009). I stress that the injection of a *second*, nearly monoenergetic electron population is expected to be marked by a sudden *increase* of the spectral curvature.

3.7 Discussion

I proposed in this Chapter that the sources of BL Lac type may be conveniently ordered in a *succession* spanning from smooth variations of one or a few dominant SSC parameter, up to the appearance of truly different components that ultimately break through the limits of the simple HSZ SSC model. Even more so at increasing energies and frequencies, that would imply weaker and weaker γ-ray fluxes relative to X-ray, owing to KN cross section effects. This picture is supported by the following two lines of evidence.

First, a recent statistical study of Third EGRET Catalogue data (Mukherjee , 2001; Casula, 2008) shows for BL Lac objects observed at 30 MeV $\div$ 30 GeV a weak γ-ray variability on average, compared to the FSRQ Blazars. Also the time-structure functions for these two classes of objects indicate a similar trend, within the limitations of the sample.

Second, the first *AGILE*-GRID Catalogue of high confidence gamma-ray sources (Pittori et al., 2009) apparently shows few if any new BL Lac sources other than those already detected by EGRET. This circumstance suggests the sources observed by *AGILE* to be more powerful than the average; it leads to expect for the majority of the sources either reduced flare activity in this band, or weak average fluxes. I relate these features to reduced Klein-Nishina cross section that tends to limit both the average fluxes and the flares.

4

Flares

4.1 Introduction

As mentioned above, Blazars comprise two major subclasses: the gas-rich Flat Spectrum Radio Quasars with high accretion rates, and the gas-poor BL Lac objects with low current accretions. In this Chapter I will show that this dichotomy in physical properties of Blazars is yet enhanced in their strong flaring activity.

In particular, it is interesting to note that the intrinsic outputs of several BL Lacs are observed to level off at values of about 10^{46} erg s^{-1}; to investigate this evidence I studied observations of the BL Lac presented in the previous Chapter, namely S5 0716+714, Mrk 421 and Mrk 501. These are "dry" BL Lacs, that is, sources that show no evidence of surrounding gas like just weak (if any) and intermittent emission lines, or direct emission from an accretion disk like a big blue bump (see Peterson, 1997; Kembhavi & Narlikar, 1999); these facts points to low current accretion rates in Eddington units ($\dot{m} \sim 10^{-2}$, see e. g. Ghisellini et al. 2009a). So, the spectral distributions of their pure non-thermal radiations are effectively represented by the synchrotron self-Compton process. They provide an appropriate testing ground for comparing their intrinsic outputs with maximal powers extractable from rotating supermassive black holes and from the dragged accretion disks by means of large-scale electromagnetic fields, via the intriguing, variously debated Blandford-Znajek electrodynamics (BZ, Blandford & Znajek 1977; see also Ghosh & Abramowicz 1997; Krolik 1999; Livio et al. 1999; Cavaliere & D'Elia 2002; McKinney 2005; Nemmen et al. 2007; Tchekhovskoy et al. 2009). The bare hole contribution can yield up to $L_K \sim 2 \times 10^{45} \left(M_\bullet/10^9\, M_\odot\right)$ erg s^{-1}, given the hole mass $M_\bullet$ in units of $10^9 M_\odot$ and a magnetic field $B \sim 10^4$ G threading its horizon. With the source parameters derived in the previous Chapter, I find for S5 0716+714 a total jet power of about 3×10^{45} erg s^{-1}, which makes it one of the brightest dry BL Lacs so far detected in γ rays. The associated Kerr hole is found to be around $5 \times 10^8 M_\odot$, implying that the source is close to the BZ limit; the other dry BL Lacs remain well below that threshold.

On the other hand, FSRQ broad emission lines and strong Big Blue Bump yield evidence of plenty surrounding gas, associated to high current accretion at $\dot{m} \sim 1$. Such accretion provides seed photons from outside the jets, that drive an additional contribution to the non-thermal radiations by the external Compton scattering (EC; see Dermer & Schlickeiser, 1993; Sikora et al., 1994). Such EC contributions often dominate the γ-ray outputs of FSRQs (Maraschi & Tavecchio, 2001).

While the BL Lac flares yield spectral evidence of being driven by ongoing acceleration of highly relativistic electrons in the jet (as shown in the previous Chapter), in FSRQs we observe external Compton radiation enhanced by increased production of thermal seed photons, mainly driven by increasing accretion; so these sources are not expected to be limited in their flares by limits on maximal available power in the Blandford-Znajek scenario. To test this framework I compare the BL Lac flaring activity with strong flares of two Flat Spectrum Radio Quasars 3C 454.3 and 3C 279, recently detected in γ rays with the *AGILE* and *Fermi* satellites; in particular, on the luminosity - electron energy plane these flares trace patterns that diverge from those followed by luminous, flaring BL Lacs.

Source name	γ_p	L_r	L_T
S5 0716+714 (low)	9.1×10^2	4.2×10^{44}	1.3×10^{45}
S5 0716+714 (high)	2.8×10^3	1.5×10^{45}	3.1×10^{45}
Mrk 501 (low)	1.4×10^5	4.9×10^{42}	1.2×10^{43}
Mrk 501 (high)	1.9×10^5	2.3×10^{43}	3.1×10^{43}
Mrk 421 (2000, low)	5.2×10^4	4.0×10^{42}	1.9×10^{43}
Mrk 421 (2000, high)	6.1×10^4	8.1×10^{42}	3.1×10^{43}
Mrk 421 (2008, low)	2.5×10^4	1.6×10^{43}	4.1×10^{43}
Mrk 421 (2008, high)	3.4×10^4	2.1×10^{43}	4.6×10^{43}

Table 4.1: Parameters for the BL Lac sources discussed in the text. Powers L_r and L_T are given in erg s^{-1}.

4.2 The source power

To estimate the power content of Blazar jets we are interested in the *intrinsic* outputs referred to the jet frame, rather than in the luminosities $L_{iso} = 4\pi D_L^2 F$ inferred from insisting on an isotropic distribution of the observed flux F, at the luminosity distance[1] D_L. We assume one "cold" proton per electron satisfying $\langle\gamma\rangle \lambda m_p/m_e$ (with the average $\langle\gamma\rangle = \gamma_p \times 10^{-1/4r}$ bounded in terms of the electron m_e and the proton m_p masses), and follow Celotti & Ghisellini (2008) in writing for the intrinsic radiative luminosity L_r contributed by both the synchrotron and IC radiations and for the related powers carried by the jet, the expressions

$$L_r = L_{iso}\,\Gamma^2/\delta^4 \approx L_{iso}/16\,\Gamma^2\,, \tag{4.1}$$

$$L_e = \frac{4}{3}\pi R^2\, c\, n\, m_e\, c^2\, \langle\gamma\rangle\, \Gamma^2\,, \tag{4.2}$$

$$L_p = \frac{4}{3}\pi R^2\, c\, n\, m_p\, c^2\, \Gamma^2 = L_e\, \frac{m_p}{m_e\,\langle\gamma\rangle}\,, \tag{4.3}$$

$$L_B = \frac{1}{6}\, R^2\, c\, B^2\, \Gamma^2\,. \tag{4.4}$$

The total jet power is therefore given by $L_T = L_r + L_e + L_p + L_B$.

The five source parameters n, R, B, γ, and δ (or Γ) entering Eqs. 4.1 - 4.4 are obtained in the previous Chapter (see Table 3.1), and yield the luminosities collected in Table 4.1. Note that for the FSRQs with average electron energies $\langle\gamma\rangle < 10^3$ the proton component to the energetics is considerable and hardly variable; this steadily feeds the energetics of the radio lobes (Celotti et al., 2001).

4.3 The BZ benchmark

As anticipated in Sect. 4.1, a natural benchmark for these powers is provided by the BZ mechanism for electrodynamical energy extraction from a Kerr hole spun up to maximal rotation by past accretion episodes. A minimal, vestigial disk is required to hold the poloidal magnetic field threading the horizon; the disk is kept active by low accretion rates $\dot{m} \lesssim 10^{-2}$ in Eddington units, loses angular momentum mainly via the large-scale field, and contributes some $3\,L_K$ to the total power (Blandford & Znajek, 1977; Livio et al., 1999). The two contributions add to yield

$$L_{BZ} \approx 8 \times 10^{45} \left(\frac{M_\bullet}{10^9\, M_\odot}\right) \text{ erg s}^{-1}\,. \tag{4.5}$$

[1] In the following, we adopt the standard, flat cosmology with $H_0 = 72$ km s^{-1} Mpc^{-1} and $\Omega_\Lambda = 0.74$ (Dunkley et al., 2009).

Note that the balance $B^2/4\pi \sim p$ between the magnetic stress and the kinetic or radiation pressure p in the disk yields $B \sim 10^4$ G; for a radiation-pressure dominated disk, one has at the inner rim $B^2 \propto 1/M_\bullet$, so B has dropped out of Eq. 4.5.

The hole mass is then the key parameter, that can be evaluated from its correlation with the absolute red magnitude M_R of the host galactic bulge (Ferrarese & Merritt, 2000; Gebhardt et al., 2000; Falomo et al., 2003); for our cosmology this reads

$$\log\left(\frac{M_\bullet}{M_\odot}\right) = -0.50\, M_R - 2.61\,, \tag{4.6}$$

with scatter ±0.4 dex (Bettoni et al., 2003). For the host galaxy of S5 0716+714, observations of the magnitude $R = 18.3 \pm 0.5$ reported by Nilsson et al. (2008), besides indicating the redshift $z = 0.31 \pm 0.08$, yield a mass $M_\bullet \simeq 5.5^{+8.0}_{-3.3}\, 10^8\, M_\odot$; the central value is consistent with estimates from microvariability of the optical flux (Sasada et al., 2008), which yield $M_\bullet \sim 10^8 M_\odot$. For Mrk 501 and Mrk 421, one obtains $M_\bullet \simeq 1.0^{+2.4}_{-0.7}\, 10^9\, M_\odot$ and $M_\bullet \simeq 4.1^{+7.8}_{-2.7}\, 10^8\, M_\odot$, respectively.

Results normalized to the respective L_{BZ} from Eq. 4.5 are represented in Fig. 4.1. During flares, the electron rms energies (and the peak frequencies) are boosted in all sources, and so are the luminosities; this indicates that rising flares are directly related to increased *acceleration* of the emitting electrons.

I emphasize that the powerful source S5 0716+714 is apparently constrained to move *sideways*, as if to skirt the BZ limit; Mrk 421 in the 2008 states exhibits a similar behaviour, although with lower significance. On the other hand, the weaker source Mrk 421 in 2000 and the yet weaker Mrk 501 remain considerably below the BZ limit and so are expected to be free to move more vertically, as they do.

4.4 BL Lac flaring patterns

For dry BL Lacs with accretion rates $\dot{m} < 10^{-2}$, the SSC radiation process provides a robust evaluation of the jet luminosities. Whence L_{BZ} provides a significant *benchmark* for the output of the BL Lacs discussed here, and indeed an upper limit to both their quiescent states and flares. In fact, during its recent flare S5 0716+714 was observed to be constrained by $L_{BZ} \lesssim 10^{46}$ erg s^{-1}, and a similar behavior was observed in 2008 for Mrk 421. Non-thermal, beamed powers in the range $L_K - L_{BZ}$ also provide evidence of an accretion disk that is active mainly in launching and channeling the jets by means of large-scale fields.

Referring to Fig. 4.2 and its caption, note that during flares the sources move in the L_T - γ_{peak} plane away from the envelope that is outlined by bright BL Lacs with increasing rates $\dot{m}$; the envelope ends up in the locus of the yet brighter FSRQs with $\dot{m} \sim 1$. The flares then move into a region of faster radiative cooling (Celotti & Ghisellini, 2008, and references therein). This implies short-lived flares on timescales $\lambda 1$ day, or requires shorter acceleration times $t_a \sim \gamma/E$ with higher E, as an alternative to structured sources such as decelerating (Georganopoulos & Kazanas, 2003) or spine-sheath jets with inner scale $R_1 < R$ (Tavecchio & Ghisellini, 2008b). Faster acceleration and deviations from the envelope are consistent with flares caused by electron *boost* rather than episodes of increased accretion onto the disk.

In this context, note that sources lying along the envelope in Fig. 4.2 at higher L and lower γ_{peak} often exhibit stronger evidence of current accretion up to $\dot{m} \sim 1$, such as thermal emissions and surrounding gas (big blue bump and broad emission lines), with a larger contribution from EC (see Blandford 1990; Padovani et al. 2007b). In fact, the progression from dry BL Lacs to FSRQs is likely to involve an enhanced and extended disk contribution as described by Blandford & Payne (1982), starting with "wet" BL Lacs with $\dot{m} \sim 10^{-1}$; these feature larger EC contributions (Dermer, 2008) and looming evidence of gas, including some thermal disk emission and weak or intermittent lines (Celotti et al., 2007). The last step in this progression is constituted by the powerful FSRQs with extant broad lines, a big blue bump from disks accreting at full rates $\dot{m} \sim 1$, and a dominant or towering EC (Maraschi & Tavecchio, 2001).

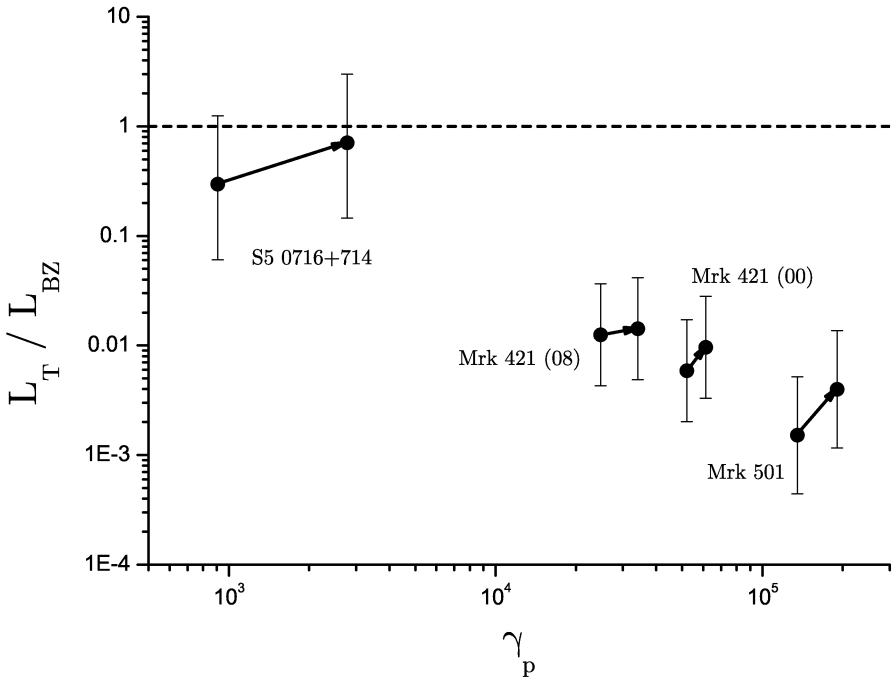

Figure 4.1: For the named sources the total jet luminosities normalized to their BZ power are plotted against the electron rms energy. Bars represent the hole mass uncertainties reflecting those (at the $1-\sigma$ level) in host bulge luminosities, and including the scatter in Eq. 4.6.

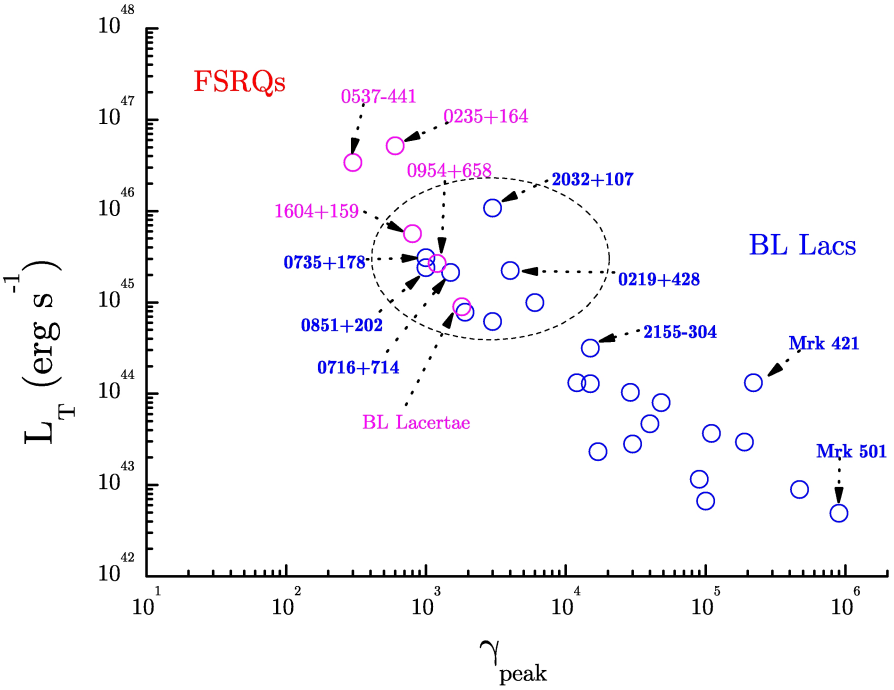

Figure 4.2: Bright BL Lacs in their context, adapted from Celotti & Ghisellini (2008) with historical data in terms of L_T and the energy γ_{peak} related to the synchrotron peak ($\gamma_{peak} = \gamma_p \times 10^{1/2r}$). Blue circles indicate dry, while violet circles indicate wet BL Lacs. The lower-left region of the diagram corresponds to the source condition $t_c > R/c$, and the upper-right to $t_c \gtrsim t_a$. Bright FSRQs lie at lower γ_{peak} and higher powers, with increasing signs of current $\dot{m} \to 1$; selection effects depopulate weaker sources in the lower region (see Padovani, 2007a). The dashed oval highlights sources in the transition region from dry to wet BL Lacs, interesting to compare with L_{BZ} from Eq. 4.5 particularly when at $z \gtrsim 0.3$.

In addition, the outputs of even misaligned BL Lacs may be *calorimetrically* gauged from their feedback actions on the intra-cluster plasma surrounding their host galaxy when located in a cluster or a group of galaxies, as discussed by McNamara et al. (2007). These authors evaluate average powers around 10^{46} erg s^{-1} injected into the cluster MS0735.6+7421, and possibly also in the cluster A2029 and the group AWM 4.

The whole of the above evidence provides observational support to the *relevance* of the electrodynamical BZ mechanism, and invites extended sampling of other interesting sources (see Fig. 4.2).

If in dry BL Lacs with $M_\bullet < 10^9 M_\odot$ the L_{BZ} limit were found to be substantially exceeded by outputs $L_T > 10^{46}$ erg s^{-1}, this would require $B > 10^4$ G at the Kerr horizon. These fields imply large dynamical stresses bounded only by $B^2/4\pi \leq \rho c^2$, associated with particle orbits plunging from the disk toward the hole horizon (Meier, 2002) into a region fully controlled by strong gravity effects.

Thus, all such sources will provide powerful tests for the coupling of electrodynamics with General Relativity in full swing, and constitute an exciting arena for *AGILE* and *Fermi*-LAT data.

4.5 External Compton

As to the FSRQs, we have the additional and often dominant EC component originated from seed photons emitted outside the jet, specifically by the broad line region (BLR) or by the inner accretion disk. The latter's emission is often modeled as a sum of annular concentric surfaces radiating locally as a black body; their temperatures follow along the radius $\mathcal{R}$ the profile (see Shapiro & Teukolsky, 1983)

$$T(r) = T_* \left[\frac{R_i^3}{\mathcal{R}^3} \left(1 - \sqrt{\frac{R_i}{\mathcal{R}}} \right) \right]^{1/4} , \tag{4.7}$$

where $T_* \equiv \left(3GM_\bullet \dot{M} / 8\pi {R_i}^3 \sigma \right)^{1/4}$, $\dot{M}$ is the accretion rate, and$R_i \approx GM_\bullet/c^2$ is the last sable orbit radius. The integrated emission has a peak flux $S_d \propto \dot{M} \propto {T_i}^4$ at a peak frequency $\nu_d \propto \dot{M}^{1/4} \propto T_i$. The BLR instead comprises a number of "clouds" at distances $\sim 10^{17-18}$ cm intercepting some 10% of the radiation coming from the disk at ionization parameter values $\sim 10^{-1}$ (Padovani, 1988).

These external photons scatter off the electrons in the jet to yield EC radiation, with a SED again following log-parabolic shapes. For the photons coming from the disk at a height scale D_d from the emitting region, the EC radiation has a peak flux $S_D \propto \dot{M} \gamma_p^2 R^3 n D_d^{-2} \Gamma^{-1}$, a peak frequency $\nu_D \propto \dot{M}^{\frac{1}{4}} \gamma_p^2 \Gamma^{-1}$, and a spectral curvature $b_D \approx r$ close to the electron distribution's. For photons coming from the BLR we have a peak flux $S_{\mathcal{B}} \propto \dot{M} \gamma_p^2 R^3 n \Gamma$, a peak frequency $\nu_D \propto \dot{M}^{\frac{1}{4}} \gamma_p^2 \Gamma^{-1}$, and the spectral curvature is again $b_{\mathcal{B}} \approx r$.

We recall that the observed frequencies are enhanced by the beaming factor δ, while the fluxes are boosted by δ^4, with $\delta \approx 2\Gamma$ for small viewing angles $\sim 1/\Gamma$ (Begelman et al., 1984). The EC flux is further enhanced by factors $\Gamma - \Gamma^2$ depending on the scattering geometry for the BLR photons (Dermer & Schlickeiser, 2002; Ghisellini & Tavecchio, 2009b). Examples of these emissions and contributions to the SEDs are computed and illustrated in Fig. 4.3, for both the low and high states of a typical FSRQ with $M_\bullet \approx 10^8 M_\odot$, $\dot{m} \approx 1$, $\Gamma \approx 10$, $R \approx 10^{17}$ cm, $B \approx 1$ G and $n \approx 10^2$ cm^{-3}, and $\gamma_p \approx 10^2$. These will be used in Sect. 4.6 as templates to focus the main flare drivers, preliminary to our detailed fits in Fig. 4.4.

Note that radiative cooling (particularly effective with bright EC radiation) will erode at high γ the electron distribution from the basic log-parabolic shape, but numerical simulations including synchrotron cooling show that the distributions retain an approximately log-parabolic shape around their peak, though with sharpened curvature (Massaro et al., 2006, in particular their Fig. 4). Meanwhile, analytical solutions of the Fokker-Planck equation including systematic and stochastic accelerations along with cooling are obtained in the form of a power series in terms of $q = t_2/2\,t_c$, the ratio of the stochastic acceleration time t_2 into the cooling time t_c, resulting in $q \approx 10^{-1}$ for $\gamma_0 \simeq 10^3$ and $B \simeq 0.1$ G

(Paggi et al., 2009a,b). While the zeroth order solution is the log-parabola, the first order correction steepens the energy distribution at the high end $\gamma \gtrsim 1.5 \times 10^3$, mimicking a somewhat sharpened curvature, and correspondingly affects the SEDs at frequencies beyond their peaks; systematic acceleration moves the deviations upwards yet (as shown in Fig. 2.2). On the other hand, broken power laws for the energy distribution and the resulting SED (as used, e.g., Donnarumma et al. 2009, Vittorini et al. 2009) provide closely similar shapes of the SED around, and well beyond their peaks.

4.6 Flares of 3C 454.3 and 3C 279

The dominant process driving the blazar flares can be tested from the observed spectral changes compared with the templates provided by Fig. 4.3.

In several flaring BL Lacs the SEDs have been observed to increase both their peak heights and positions (see Paggi et al., 2009a); in particular, the synchrotron peak considerably shifting up in frequency constitutes clear evidence of electron *acceleration*.

On the other hand, in several FSRQs the dominant and growing second spectral peak along with the nearly stable synchrotron frequency *favors* the EC process driven by increasing external seed photon flux as shown in Fig. 4.3-d, over the alternatives presented in Fig. 4.3-a, b, c. Correspondingly, our fits to the specific SEDs of 3C 454.3 and 3C 279 are presented in Fig. 4.4, with model parameters given in Table 4.2[2]. I stress that both sources the fits require considerably larger values of $\dot{m}$ in the flares, with limited variations of the other parameters; for 3C 279, however, the low X rays in the high state indicate a larger height scale D_d of the emitting region.

So the large flares of the FSRQs 3C 454.3 and 3C 279 appear to be dominated by thermal seed photons increasing their energy somewhat, and much more their *flux*, as expected from the increasing *accretion* rates discussed in Sect. 4.5. To wit, the EC flux grows strongly in γ rays while in the IR-optical bands little or no increase occurs for the synchrotron peak frequency (see Fig 4.4).

4.6.1 Historical states and flaring patterns

Our main concern here is constituted by bright blazars; their historical conditions are effectively represented in the L_T - γ_p plane (see Fig.4.5), where they appear to be strung along a "bright blazar strip" with some scatter. The BL Lac sources reside in the center/right region, on the branch where the crossing time $t_{cr} = R/c$ matches the cooling time $t_c \propto 1/\gamma w$ related to the energy density w in the magnetic or radiation field, to yield $L_T \propto \gamma^{-1}$. On the other hand, the FSRQs lie in the upper left region, on the branch where the cooling time is matched by the acceleration time $t_a \propto \gamma/E$ related to the effective electric field E (see Cavaliere & D'Elia 2002, Ghisellini et al. 2009a), to yield $L_T \propto \gamma^{-2}$. The lower/left corner of the plane is populated by weaker sources out of our present scope (see Padovani et al., 2003).

We see from Fig. 4.5 that on this plane the major flares move *out* considerably of the bright blazar strip into regions where the sources have higher luminosities and total powers, and faster radiative cooling. In particular, the FSRQs move *vertically*, whereas luminous BL Lacs (e.g., 0716+714 and Mrk421) move in a substantially *slanted* direction (Paggi et al., 2009b). I interpret these patterns in terms of source structure changing as follows.

The flares of "dry" BL Lacs are mainly driven by increasing γ causing larger synchrotron radiation; the cooling is faster but still can be balanced by shorter crossing times through a smaller source size (like is the case for jets with inner structure, see Tavecchio & Ghisellini 2008b, Giannios et al. 2009), to yield $\gamma \sim 1/R$ and $L_r \propto N/R^2$ in terms of the electron number $N \propto nR^3$. Eventually, the source power may exceed the yield from current accretion; so it has to live on the alternative reservoir constituted by the rotational energy of the SMBH, accumulated during previous massive accretion episodes, and tapped via the General Relativistic mechanism proposed by Blanford & Znajek in 1977. This implies

[2]Notice that larger particle densities found in FSRQs than in BL Lacs are consistent with different matter contents in the surroundings of the two source kinds.

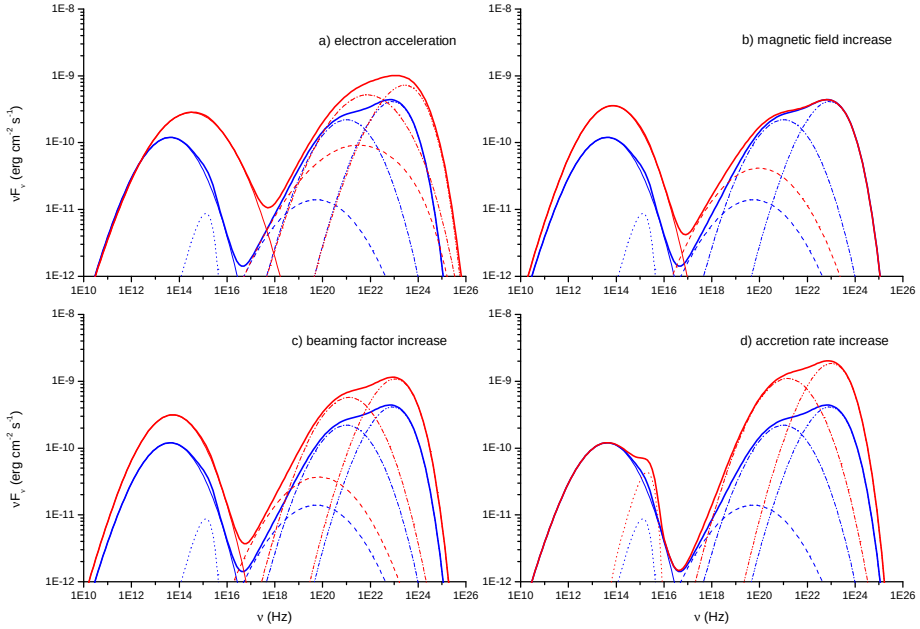

Figure 4.3: Templates of the SEDs of a typical FSRQ. The pre-flare condition (blue lines) comprises the five spectral components with their parameters discussed in Sect. 4.5: synchrotron emission (full lines), SSC radiation (dashed lines), accretion disk emission (dotted lines), disk EC radiation (dot-dashed lines), and BLR EC radiation (double-dot-dashed lines). We also represent flares (red lines) driven by different processes corresponding to an increase by a factor 1.5 in the key parameter: electron energy γ_p (panel a), magnetic field B (panel b), Lorentz factor Γ (panel c), and accretion rate $\dot{m}$ (panel d). In Table 4.2 we give the detailed parameter values for the case (d), that is shown to be most relevant in Fig. 4.4.

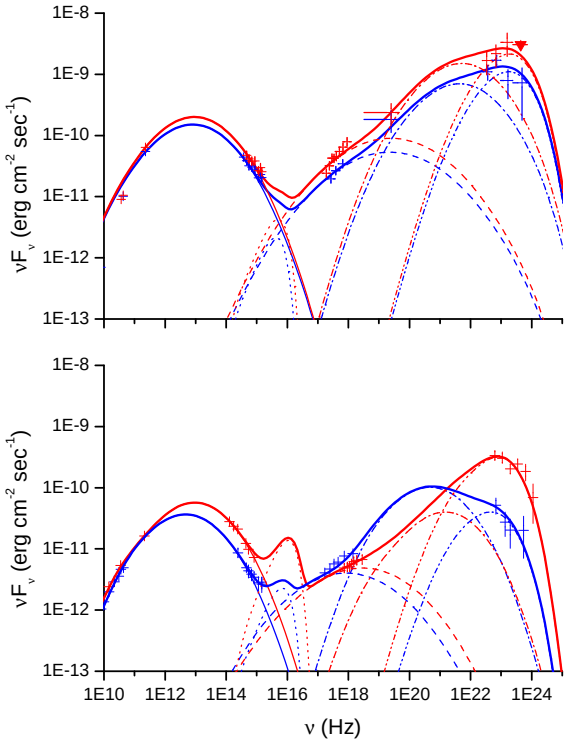

Figure 4.4: Our fits to the SEDs of two specific FSRQs: (top panel) low (blue lines) and high (red lines) state of the FSRQ 3C 454.3, as recently reported by Pacciani et al. (2010); (low panel) low and high states of the FSRQ 3C 279 (Abdo et al., 2010c). Model parameters are given in Table 4.2.

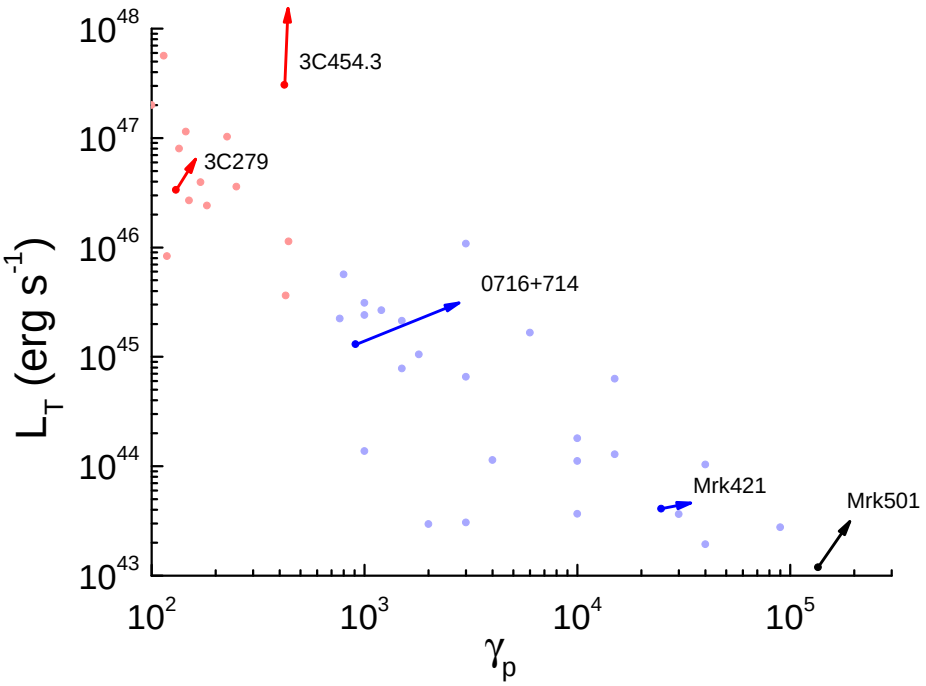

Figure 4.5: Flaring patterns on the L - γ_p plane of blazars superimposed to the BBS, the strip covered by bright historical blazar states (data adapted from Ghisellini & Celotti 2008). Light blue dots represent BL Lacs and light red dots represent FSRQs. The arrows shows enhance the variations to appear more prominent on double-log scale; for FSRQs (red arrows) the directions are almost vertical, due to electron energies being limited by strong radiative cooling (see Sect. 4.2); for gas-poor but luminous BL Lacs (blue arrows) the flare directions show patterns slanted to the right because of limited power available, e. g., from the BZ process. The actual high states are reported in Tables 4.1 and 4.2.

$L \lesssim 8\times10^{45}\, M_\bullet/10^9\, M_\odot$ erg/s; weaker and more massive sources like Mrk501 are not affected by such a constraint (see also discussion by Paggi et al., 2009b).

On the other hand, the flares of the luminous FSRQs are not so constrained in view of their high current accretion; the sources increase their luminosity $L_r \propto \gamma^2 N S_D$, and in entering the fast cooling region are assisted by acceleration from E increasing with luminosity to yield $\gamma \propto R\sqrt{E/L_r} \sim const$ (see Cavaliere & Morrison, 1980). Note that $L_T > L_r$ holds after the discussion in Sect. 4.2, implying on the L_T - γ_p plane relatively short excursions for substantial radiative flares; i have extended the relative arrows in Fig. 4.5 to highlight their directions, the relevant information in the present context.

4.7 Discussion

The different spectra observed in the two blazar subclasses, BL Lacs and FSRQs, during pre-flare conditions clearly relate to their *different* physical properties, i.e., the dearth or plenty of gas surrounding the central SMBH.

Here I have studied how this physical dichotomy is reflected in the flaring activity. I find that during the flares the BL Lac and the FSRQ follow different patterns, in fact, *diverging* ones on the L_T - γ_p

Table 4.2: Model parameters for 3C 454.3 and 3C 279 states described in the text; R is given in units of 10^{16} cm, n in units of cm^{-3}, B in G, D_d in units of 10^{16} cm, and L_T in erg s^{-1}.

Source	n	γ_p	r	R	Γ	B	D_d	$\dot{m}$	L_T
3C 454.3 (low state)	5	421.5	0.9	71.9	16	0.2	50.9	0.4	3.1×10^{47}
3C 454.3 (high state)	8	425.3	1.0	61.3	16	0.2	51.2	1.0	4.6×10^{47}
3C 279 (low state)	263	130.3	1.1	4.7	15	1.3	4.4	0.3	3.4×10^{46}
3C 279 (high state)	140	137.3	1.1	6.2	15	1.4	24.3	2.7	3.9×10^{46}

plane.

I focused on the pattern derived from recent multi-λ observations of the two FSRQs, 3C 279 and 3C 454.3. I find their flares closely *vertical* on the L_T - γ_p plane to be driven mainly by an increasing flux of the external photons, under further growth of the already substantial *accretion* rates. Meanwhile the electron energies hardly increase, being constrained by the shortening cooling times in the denser radiative field.

These sources add to three BL Lacs that 0716+714, Mrk421 and Mrk501, and complete our picture. I interpret their flares in terms of γ_p increasing under further *acceleration*, to yield patterns *slanted* toward the γ axis; an effect reinforced by saturation of the power L_T due to the limited output extractable from a rotating SMBH via the Blanford-Znajek mechanism (Vittorini et al., 2009; Paggi et al., 2009b).

So I propose the following overall pattern for blazar flares: flaring spectral changes relate to the pre-flare *positions* of BL Lacs and FSRQs on the L_T - γ_p plane, specifically, to their respective branch of the bright blazar strip; this is because the constraints that set such positions are retained or reinforced during the flares. To wit: bright sources lying in the upper branch of the strip flare up almost *vertically* as expected from the cooling constraint to γ, while sources in the lower right branch move almost *horizontally* when luminous, as expected from the BZ constraint to output given their BH masses $M_\bullet \sim 10^8 \div 10^9\, M_\odot$.

Such an overall picture may be tested on more sources with *Fermi* and multi-wavelength data; in particular, it will be fruitful to study any interlopers between gas-rich FSRQs and powerful gas-rich BL Lacs (that is, lower-luminosity FSRQs and the LBLs, low-peaked BL Lacs) during their flares on the L_T - γ_p plane in search of any divide or smooth rotation between these patterns. This may be the case for the BL Lac sources PKS 0537-441, AO 0235+164 and PKS 0426-380, with their weak broad lines and with $\dot{m} \sim 0.1$ (see Ghisellini et al., 2009a) may constitute transitional objects between FSRQs and BL Lacs. Further investigation of such objects will help understanding their nature and their stance in the above picture.

5

Acceleration mechanisms in BL Lacs

5.1 Introduction

Most of TeV detected extragalactic sources are BL Lac objects. They belong to the subclass of "high frequency peaked BL Lacs" (HBLs) exhibiting their spectral energy distributions (SEDs) with a lower energy peak in the X-ray band, interpret as synchrotron emission. Their X-ray spectra are generally curved and well described in terms of a log-parabolic shape. In previous investigations of TeV HBLs two trends between their spectral parameters have been found (Tramacere et al., 2007; Massaro et al., 2008a). (1) the synchrotron peak luminosity L_p increases with its peak energy E_p, (2) the curvature parameter b decreasing as E_p increases. The first is consistent with the synchrotron scenario while the second is expected in statistical/stochastic acceleration mechanisms for the emitting particles. Here, I present an extensive X-ray analysis of a sample of HBLs not detect at TeV energies, observed with *XMM-Newton* and *Swift*, to compare their spectral behavior with that of TeV HBLs. I investigate the distributions of their spectral parameters, providing an interpretation of both E_p and b distributions, in terms of systematic and stochastic acceleration mechanisms. I also compare X-ray spectral behavior of these sources with that in the γ-rays and I outline a criterion to select the best HBLs candidates for the future TeV observations.

As mentioned above, BL Lacs come in two flavors: the "high-frequency peaked BL Lacs" (HBLs) in which the low energy component of the SED peaks between the UV band and X-rays and the "low-frequency peaked BL Lacs" (LBLs), when it appears in the IR-optical range (Padovani & Giommi, 1995b).

In the following, to distinguish between the HBLs detected at TeV energies and those non detected, I introduce the nomenclature referring to the TeV detected objects as TBLs and indicating the others as NBLs.

Using the log-parabolic model the low energy SED of TBLs and NBLs can be described in terms of 3 parameters: the peak frequency E_p, the maximum height of the SED S_p evaluated at E_p or the correspondent peak luminosities $L_p \simeq 4\pi D_L^2 S_p$ and the spectral curvature b around E_p (Tramacere et al., 2007; Massaro et al., 2008a).

Extensive investigations of the TBLs, based on the all X-ray observations present in the archives of *BeppoSAX*, *XMM-Newton* and *Swift* between 1997 and 2007, have shown that several TBLs follow two main correlations in the (E_p, L_p, b) parameter space: (1) the synchrotron peak luminosity L_p increases with E_p, as expected in a simple synchrotron scenario, (2) the curvature parameter b decreases as E_p increases (Massaro et al., 2008a).

In particular, TBLs cover a well constrained region in the $E_p - b$ (hereinafter "acceleration plane") and the trend between b and E_p is evident for the 16 TBLs in (Massaro et al., 2008a), while no clear trend in the $E_p - L_p$ plane has be found for the whole sample.

Many HBLs have been pointed at TeV energies by HESS, Magic and VERITAS, but not all of them have been clearly detected. I noted that 19 out of the 24 TBLs belong to the The Einstein Slew Survey Sample of BL Lacertae Objects (1ES, Perlman et al., 1996), being among the brightest X-ray extragalactic sources, while the others TBLs belong to three different samples, namely: 1) ROSAT All-Sky Survey-Green Bank BL Lac catalog (RGB, Laurent-Muehleisen et al., 1999), 2) The sedentary survey of extreme high energy peaked BL Lacs (SHBL[1], Giommi et al. 2005), 3) The Hubble Space

[1] http://www.asdc.asi.it/sedentary/

Telescope Survey of BL Lacertae Objects (HST, Scarpa et al. 1999; Urry et al. 2000, see also Table 5.1).

Motivated by this observational evidence I selected all the NBLs in the above four samples to search for possible differences between them and the TBLs. I aim at interpreting the distributions of the spectral parameters in both NBLs and TBLs toward establishing a possible criterion to predict the future TeV targets on the basis of the X-ray observations. In addition, I propose an electrostatic acceleration scenario to interpret the distribution of E_p and the maximum energy available in both the TBL and NBL samples.

5.2 Sample selection

To compare the behavior of TBLs and NBLs, I selected a sample of NBLs adopting the following criteria.

- I chose all the sources classified as BL Lac object or BL Lac candidate in the ROMA BZCAT [2] (Massaro et al., 2009, 2010b) that are present in the four samples indicated in Sect. 5.1 excluding the TBLs.
- I compared the ratio between the X-ray and the radio flux Φ_{XR} with the values reported in the ROMA BZCAT. According to the criterion established by Maselli et al. (2010), I select only BL Lacs with $\Phi_{XR} \geq 0.1$, that are classified as HBLs (see also Padovani & Giommi 1995b)
- I restricted my sample to those sources with redshift lower than 0.539, the highest redshift for an extragalactic TeV source (i.e. 3C 279, Albert et al. 2008). Using this cut in redshift, I assumed that any extragalactic source with redshift higher than 0.539 could not be detected at TeV energies, because of the absorption of the extragalactic background light.
- I considered only NBLs with X-ray observations in the *XMM-Newton* or *Swift* archives, with an exposure longer than 700 s, in order to have a good chance of detectability and sufficient number of counts to perform my spectral analysis (see also Massaro et al. 2008a).

The number of NBLs in the considered sample is 119, spanning a range of redshift between 0.048 and 0.529. However, there are 79 NBLs have been excluded adopting my criteria, for a remaining number of 40 NBLs with a total of 99 X-ray observations (92 observations in the *Swift* archive and 7 in that of *XMM-Newton*, respectively). We also note that only 19 NBLs out the total 40 selected targets have been detected and identified by *Fermi* during the first year as reported in the 1st catalog (Abdo et al., 2010a).

In Table5.1, the number of object in each sample is reported. I report the number of BL Lac identified in the ROMA BZCAT (col. 1), the highest value of the redshift for the sample (col. 2), the number of TBLs in the sample (col. 3), the number of BL Lacs without a redshift estimate (col. 4), the number of HBLs present (col. 5) and the NBLs selected applying the criteria described above defined above (col. 6).

In Table 5.2, the general informations of all selected NBLs with X-ray observations are reported. I indicate both the ROMA BZCAT name (col. 1) and sample name (col. 2), the coordinates (col. 3 and col. 4), the redshift (col. 5, see Massaro et al. 2010b), the luminosity distance D_L (col. 6), the value of the Galactic column density $N_{H,Gal}$ (col. 7, see Kalberla et al. 2005), the X-ray to radio flux ratio Φ_{XR} (col. 8) and the number of both *XMM-Newton* and *Swift* observations (col. 9 and col. 10 respectively). The sources marked with a (*) close to the ROMA BZCAT name are those identified in the first year *Fermi* catalog (Abdo et al., 2010a).

[2] http://www.asdc.asi.it/bzcat/

Table 5.1: The properties of the BL Lac samples.

Sample	Total	z_{max}	TBLs	no z	HBLs	Sel.
1ES	55	0.940	18	11	46	15
HST	94	0.940	19	10	57	26
SHBL	122	0.702	9	43	122	63
RGB	109	0.664	7	26	70	32

Col.(1) Total number of BL Lacs in the sample. Col.(2) Highest value of the redshift in the sample. Col.(3) Number of TBLs present in the sample. Col.(4) Number of BL Lac without redshift estimate. Col.(5) Number of HBLs in the sample. Col.(6) Number of NBLs selected.

Finally, I did not analyze the two NBLs: BZB J0333-3619 and BZB J0613+7107. These sources are in the FOV of two deeply observed Seyfert galaxies: NGC 1365 and Mrk 3, respectively. A separate paper, including their *Chandra* observations, is in preparation.

5.3 Data reduction procedures

The reduction procedure for *XMM-Newton* data follows that described in Tramacere et al. (2007) and more details on both the *XMM-Newton* and *Swift* data reduction procedures can be found in Massaro et al. (2008a) and Massaro (2008b). In the following subsections I report only the basic details.

5.3.1 XMM-Newton observations

Our sources were observed with *XMM-Newton* by means of all EPIC CCD cameras: the EPIC-PN (Strüder et al., 2001), and EPIC-MOS (Turner et al., 2001).

Extractions of all light curves, source and background spectra were done with the *XMM-Newton* Science Analysis System (SAS) v6.5.0. The Calibration Index File (CIF) and the summary file of the Observation Data File (ODF) were generated using Updated Calibration Files (CCF) following the "User's Guide to the *XMM-Newton* Science Analysis System" (issue 3.1, Loiseau 2004) and "The *XMM-Newton* ABC Guide" (vers. 2.01, Snowden et al. 2004). Event files were produced by the EMCHAIN pipeline.

Light curves for each dataset are extracted, and all high-background intervals filtered out to exclude time intervals contaminated by solar flares. Then by visual inspection I selected good time intervals far from solar flare peaks and with no count rate variations on time scales shorter than 500 seconds. Photons are extracted from an annular region using different apertures to minimize pile-up, which affects MOS data. The mean value of the external radius used for the annular region is 40 $''$.

A restricted energy range (0.5–10 keV) is used to account for residual calibration uncertainties. To ensure the validity of Gaussian statistics, data have grouped by combining instrumental channels so that each new bin contains 30 counts or more.

5.3.2 Swift observations

The XRT data analysis was performed with the XRTDAS software (v. 2.1), developed at the ASI Science Data Center (ASDC) and included in the HEAsoft package (v. 6.0.2). Event files were calibrated and cleaned with standard filtering criteria using the XRTPIPELINE task.

Events in the energy range 0.3–10 keV with grades 0–12 (photon counting mode, PC) and 0–2 (windowed timing mode, WT) are used in the analyses (see Hill et al. 2004 for a description of readout modes, and Burrows et al. 2005 for a definition of XRT event grades). For the WT mode data, events

Table 5.2: NBLs selected (00 – 24 hh).

BZCAT Name	Other Name	RA (J2000)	DEC (J2000)	z	D_L [Mpc]	$N_{H,Gal}$ [$10^{20} cm^{-2}$]	Φ_{XR}	*Swift*	*XMM-Newton*
BZB J0123+3420	1ES 0120+340	01 23 08.5	+34 20 47.0	0.272	1359.7	5.20	5.74	13	1
BZB J0152+0147	RGB J0152+017	01 52 39.5	+01 47 17.0	0.080	354.0	2.67	0.51	10	—
BZB J0201+0034	1ES 0158+003	02 01 06.1	+00 34 00.0	0.298	1511.2	2.23	2.71	1	—
BZB J0208+3523*	1RXS J020837.5+35231	02 08 38.2	+35 23 13.0	0.318	1629.9	6.27	5.76	—	2
BZB J0214+5144	RGB J0214+517	02 14 17.8	+51 44 52.0	0.049	212.0	14.4	0.16	3	—
BZB J0325-1646*	1RXS J032540.8-16460	03 25 41.1	-16 46 14.9	0.291	1470.1	3.27	10.1	1	—
BZB J0326+0225*	1ES 0323+022	03 26 13.9	+02 25 14.0	0.147	681.2	7.87	1.77	3	1
BZB J0441+1504	1RXS J041112.1-39413	04 41 27.4	+15 04 54.0	0.109	492.3	14.0	7.28	1	1
BZB J0442-0018*	1RXS J044229.8-00182	04 42 29.8	-00 18 34.9	0.449	2453.2	4.83	3.35	2	—
BZB J0621-3411	1RXS J062150.0-34114	06 21 49.4	-34 11 53.9	0.529	2991.5	4.08	2.30	1	—
BZB J0744+7433*	1ES 0737+746	07 44 05.2	+74 33 56.9	0.314	1606.0	3.28	2.74	—	2
BZB J0751+1730	1RXS J075124.3+17304	07 51 25.0	+17 30 51.0	0.185	878.4	4.93	1.78	1	—
BZB J0847+1133*	1RXS J084713.3+11334	08 47 12.8	+11 33 50.0	0.199	953.2	3.17	3.34	1	—
BZB J0916+5238	RGB J0916+526	09 16 51.8	+52 38 27.9	0.190	905.0	1.43	0.53	1	—
BZB J0952+7502	1RXS J095225.8+75021	09 52 24.1	+75 02 12.9	0.179	846.8	2.23	2.07	2	—
BZB J1010-3119	1RXS J101015.9-31190	10 10 15.9	-31 19 08.0	0.143	660.9	8.48	1.37	3	—
BZB J1022+5124	1RXS J102212.5+51240	10 22 12.6	+51 23 59.9	0.142	655.9	1.02	6.88	1	—
BZB J1053+4929*	RGB J1053+494	10 53 44.0	+49 29 56.0	0.140	645.8	1.50	0.13	1	—
BZB J1056+0252	1RXS J105607.0+02521	10 56 06.6	+02 52 13.0	0.236	1155.7	3.82	17.3	1	—
BZB J1111+3452	1RXS J111131.2+34521	11 11 30.7	+34 52 02.9	0.212	1023.5	1.64	5.71	1	—
BZB J1117+2014*	1RXS J111706.3+20141	11 17 06.1	+20 14 08.0	0.139	640.7	1.35	3.26	1	—
BZB J1136+6737*	1136+676	11 36 29.9	+67 37 04.0	0.136	625.7	1.09	3.28	5	—
BZB J1145-0340	1RXS J114535.8-03394	11 45 35.1	-03 40 00.9	0.167	784.0	2.22	2.28	2	—
BZB J1231+6414	1229+643	12 31 31.3	+64 14 17.9	0.163	763.3	2.12	0.43	—	2
BZB J1237+6258	1RXS J123739.2+62584	12 37 38.9	+62 58 41.9	0.297	1505.3	0.97	1.90	12	2
BZB J1253-3931	1RXS J125341.2-39320	12 53 41.2	-39 31 59.0	0.179	846.8	7.66	1.47	1	—
BZB J1257+2412	1ES 1255+244	12 57 31.9	+24 12 39.9	0.141	650.8	1.25	5.16	1	2
BZB J1341+3959*	RGB J1341+399	13 41 05.1	+39 59 44.9	0.172	810.0	0.80	1.26	2	—
BZB J1417+2543*	1RXS J141756.8+25432	14 17 56.5	+25 43 26.0	0.237	1161.3	1.54	1.72	5	—
BZB J1439+3932*	1RXS J143917.7+39324	14 39 17.5	+39 32 42.0	0.344	1787.1	1.14	2.64	2	—
BZB J1442+1200*	1ES 1440+122	14 42 48.1	+12 00 39.9	0.163	763.3	1.58	1.13	3	—
BZB J1534+3715	RGB J1534+372	15 34 47.2	+37 15 54.0	0.143	660.9	1.33	0.10	2	—
BZB J1605+5421	1RXS J160518.5+54210	16 05 19.0	+54 21 00.0	0.212	1023.5	0.89	5.53	1	—
BZB J1728+5013*	1728+502	17 28 18.5	+50 13 09.9	0.055	239.0	2.35	1.01	3	—
BZB J1743+1935*	1ES 1741+196	17 43 57.7	+19 35 08.9	0.080	354.0	7.36	0.14	1	—
BZB J2131-0915*	1RXS J213135.5-09152	21 31 35.3	-09 15 21.9	0.449	2453.2	3.62	1.74	1	—
BZB J2250+3824*	RGB J2250+384	22 50 05.7	+38 24 37.0	0.119	541.2	10.4	0.24	4	—
BZB J2308-2219	1RXS J230846.7-22195	23 08 46.8	-22 19 49.0	0.137	630.7	1.86	7.12	1	—
BZB J2322+3436*	RGB J2322+346	23 22 43.9	+34 36 14.0	0.098	439.3	6.83	0.11	1	—
BZB J2343+3439*	1RXS J234332.5+34395	23 43 33.5	+34 39 48.9	0.366	1922.6	6.75	1.60	2	—

Col. (1) ROMA BZCAT source names. Col. (2) the name in the selected sample. Cols.(3,4) the right ascension and declination, respectively. Col. (4) gives the redshift (from ROMA BZCAT). Col. (5) reports the luminosity distance. Cols. (6) the Galactic column density along the line of sight (Kalberla et al., 2005). Col. (8) the X-ray to radio flux ratio Φ_{XR} (see Sect. 5.2). Cols. (9,10) report the number of X-ray observations per satellite. (*) indicates that the BL Lac has been detected by *Fermi*-LAT.

were selected for temporal and spectral analysis using a 40 pixel wide (1 pixel = 2.36 ") rectangular region centered on the source, and aligned along the WT one dimensional stream in sky coordinates. Background events were extracted from a nearby source-free rectangular region of 40 x 20 pixels.

For PC mode data, when the source count rate is above 0.45 counts s^{-1} the data are significantly affected by pile-up in the inner part of the point spread function (PSF) (e.g. Perri et al., 2007). To remove the pile-up contamination, I extract only events contained in an annular region centered on the source. The inner radius of the region was determined comparing the observed PSF profiles with the analytical model derived by Moretti et al. (2005), and typically has a 4 or 5 pixels size, while the outer radius is 20 pixels for each observation. For *Swift* observations in which the source count rate was below the pile-up limit, events are instead extracted using a 20 pixel radius circle. The background for PC mode is estimated from a nearby source-free circular region of 20 pixel radius.

Source spectra are binned to ensure a minimum of 30 counts per bin in order ensure the validity of χ^2 statistics.

5.4 X-ray Spectral analysis

I performed my spectral analysis primarily with the *Sherpa* [3] modeling and fitting application (Freeman et al., 2001) and the XSPEC software package, version 11.3.2 (Arnaud, 1996) as a secondary check of my results.

I describe the X-ray continuum with different spectral models: 1) an absorbed power-law with column density either free, or fixed at the Galactic value $N_{H,Gal}$; 2) a log-parabolic model (LP) (Landau et al., 1986; Massaro et al., 2004b); 3) a power-law with an exponential cutoff (PEC) with a new expression as described in the following; In all models with fixed Galactic column density, I use $N_{H,Gal}$ values from the LAB survey (Kalberla et al., 2005) reported in Table 5.2.

The LP model fitted using the following expression:

$$F(E) = K\, E^{-a-b\ log(E)}\ , \tag{5.1}$$

and also adopting the equivalent SED representation already used by Tramacere et al. (2007) and Massaro et al. (2008a) expressed as:

$$F(E) = \frac{S_p}{E^2}\ 10^{-b\ log^2(E/E_p)}\ , \tag{5.2}$$

with $S_p = E_p^2\, F(E_p)$. Both LP model representations are in units of $[photons\ cm^{-2}\ s^{-1}\ keV^{-1}]$. In particular, using fits to Eq. 5.2, the values of the parameters E_p (the location of the SED energy peak), S_p (the peak height), and b (the curvature parameter) can be estimated independently in the fitting procedure (Massaro et al., 2006; Tramacere et al., 2007).

I used the following expression to define the PEC model:

$$F(E) = \frac{S_p}{E^2}\left(\frac{E}{E_p}\right)^a exp\left[1 - \frac{E}{E_p}\right]^{(a+2)}\quad . \tag{5.3}$$

Adopting Eq. 5.3 during a fitting procedure the three parameters: E_p, S_p and the photon index a, can be evaluated independently, this allow us to investigate possible correlations among them, as for the LP function, without the introduction of functional biases.

Analyses of long exposure observations were performed using time-resolved spectra, as described in Tramacere et al. (2007), to avoid averaging significant spectral variations while still having a sufficient number of counts per observation to evaluate the spectral curvature.

[3] http://cxc.harvard.edu/sherpa/

The results of our fitting procedures are reported in App. C; the statistical uncertainties quoted refer to the 68% confidence level (one Gaussian standard deviation).

In some cases, poor statistics (due to short observational exposures or low source count rate) or restricted instrumental energy range, combined with the location of the E_p outside the observational energy range, make difficult to evaluate a possible spectral curvature, consequently the single power-law model constitutes an acceptable description of the X-ray spectra.

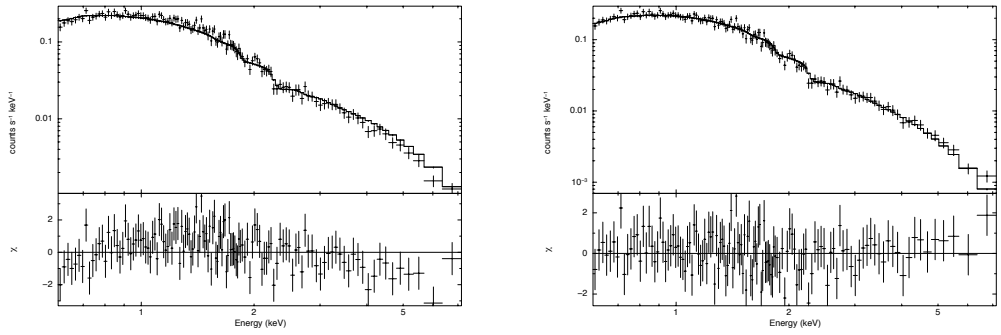

Figure 5.1: *XMM-Newton* spectrum of BZB J0208+3523 performed on Feb. 14, 2001 (Obs. ID 0084140101). *Left*: the systematic deviations on both sides of the residuals from a best fit power-law with fixed $N_{H,Gal}$ show the need of intrinsic curvature. *Right*: the deviations disappear with the LP model with fixed $N_{H,Gal}$.

5.5 Results

5.5.1 X-ray properties

I present the results of the X-ray spectral analysis performed on the NBL sample in comparison with the known X-ray spectral behavior of TBLs (see Massaro et al., 2008a).

I excluded the case of PKS 2155-204 between the TBLs, because this source showed a high energy component dominating the low energy one in several occasions, being more similar to a flat spectrum radio quasars than a HBL. In addition, for our comparison between TBLs and NBLs I also excluded Mrk 421, because having at least ten times the number of X-ray observations than the other TBLs could dominate the parameter distributions.

Finally, for the comparison of the average X-ray spectral behavior of TBLs and NBLs I also excluded from our analysis the giant flare of Mrk 501 in 1997 (Massaro et al., 2006) and that of 1H 1426+428 (Massaro et al., 2008a), because I am interested in investigating the average spectral behavior, not considering rare, giant, flaring episodes.

My results can be summarized as follows:

- Adopting the absorbed power-law model to describe the NBL X-ray spectra I obtained unacceptable values of χ^2_r (i.e. $\chi^2_r \geq 1.5$); even when I leave the intrinsic low energy absorption as a free parameter, mainly because these models are not adequate to describe the high energy tail of their X-ray spectra above ~ 4 keV (see Fig. 5.1 for more details).

This result is in agreement with the X-ray spectral analysis of TBLs that appear to be featureless over a broad energy range (Giommi et al., 2005; Perri et al., 2007; Tramacere et al., 2007; Massaro et al.,

2008a). Absence of spectral features related to any absorbing material was also confirmed by Blustin et al. (2004), using the *XMM-Newton* RGS spectra.

- Both the LP and the PEC models provides acceptable χ^2_r values for all the NBLs (see appendix A) and none of these models can be favored with respect to the other in terms of χ^2_r and residual distribution.

However, it is remarkable that the E_p values derived using the PEC model have larger uncertainties with respect to those derived with LP function, this is due to the fact that for the PEC model, E_p is directly related to the exponential cut-off that in the fitting procedure depends only by the high energy tail of the X-ray spectra, typically not well sampled.

On the other hand, LP model provides a systematic better description than PEC function for the TBL X-ray spectra (Massaro et al., 2008a)).

- The E_p distribution of the NBLs is similar to that of TBLs, exhibiting a peak around the value of $\sim$ 1.5 keV. However, the E_p distribution of NBLs do not show values larger than $\sim$ 3 keV while these are present, even if in few cases for TBLs. The comparison between these distributions is reported in Fig. 5.2, appearing to be different only above the E_p value of 1.75 keV. The D variable of the Kolmogorov-Smirnoff (KS) test (i.e. D_{KS}) has a value of 0.07, so the two distributions are equal within an interval of confidence of 1%.

Identifying X-ray flares of HBLs as a state in which both the E_p and the L_p are increasing with respect to the average values, the presence of few high values of E_p suggests that TBLs are more variables than NBLs.

- There is a systematic difference in the spectral curvature between TBLs and NBLs. Their distributions of b are reported in Fig. 5.3 for comparison. It is clear that the curvature in NBLs is systematically higher than in TBLs, indicating that the NBL X-ray spectra are narrower around E_p than those of TBLs. Applying a KS test, D_{KS}) has a value of 0.42, so the two distributions are different within a level of confidence of 90%.

This is also confirmed by the X-ray spectral analysis that provides acceptable χ^2_r values when the PEC model is adopted for the HBL X-ray observations with detectable spectral curvature.

- There is no clear trend evident for the NBLs in the acceleration plane, while, as shown in Massaro et al. (2008a), TBLs follow a correlation between E_p and b: the energy peak E_p increases as the spectral curvature b decreases.

- There is no significant trend between L_p and b in the NBL sample, a similar behavior shown by TBLs (Massaro et al., 2008a).

All the correlation coefficients evaluated between spectral parameters are lower than 0.1 for both LP and PEC models.

- The X-ray fluxes derived from our analysis of NBLs are consistent with those measured by previous X-ray ROSAT observations (ROMA BZCAT, Massaro et al. 2010b), suggesting that NBLs are less variable than TBLs.

5.5.2 γ-ray properties

The number of TBLs known is 24; and the majority of them, 19 out of 24, has been also detected in the *Fermi*-LAT energy range (30 MeV - 100 GeV), as reported in the first year *Fermi* catalog (Abdo et al.,

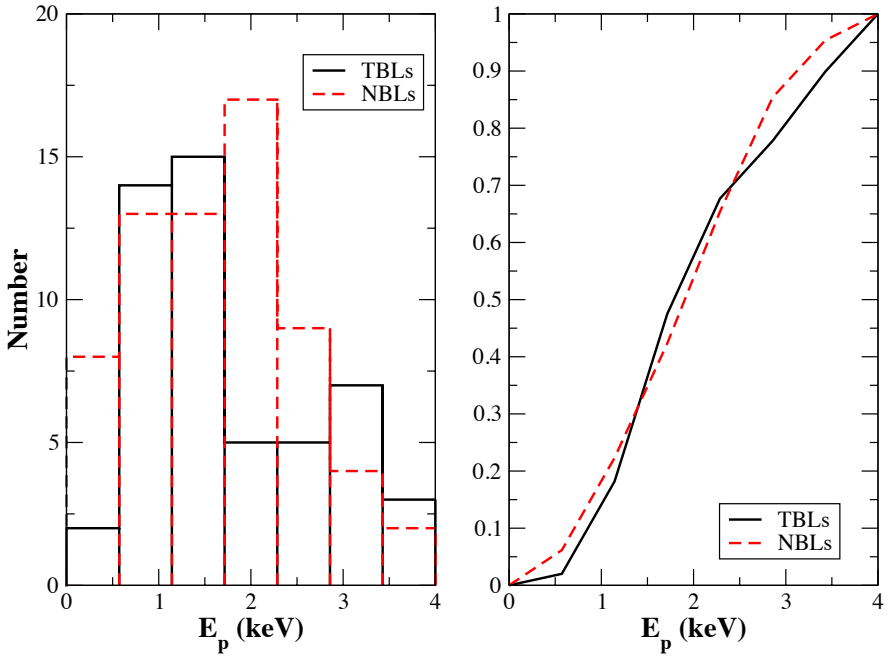

Figure 5.2: The X-ray E_p distribution of NBLs (red) and TBLs (black). The sample of TBLs is plotted excluding Mrk 421 and PKS 2155-304 and giant flares of Mrk 501 and 1H 1426+421, as described in Sect. 5.5.

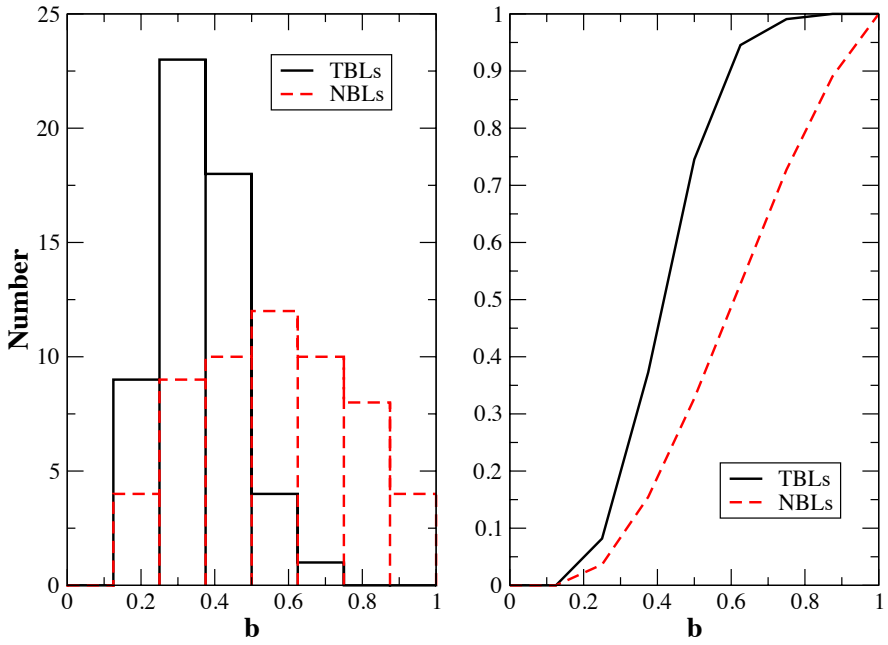

Figure 5.3: The X-ray *b* distribution of NBLs (red) and TBLs (black). The sample of TBLs is plotted considered excluding Mrk 421, PKS 2155-304 and the giant flares of Mrk 501 and 1H 1426+421, as described in Sect. 5.5.

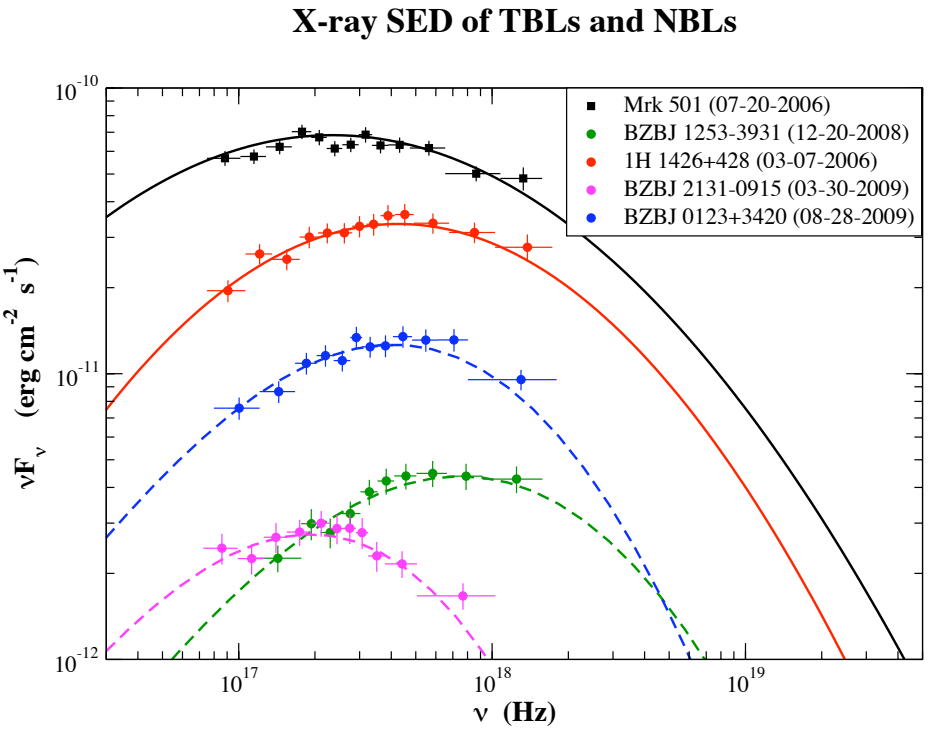

Figure 5.4: The SEDs for three observations of the NBLs: BZB J 0123+3420 (magenta), BZB J 1253-3931 (green) and BZB J 2131-0915 performed with *Swift* in comparison with two archival observations of the TBLs: Mrk 501 (black) and 1H 1426+428 (red) (see Massaro et al., 2008a) for more details). It appears evident that both in the low and in the high states the TBLs are broader than the NBLs. The dashed lines represent the LP bestfit model for the NBLs while the straight lines that of TBLs.

2010a). I searched the *Fermi* catalog for detection of the NBLs and I found that only ~ 20% (24 out of 119) were detected. I found no difference between the distribution of the γ-ray spectral index between the TBLs and NBLs detected by the *Fermi*-LAT. However, there is a marginal indication that the NBLs appear to be less luminous than TBLs, in particular at low redshift. The γ-ray luminosity L_γ for all the sources is shown in Fig. 5.5 with respect to their redshift.

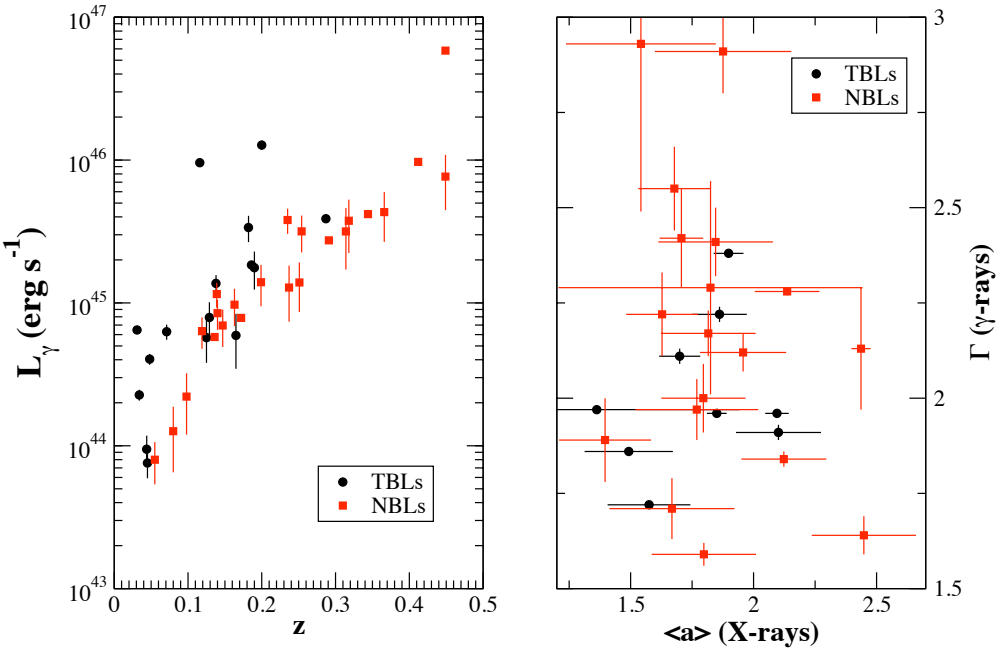

Figure 5.5: The γ-ray luminosity for NBLs (red squares) and TBLs (black circles) evaluated using the γ-ray fluxes reported in the first year *Fermi* catalog (Abdo et al., 2010a). The γ-ray photon index Γ for NBLs (red square) and TBLs (black circles) with respect to the mean X-ray photon index a evaluated averaging its values during the non flaring states.

In the same figure I report the γ-ray photon index Γ with respect to the average X-rays photon index of with the LP model $< a >$ weighted with their variance. I did not find any difference in the indices plot between the different sample of HBLs and TBLs. Then I conclude that the spectral γ-ray behavior of the NBLs with respect to the TBLs detected by the *Fermi*-LAT appears the same.

5.6 TeV detectable HBLs

Comparing the distribution of the X-ray spectral curvature and the *Fermi*-LAT detection, I outline a possible criterion to predict the NBLs that could be detectable at TeV energies.

I argue that only NBLs with a curvature comparable to that of TBL objects $b < 0.5$ (corresponding to the maximum distance between the two cumulative b distributions, see Fig. 5.3) with a *Fermi*-LAT detection are the best candidates for the future TeV observations. From my analysis I found that BZB J0326+0225, BZB J2250+3824 and BZB J1743+1953 are the possible new TeV detectable

extragalactic sources because they always satisfied the above criteria. In addition, BZB J1136+6737, BZB J1417+2543, BZB J1442+1200, BZB J1728+5013 show a similar X-ray spectral behavior being TeV candidates.

However, this criterion suffers of one common problem of BL Lac observations: the temporal variability. HBL sources, both TBLs or NBLs, could be variable and could show curvature variations on different time scales, up today unknown. Consequently, I expect the discovery of new HBLs at TeV energies if the X-ray spectrum shows a curvature with $b \geq 0.5$, with γ-ray detection in the *Fermi*-LAT energy range, quasi-simultaneously with the TeV observation.

5.7 Systematic acceleration in BL Lac objects

I propose an acceleration scenario to explain the E_p distribution around the value of a few keV for both NBLs and TBLs.

In the following, I assume that the acceleration mechanisms occurring in BL Lac jets are a combination of systematic acceleration, responsible for the energy peak position of the particle energy distribution (PED), and stochastic acceleration, which accounts for the broadening of the PED around its peak.

In addition, I consider the inverse Compton radiative losses negligible with respect to those of the synchrotron emission. This is supported by the observational lack of the inverse Compton dominance in the BL Lac SEDs (e.g. the recent TBL PKS 0548-322, Aharonian et al. 2010).

I am also considering the BL Lac jet emission dominated by electrons, neglecting hadronic components.

According to Cavaliere & D'Elia (2002), BL Lac jets could be powered by the Blandford & Znajek (BZ) mechanism (1977), i.e. the extraction of rotational energy from a spinning supermassive black hole via the Poynting flux associated with the surrounding magnetosphere.

The force-free condition $\underline{E} \cdot \underline{B} = 0$ governing these magnetospheres breaks down when the electric field $E \leq B$. Electric fields parallel to magnetic fields can accelerate charged particles as a result of magnetic field reconnection in a current sheets (e.g. Litvinenko 1996, 1999). Consequently, the systematic acceleration mechanism is electrostatic. However, these electric fields are electrodynamically screened out beyond distances that exceed the Debye length, λ_D. For a pair plasma λ_D is defined as:

$$\lambda_D = \frac{c}{\omega_p} = \left(\frac{\gamma_p \, m_e \, c^2}{4\pi \, e^2 \, n} \right)^{1/2} = 5.30 \cdot 10^6 \left(\frac{\gamma_p}{n} \right)^{1/2} \; cm. \tag{5.4}$$

where ω_p is the plasma frequency, γ is the characteristic electron Lorentz factor, m_e is the electron mass, e its electric charge, c the speed of light, B the magnetic field, and n the electron density.

Consequently, in a BZ magnetosphere the particle energy gain for each acceleration step can be written as:

$$\gamma_p \, m \, c^2 = e \, B \, d \simeq e \, B \, \lambda_D. \tag{5.5}$$

Substituting Eq. 5.4 in Eq. 5.5 I obtain an expression for the Lorentz factor of the accelerated particle:

$$\gamma_p = \frac{1}{4 \, \pi \, m \, c^2} \left(\frac{B^2}{n} \right) = 9.77 \cdot 10^4 \left(\frac{B^2}{n} \right). \tag{5.6}$$

The above expression is similar to the assumption that the electron energy density $u_e \sim n \, \gamma_p \, m \, c^2$ is half of the magnetic energy density $u_B = \frac{B^2}{8\pi}$, which is close to the equipartition condition.

For a beaming factor $\delta \sim 10$, typical of a HBL (REF), the peak energy of the synchrotron emission for an electron of Lorentz factor $\gamma_p \sim 10^5$ lies in the X-ray band (assuming $n \sim 1$ cm^{-3} and $B \sim 1$ G, typical for a HBL (REF)).

The maximum energy extractable by a particle of Lorentz factor 10^5 is ~ 0.05 TeV, so considering $\delta \simeq 10$, I expect the peak of the inverse Compton emission around ~ 0.5 TeV. This is consistent with

all TBL observations having a γ-ray photon index typically ≥ 2 in the TeV energy range, implying that the energy peak of their high energy component lies below a few TeV.

Adopting the above scenario, the energy gain by electrostatic acceleration for a single relativistic electron in a magnetic field, B, can be written in the form:

$$\left(\frac{dE}{dt}\right)_{acc} = e\,B\,c\,, \tag{5.7}$$

and the synchrotron radiative losses are:

$$\left(\frac{dE}{dt}\right)_{sync} = -\frac{4}{3}\,\sigma_T\,c\,\gamma^2\,\frac{B^2}{8\pi}, \tag{5.8}$$

where σ_T is the Thomson cross-section.

The maximum electron Lorentz factor γ_{max} that can be reached by a single electron corresponds to the situation when the synchrotron losses are balanced by the electrostatic acceleration:

$$\gamma_{max} = \left(\frac{3\,e}{2\,\pi\,\sigma_T\,B}\right)^{1/2} = 1.86 \cdot 10^7 B^{-1/2}, \tag{5.9}$$

that depends on B which has a typical value for HBLs of $\sim$ 1 G. Hence, the maximum energy available in the electrons is of the order of $\gamma_{max}\,m\,c^2 \sim 1$ TeV.

The synchrotron loss length l_{syn} is:

$$l_{syn} \simeq c\,\tau_{syn} = 1.51 \cdot 10^{19}\gamma^{-1}B^{-2}cm \tag{5.10}$$

where τ_{syn} is the synchrotron cooling time. For the characteristic $\gamma_p \sim 10^5$ moving in a magnetic field of $\sim$ 1G, $l_{syn} \sim 10^{14}$ cm, of the same order of the emitting size region derived from the HBL timescale variability.

The total intrinsic luminosity, L_{int} of a current sheet that is accelerating the electrons can be estimated from its Poynting flux in the form:

$$L_{int} = \frac{1}{2\pi}\,B^2\,c\,\cdot\,(l_{cs}\,w), \tag{5.11}$$

where w and l_{cs} are the current sheet width and its length, respectively (Litvinenko, 1999).

Assuming that $l_{cs} \sim w \sim l_{syn}$, for B of the order of 1 G, I find an intrinsic luminosity $L_{int} \sim 10^{40}$ erg s^{-1} for each reconnection region. Consequently, a number of reconnections ranging between 10 and 100 can explain the total intrinsic luminosity of NBLs and TBLs, as for $\delta \sim 10$, I get a total observed luminosity of 10^{45} - 10^{46} erg s^{-1} as measured (e.g. Massaro et al., 2008a) for the TBLs and in this work for the NBLs).

Finally, I remark that a similar scenario has been successfully adopted in the single pulses of GRB jets (Massaro & Grindlay submitted).

5.8 Stochastic acceleration in TBLs and NBLs

The observational evidence that NBLs have a systematically higher curvature than TBLs could be interpreted in terms of more efficient acceleration mechanisms occurring in their jets.

The general solution of the kinetic equation, time and energy dependent, yields log-normal (i.e. log-parabolic) PEDs, where only systematic (e.g. electrostatic) and stochastic (e.g. turbulence) acceleration are considered (Kardashev, 1962). Recently, it has been shown that including synchrotron and inverse Compton radiative losses, as well as the loss of particles escaping from the acceleration

region, numerical solutions for the kinetic equation again give PED close to a log-parabolic function (e.g. Tramacere et al. 2009; Paggi et al. 2009a).

According to this scenario, the curvature parameter of the PED is only related to the stochastic acceleration term (e.g. Kardashev 1962; Stawarz & Petrosian 2008; Tramacere et al. 2009; Paggi et al. 2009a). PED and consequently synchrotron SED where the stochastic acceleration is more efficient are broader with respect to those in which the stochastic term is negligible. In addition, radiative cooling effects due to synchrotron and inverse Compton radiation should make the observed SED narrower (e.g. Massaro et al., 2006).

Assuming that there is no difference of beaming factor between TBL and NBL jets and that particles in NBL jets are less confined than in TBLs, because less subject to the stochastic acceleration, I argue that the emitting region is larger in NBLs than in TBLs. The X-ray peak luminosities, proportional to the number of emitting electrons, has the same distribution in NBLs and TBLs, so the density of NBLs is expected to be lower than in TBLs if the size of the emitting region is larger. Consequently, NBLs, being less dense sources than TBLs, will emit a lower flux for the inverse Compton component at TeV energies. This idea is supported by the low γ-ray luminosity observed in NBLs with respect to the TBL sample.

The combination of a narrower SED and a lower flux in the TeV energy range makes more difficult to detect the NBLs in the TeV energy range. On the other hand, the inferred higher values of their size for the emitting region in NBL rather than in TBLs predict longer variability time scales. This is in agreement with the lack of giant X-ray flares found in the whole sample of NBLs observations analyzed in this work.

5.9 Discussion

I carried on an extensive X-ray spectral analysis of HBLs to compare the spectral behavior of those TeV non detected (NBLs) with those already known as TeV emitters (TBLs).

I found that the E_p distributions of NBLs and TBLs are similar, suggesting that the same systematic acceleration scenario is working in these sources. In particular, the E_p distribution appear to be symmetric around a value of few keV for both subclasses.

I assumed that the electrons accelerated in their relativistic jets, both under stochastic and systematic acceleration mechanisms, emit mainly via synchrotron emission and that the stochastic acceleration is only responsible for the spectral broadening (i.e. curvature) around E_p, while the E_p mean position is due to the systematic acceleration. In fact, the curvature of the PED is only dependent by the stochastic acceleration term, while the γ_p is mostly affected by the systematic acceleration terms (e.g. Tramacere et al. 2009; Paggi et al. 2009a).

Under these assumptions, I propose an electrostatic acceleration scenario and I derived the characteristic Lorentz factor for the emitting electron of $\gamma_p \sim 10^5$. This corresponds to the average value of E_p of few keV for the typical values of electron density, magnetic field and beaming factor of HBLs.

Investigating the comparison between the X-ray spectral curvature b of NBLs and TBLs, I found that this is systematically lower than in TBLs, implying that the NBL X-ray spectra are narrower. I argued that a possible interpretation of this effect could be more efficient stochastic acceleration in TBLs than in NBLs. This is supported by their X-ray spectra well described also with the PEC model and not only with the LP function.

In addition, using the recent *Fermi*-LAT observations of the NBLs in my sample, reported in the 1st year *Fermi* catalog (Abdo et al., 2010a), I found that there are no differences between NBL and TBLs in terms of γ-ray spectral index or γ-ray flux distributions. Only a small fraction of NBLs has been detected in the-LAT energy range.

On the basis of my analysis, I developed a criterion to search future TBLs. However, to have a more complete understanding of the two different subclasses, HBLs and TBLs, more and longer X-ray observations are necessary. In particular, a crucial test for my criterion would be a long monitoring

of two candidates in the different samples to investigate the variability time scales of their spectral curvature.

6

Summary and Conclusions

Making use of the log-parabolic model to describe BL Lac spectra, I refined the classic one-zone SSC model (based on power law emissions), in order to investigate its very limits; in this view, BL Lac may be conveniently ordered in a succession spanning from smooth variations of one or a few dominant SSC parameter, up to the appearance of truly different components that ultimately break through the limits of the simple model, as shown Chapter 3. Even more so at increasing energies and frequencies, that would imply weaker and weaker γ-ray fluxes relative to X-ray, owing to KN cross section effects. This yields a weak γ-ray variability on average for these sources, and leads to expect for the majority of the sources either reduced flare activity in this band, or weak average fluxes, relating these features to reduced Klein-Nishina cross section that tends to limit both the average fluxes and the flares.

Moreover, the model lead me to interpret the spectral variations of flaring BL Lacs in terms of increased *acceleration* of particles *inside* the jets; the situation changes when we look at FSRQs, where higher accretion onto the central black hole affect both the spectral behavior and the energetic of the flares. In fact, for dry BL Lacs discussed in Chapter 4, with accretion rates $\dot{m} < 10^{-2}$, the outputs appear to be effectively gauged in terms of the maximal power extractable from the central black hole via the enticing Blandford-Znajek electodynamical mechanism, and their flares appear to be constrained in this way. FSRQs, on the other hand, may easily overcome this limit, due abundant surrounding gas, and are therefore free in power increases during flares; moreover, those flare appear to be driven by increased *accretion* rates $\dot{m} \sim 1$, that is, increased energy coming from *outside* the jets. Therefore, the physical dichotomy in Blazars sources is reflected in the flaring patterns on a jet luminosity vs. electron energy plane; on such a plane Blazar bright states strung along a stripe of increasing luminosity and accretion rates and decreasing particle energies, that is, from luminous, farther FSRQs to fainter, closer HBLs. The flaring behavior of Blazars can be related to their position on this strip, with FSRQs moving almost vertically, mainly driven by their strong accretion rates, and with powerful dry BL Lacs, constrained to move in a slanted way by their poorly powered engines, and so mainly driven in their flares by acceleration of the emitting particles.

These acceleration processes can be investigated with the quiescent activity of BL Lacs; in Chapter 5 I showed the results of an extensive X-ray spectral analysis of HBLs not yet detected at TeV energies, in order to compare them with the other detected at such energies. The similar peak frequency distributions in the two populations yield to similar *systematic* accelerations, understandable with a simple, electrostatic model; but the strong differences in the spectral curvatures lead different *stochastic* acceleration efficiencies. In particular, while both population are able to accelerate electrons about up to the same *energies*, HBL not detected at TeV are not enough efficient stochastic accelerators in order emit substantial *flux* at such energies; sources providing such an efficiency are therefore strongly suspected to be the next TeV detected BL Lacs.

My overall picture will be tested on more sources with *Fermi* and multi-wavelength data; in particular, it will be fruitful to study any interlopers between gas-rich FSRQs and powerful gas-rich BL Lacs (that is, lower-luminosity FSRQs and the LBLs, low-peaked BL Lacs) during their flares on the L_T - γ_p plane in search of any divide or smooth rotation between these patterns. This may be the case for the BL Lac sources PKS 0537-441, AO 0235+164 and PKS 0426-380, with their weak broad lines and with $\dot{m} \sim 0.1$ may constitute transitional objects between FSRQs and BL Lacs. Further investigation of such objects will help understanding their nature and their stance in the above picture.

Appendix A

Radiation and acceleration processes

A.1 General definitions

A population of energetic particles is described by its differential energy distribution

$$N(\gamma) = \frac{dn}{d\gamma} \left[\mathrm{cm}^{-3}\right], \tag{A.1}$$

where $n \left[\mathrm{cm}^{-3}\right]$ is the particle number density and $\gamma = E/mc^2$ is the particle total adimensional energy, so that $N(\gamma)\, d\gamma$ is the density of particles with energy between $\gamma\, mc^2$ and $(\gamma + d\gamma)\, mc^2$; particle density and particle energy distribution are obviously related by

$$n = \int_{\gamma_{\min}}^{\gamma_{\max}} N(\gamma)\, d\gamma\,,$$

where $\gamma_{\min}$ and $\gamma_{\max}$ are respectively the minimum and maximum adimensional energy of the particle distribution.

On the other hand, photon emission from a source can be described by the differential luminosity

$$L_\nu = \frac{dE}{dt\, d\nu} \left[\mathrm{erg\ s^{-1}\ Hz^{-1}}\right],$$

where ν is the photon frequency, so that $L_\nu\, d\nu$ is the power emitted between frequencies ν and $\nu + d\nu$. An observer away from the source will measure a differential energy flux (or energy spectrum)

$$F_\nu = \frac{dE}{dA\, dt\, d\nu} \left[\mathrm{erg\ cm^{-2}\ s^{-1}\ Hz^{-1}}\right],$$

expressing the energy crossing a unit surface per unit time and unit frequency. If the emission from the source is isotropic the flux measured at a luminosity distance D will of course be

$$F_\nu = \frac{L_\nu}{4\pi D^2}\,. \tag{A.2}$$

We also introduce the photon spectrum

$$\phi_\nu = \frac{d\mathcal{N}}{dA\, dt\, d\nu} \left[\mathrm{\ cm^{-2}\ s^{-1}\ Hz^{-1}}\right],$$

expressing the number of photons crossing a unit surface per unit time and unit frequency; of course we have $\phi_\nu = F_\nu/h\nu$.

Besides differential quantities, we can use bolometric luminosity and flux

$$L = \int_{\nu_{\min}}^{\nu_{\max}} L_\nu\, d\nu \quad \left[\mathrm{erg\ s^{-1}}\right],$$

$$F = \int_{\nu_{\min}}^{\nu_{\max}} F_\nu\, d\nu \quad \left[\mathrm{erg\ cm^{-2}\ s^{-1}}\right],$$

expressing total luminosity and flux (respectively) between $\nu_{\min}$ and $\nu_{\max}$.

Another useful radiation representation is the spectral energy distribution (SED), that is,

$$S_\nu = \nu F_\nu \,; \tag{A.3}$$

even being a differential quantity, it has an approximate meaning of integrated flux. In fact, if the flux is described by a power-law, that is, $F_\nu = K\nu^{-a}$, bolometric flux will be $F = K/(1-a)\nu^{1-a} \propto S_\nu$.

To characterize the radiation distribution inside a source of volume V, it is useful to introduce the emissivity

$$j_\nu(r,\Omega) = \frac{dE}{dV\,dt\,d\nu}\,\left[\text{erg cm}^{-3}\ \text{s}^{-1}\ \text{Hz}^{-1}\right],$$

which can be related to the differential luminosity; let us consider, for example a spherical source with radius R containing particles with homogeneous density; if the radiation is homogeneously and isotropically distributed inside the source, that is, j_ν does not depends on r and Ω, we have (Band & Grindlay, 1985)

$$L_\nu = \pi R^3 \frac{j_\nu}{\tau_\nu}\left[1 - \frac{1 - e^{-2\tau_\nu}\,(1+2\tau_\nu)}{2\tau_\nu^2}\right],$$

where τ_ν is the optical depth for particle-photon interaction; for an optically thin source, that is $\tau_\nu \ll 1$ one obtains

$$L_\nu = \frac{4}{3}\pi R^3 j_\nu \,. \tag{A.4}$$

Lastly, we introduce the photon differential frequency distribution

$$N_\nu = \frac{d\mathcal{N}}{dV\,d\nu}\,\left[\text{cm}^{-3}\ \text{Hz}^{-1}\right], \tag{A.5}$$

where $\mathcal{N}$ is the total number of photons and, so that $N(\nu)\,d\nu$ is the number of photons per unity of volume with frequency between ν and $\nu + d\nu$. N_ν can be related to the emissivity; for example, for an optically thin, spherical source with radius R one has (Gould, 1979)

$$N_\nu(r) = \frac{1}{h\nu c}\int_0^R \frac{j_\nu\,(r',\Omega')}{4\pi\left|\vec{r}-\vec{r'}\right|^2}\,d\Omega' \,;$$

for an homogeneous, isotropic radiation we have

$$N_\nu(r) = \frac{R}{4c}\frac{j_\nu}{h\nu}\left[\left(\frac{1-x^2}{x}\right)\ln\left(\frac{1+x}{1-x}\right) + 2\right],$$

where $x = r/R$. It is possible to simplify calculations considering a mean photon density, that is

$$\bar{N}_\nu = \frac{\displaystyle\int N_\nu(r)\,dV}{\displaystyle\frac{4}{3}\pi R^3} = \frac{3}{4}\frac{R}{c}\frac{j_\nu}{h\nu}\,, \tag{A.6}$$

which corresponding to an effective radius $r \approx 0.8R$.

A.2 Synchrotron radiation

A.2.1 Power emitted by a single electron

The motion of an electron with speed $\vec{v}$ in an electromagnetic field is described by the equation (Rybicki & Lightman, 1979; Vietri, 2006; Jackson, 2001)

$$\frac{dp^\mu}{d\tau} = \frac{e}{c}\,F^{\mu\nu}u_\nu \,, \tag{A.7}$$

where m and e are the electron rest mass and charge, respectively, $u^\mu = \gamma\,(c, \vec{v})$ is the quadri-velocity, $p^\mu = mu^\mu$ is the quadri-momentum, $d\tau = \sqrt{dt^2 - dx^2/c^2}$, and $F^{\mu\nu}$ is the electromagnetic tensor

$$F^{0i} = -E_i, \qquad F^{ij} = -\epsilon_{ijk} B_k\,,$$

being $\vec{E}$ and $\vec{B}$ the electric and magnetic field, respectively, and ϵ_{ijk} the Levi-Civita tensor. If $\vec{E} = 0$, the temporal part of Eq. A.7 yields $d\gamma/dt = 0$, so the spatial part of Eq. A.7 become

$$\gamma m \frac{d\vec{v}}{dt} = \frac{e}{c}\,\vec{v} \wedge \vec{B}\,. \tag{A.8}$$

Let now be $\vec{B}$ = const; scalar-multiplying Eq. A.8 by $\vec{B}$ one obtains

$$a_{\shortparallel} = \frac{dv_{\shortparallel}}{dt} = 0\,, \tag{A.9}$$

$$\vec{a}_\perp = \frac{d\vec{v}_\perp}{dt} = \frac{e}{\gamma mc}\,\vec{v}_\perp \wedge \vec{B}\,. \tag{A.10}$$

Scalar-multiplying Eq. A.10 by $\vec{v}_\perp$ gives $v_\perp$ = const, which together with Eq. A.9 yields v = const. So, while the motion component parallel to the magnetic field is a linear uniform, on a plane normal to $\vec{B}$ the electron describes a circular uniform motion with frequency ν_g/γ, where

$$\nu_g = \frac{eB}{2\pi mc} \approx 2.7993 \times 10^6 \left(\frac{B}{1\ \mathrm{G}}\right)\ \mathrm{Hz}$$

is the Larmor frequency; the resulting electron motion will therefore be represented by a spiral along the magnetic field direction.

In order to calculate the power emitted by the electron we make use of the Larmor equation

$$P = -\frac{2e^2}{3c^3}\,a^\mu a_\mu\,;$$

from Eq. A.9 we have $a_{\shortparallel} = 0$, and from Eq. A.10 we have $\vec{v}_\perp \perp \vec{a}_\perp$, so

$$a^\mu a_\mu = -c^2\gamma^4 \left[\gamma^2 \left(\vec{\beta}\dot{\vec{\beta}}\right)^2 + \left(\dot{\vec{\beta}}\right)^2\right] = -\gamma^4 \left(\dot{\vec{v}}\right)^2,$$

where $\vec{\beta} = \vec{v}/c$. We then have the emitted power by a single electron by synchrotron radiation

$$P_S = 2\sigma_T c \beta^2 \gamma^2 \varepsilon_B \sin^2\theta, \tag{A.11}$$

where $\sigma_T = \frac{8\pi e^4}{3m^2c^4}$ is the Thomson cross section, $\varepsilon_B = B^2/8\pi$ is the energy density of the magnetic field and θ is the angle between $\vec{v}$ and $\vec{B}$; we note that θ = const, because

$$\theta = \arccos\left(\frac{\vec{v}\vec{B}}{vB}\right) = \arccos\left(\frac{v_{\shortparallel}}{v}\right).$$

If electron velocities are isotropically distributed we can average P_S over θ, to obtain

$$P_S = 2\sigma_T c \beta^2 \gamma^2 \varepsilon_B \frac{1}{4\pi} \int d\Omega\, \sin^2\theta = \frac{4}{3}\sigma_T c \beta^2 \gamma^2 \varepsilon_B. \tag{A.12}$$

The synchrotron emitted power per frequency unit by an electron with energy γmc^2 is

$$\frac{dP_S}{d\nu} = \frac{\sqrt{3} e^3 B \sin\theta}{mc^2} F\left(\frac{\nu}{\nu_s}\right), \tag{A.13}$$

where

$$\nu_S = \frac{3}{2}\nu_g \gamma^2 \sin\theta \tag{A.14}$$

is the characteristic synchrotron frequency; the function F is defined by

$$F(x) = x \int_x^\infty K_{\frac{5}{3}}(z)\, dz\,,$$

where K is a modified second species Bessel function

$$K_n(z) = \frac{\Gamma\left(n+\frac{1}{2}\right)(2z)^n}{\sqrt{\pi}} \int_0^\infty \frac{\cos y}{(y^2+z^2)^{n+\frac{1}{2}}}\, dy\,.$$

The characteristic timescale on which the electron with energy γmc^2 looses energy by synchrotron radiation, or synchrotron cooling time, is

$$t_S = \frac{\gamma mc^2}{P_S} \approx 0.7738 \times 10^9 \frac{1}{\gamma}\left(\frac{B}{1\mathrm{G}}\right)^{-2} \mathrm{s}\,. \tag{A.15}$$

A.2.2 Emitted spectra form an electron population

The emissivity for an electron population with an energy distribution $N(\gamma)$ is

$$j_\nu = \int N(\gamma)\, \frac{dP}{d\nu}\, d\gamma\,; \tag{A.16}$$

using Eq. A.13 we have for synchrotron radiation

$$j_{\nu S} = \frac{\sqrt{3} e^3 B \sin\theta}{mc^2} \int N(\gamma)\, F\left(\frac{\nu}{\nu_s(\gamma)}\right) d\gamma\,. \tag{A.17}$$

where F depends on γ by means of ν_s according to Eq. A.14; an approximated expression of function F at 3% level is given by

$$F(x) = x^{\frac{1}{3}} \frac{2.79x + 2.13}{2.15x^{\frac{5}{6}}\mathrm{e}^x + 0.5x + 0.96}\,,$$

as shown in Fig. A.1. Function F has the following asymptotic trends

$$F(x) = \begin{cases} 2.15x^{\frac{1}{3}} & x \ll 1 \\ \sqrt{\frac{\pi}{2}} x^{\frac{1}{2}} \mathrm{e}^{-x} & x \gg 1 \end{cases},$$

and features a sharp peak at $x \approx 0.29$, so, to a fair approximation, we can adopt a delta approximation

$$\frac{dP}{d\nu} \approx P_S\, \delta\left(\nu - 0.29\,\nu_s\right) \approx P_S\, \delta\left(\nu - \gamma^2 \nu_c\right), \tag{A.18}$$

where $\nu_c = 0.29\,(3/2)\,\nu_g \sin\theta$, and P_S is given by Eq. A.11. Then, on using Eqs. A.2, A.4, A.16 and A.18, we can write for the synchrotron energy spectrum observed at a luminosity distance D from a spherical source with radius R

$$F_{\nu S} \approx \frac{1}{18\,0.29} \frac{\sigma_T mc^2 \beta^2}{e} \frac{R^3\, B \sin\theta}{D^2}\, \sqrt{\frac{\nu}{\nu_c}}\, N\left(\sqrt{\frac{\nu}{\nu_c}}\right). \tag{A.19}$$

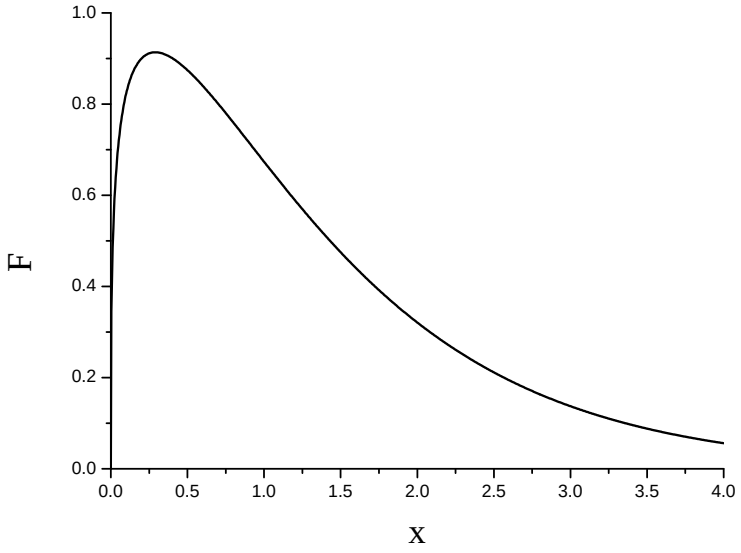

Figure A.1: Function F describing synchrotron emission (see Eq. A.13).

A.3 Compton scattering

We now consider the scattering of a non polarized electromagnetic wave with frequency ν'_0 on an electron at rest with mass m and electric charge e; if the incoming photon has energy $h\nu'_0 \ll mc^2$, we can neglect energy exchanges between photon and electron and consider an elastic scattering; this is the classical Thomson scattering, characterized by a differential cross section (Rybicki & Lightman, 1979)

$$\frac{d\sigma_T}{d\Omega} = \frac{{r_0}^2}{2}\left(1 + \cos^2\theta'\right), \tag{A.20}$$

where $r_0 = e^2/mc^2$ is the classical electron radius and θ' is the scattering angle, that is, the angle between the directions of the incoming and the scattered photon; the total cross section of the Thomson scattering is

$$\sigma_T = \frac{8\pi}{3}{r_0}^2. \tag{A.21}$$

We now do not neglect energy exchanges between photon and electron; we denote with P'_0 and P' the photon momentum before and after the scattering, respectively:

$$P'^{\mu}_0 = \left(\frac{h\nu'_0}{c}, \vec{P}'_0\right),$$
$$P'^{\mu} = \left(\frac{h\nu'}{c}, \vec{P}'\right),$$

where $\left|\vec{P}'_0\right| = h\nu'_0/c$ and $\left|\vec{P}'\right| = h\nu'/c$; on the other hand the electron momentum is

$$p'^{\mu}_0 = \left(mc, \vec{0}\right),$$
$$p'^{\mu} = \left(mc\gamma', \vec{p'}\right),$$

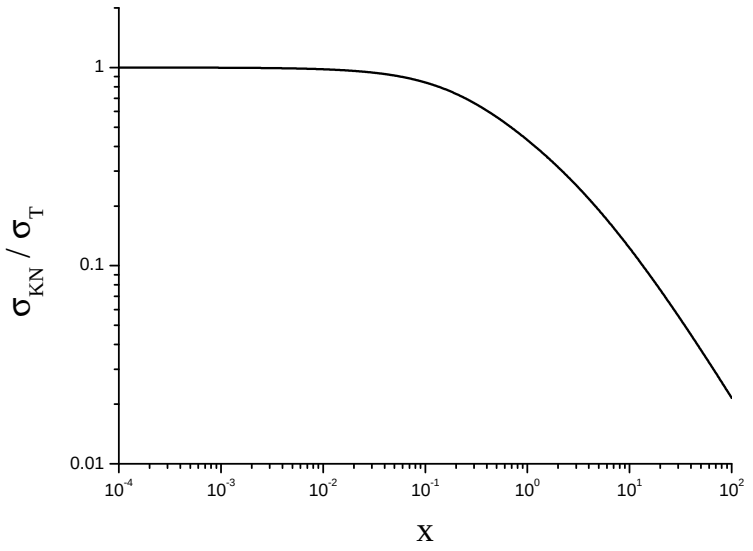

Figure A.2: Klein-Nishina cross section as a function of $x = h\nu'_0/mc^2$ (see Eq. A.24).

before and after the scattering, respectively. Momentum conservation yields

$$h\nu' = \frac{h\nu'_0}{1 + \dfrac{h\nu'_0}{mc^2}\,(1 - \cos\theta')}\,; \tag{A.22}$$

The process is characterized by the differential Klein-Nishina cross section

$$\frac{d\sigma_{KN}}{d\Omega} = \frac{{r_0}^2}{2}\left(\frac{\nu'}{\nu'_0}\right)^2\left[\left(\frac{\nu'_0}{\nu'}\right)^2 + \left(\frac{\nu'}{\nu'_0}\right)^2 - \sin^2\theta'\right]; \tag{A.23}$$

note that for $h\nu'_0/mc^2 \ll 1$ we recover the classical Thomson scattering, because Eq. A.22 gives $h\nu' \approx h\nu'_0$ and so Eq. A.23 reduces to Eq. A.20. The total Klein-Nishina cross section is given by

$$\sigma_{KN} = \sigma_T \frac{3}{4}\left\{\frac{1+x}{x^3}\left[\frac{2x(1+x)}{1+2x} - \ln(1+2x)\right] + \frac{1}{2x}\ln(1+2x) - \frac{1+3x}{(1+2x)^2}\right\}, \tag{A.24}$$

where the parameter $x = h\nu'_0/mc^2$ regulates the transition between the non relativistic Thomson regime ($x \ll 1$) and the ultra relativistic Klein-Nishina regime ($x \gg 1$), as shown in Fig. A.2. In the two regimes, Eq. A.24 features the following asymptotic trends

$$\sigma_{KN} = \begin{cases} \sigma_T\left[1 - 2x + \dfrac{26}{5}x^2 + \cdots\right] & x \ll 1 \\ \sigma_T\,\dfrac{3}{8}\,\dfrac{1}{x}\left[\ln(2x) + \dfrac{1}{2}\right] & x \gg 1 \end{cases}. \tag{A.25}$$

A.4 Inverse Compton scattering

We now consider a situation where the electron is not at rest but has a velocity $\vec{\beta} = \vec{v}/c$ forming an angle α with the direction $\widehat{k_0}$ of the incoming photon (inverse Compton scattering, IC); we denote with ν_0 and

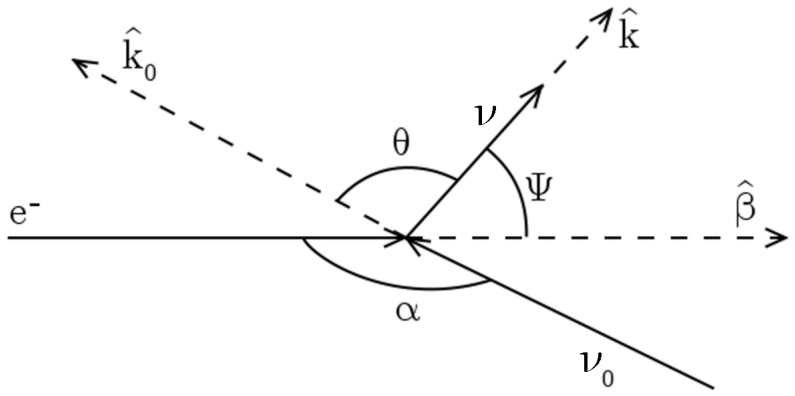

Figure A.3: Schematic description of IC scattering.

ν the photon frequency before and after the scattering, respectively; we choose a reference frame with z axis along $\widehat{k_0}$ and $\widehat{\beta} = \vec{\beta}/\beta$ lying on the xz plane (see Fig. A.3). We have

$$\widehat{\beta} = (\sin\alpha, 0, \cos\alpha) \ ,$$

while the scattered photon direction will be

$$\widehat{k} = (\sin\theta\cos\phi, \sin\theta\sin\phi, \cos\theta) \ .$$

We also denote with Ψ the angle between $\widehat{\beta}$ and $\widehat{k}$; we have of course $\alpha = \Psi + \theta$.

Now we move to the electron rest frame, where the electron has energy mc^2 before the scattering; in this reference frame angles and frequencies are denoted with a prime mark. So, ν'_0 and ν' are the photon frequencies before and after the scattering, respectively, and for example we will have (Longair, 1997)

$$\cos\alpha' = \frac{\cos\alpha - \beta}{1 - \beta\cos\alpha} \ . \tag{A.26}$$

In this rest frame we can apply the results of the previous section, in particular Eq. A.22

$$h\nu' = \frac{h\nu'_0}{1 + \dfrac{h\nu'_0}{mc^2}\,(1 - \cos\theta')} \ .$$

Using Lorentz transformations

$$h\nu'_0 = \gamma h\nu_0\,(1 - \beta\cos\alpha) \ , \tag{A.27}$$

$$h\nu = \gamma h\nu'\,(1 + \beta\cos\Psi') \tag{A.28}$$

in Eq. A.22, we obtain

$$h\nu = \gamma^2 h\nu_0 \frac{(1 - \beta\cos\alpha)\,(1 + \beta\cos\Psi')}{1 + \dfrac{\gamma h\nu_0}{mc^2}\,(1 - \beta\cos\alpha)\,(1 - \cos\theta')} \ . \tag{A.29}$$

Using the head-on scattering approximation $\alpha' \approx \pi$ we have from Eq. A.26 $\alpha \approx \pi$; so, because $\alpha' = \Psi' + \theta'$, we have $\cos\Psi' = -\cos\theta'$. Substituting into Eq. A.29 we have

$$h\nu \approx \gamma^2 h\nu_0 \frac{(1+\beta)(1-\beta\cos\theta')}{1+\frac{\gamma h\nu_0}{mc^2}(1+\beta)(1-\cos\theta')}\,. \tag{A.30}$$

We can now consider the two limit conditions $\theta' \approx 0$ and $\theta' \approx \pi$; in the former situation photon does not exchange energy with the electron because from Eq. A.30 we have $\nu = \nu_0$. In the latter photon is back scattered, exchanging the maximum energy, that is,

$$h\nu_{\max} = \gamma^2 h\nu_0 \frac{(1+\beta)^2}{1+\frac{2\gamma h\nu_0}{mc^2}(1+\beta)}\,,$$

which in ultra relativistic limit $\beta \approx 1$ becomes

$$h\nu_{\max} \approx \frac{4\gamma^2 h\nu_0}{1+\frac{4\gamma h\nu_0}{mc^2}}\,; \tag{A.31}$$

in conclusion, we have

$$h\nu_0 \leqslant h\nu \leqslant \frac{4\gamma^2 h\nu_0}{1+\frac{4\gamma h\nu_0}{mc^2}}\,. \tag{A.32}$$

For $\beta \approx 1$, $\alpha \approx \pi$ Eq. A.27 yields $h\nu'_0 \approx 2\gamma h\nu_0$, so Eq. A.31 can be rewritten as

$$h\nu_{\max} \approx \frac{4\gamma^2 h\nu_0}{1+2\frac{h\nu'_0}{mc^2}}\,;$$

in particular in Thomson regime, that is, $h\nu'_0 = 2\gamma h\nu_0 \ll mc^2$, the maximum frequency of the scattered photon is

$$h\nu_{\max} \approx 4\gamma^2 h\nu_0\,, \tag{A.33}$$

while in the Klein Nishina regime, that is, $h\nu'_0 = 2\gamma h\nu_0 \gg mc^2$, we have

$$h\nu_{\max} \approx \gamma mc^2 \tag{A.34}$$

with the electron transferring all his energy to the photon.

A.4.1 Power radiated by a single electron

We can now calculate the power radiated by a single electron via IC scattering: if the photons have a differential frequency distribution

$$N_{\nu_0} = \frac{d\mathcal{N}_{\nu_0}}{dV\,d\nu_0}\,,$$

in the electron rest frame we can write for the radiated power in the Thomson regime

$$P'_{\rm rad} = c\sigma_T h \int \nu'\, N_{\nu'_0}\, d\nu'_0 = P_{\rm rad}\,,$$

being the emitted power a Lorentz invariant. In the Thomson regime we have $\nu' \approx \nu'_0$, so

$$P_{\rm rad} = c\sigma_T h \int \nu'_0\, N_{\nu'_0}\, d\nu'_0 = c\sigma_T h \int {\nu'}_0^2\, \frac{N_{\nu'_0}}{\nu'_0}\, d\nu'_0\,,$$

and because $N_\nu/\nu\, d\nu$ is invariant, we have

$$P_{\rm rad} = c\sigma_T h \int {\nu'}_0^2 \frac{N_{\nu_0}}{\nu_0}\, d\nu_0 \,.$$

Using Eq. A.27 we have

$$P_{\rm rad} = c\sigma_T \gamma^2 h \int (1-\beta\cos\alpha)^2\, \nu_0\, N_{\nu_0}\, d\nu_0 \,;$$

for an isotropically distributed radiation we have

$$\left\langle (1-\beta\cos\alpha)^2 \right\rangle = 1 + \frac{1}{3}\beta^2 \,,$$

and so

$$P_{\rm rad} = c\sigma_T \gamma^2 h \left(1 + \frac{1}{3}\beta^2\right) \int \nu_0\, N_{\nu_0}\, d\nu_0 \,.$$

On the other hand, the power of the incoming radiation is

$$P_{\rm in} = c\sigma_T h \int \nu_0\, N_{\nu_0}\, d\nu_0 \,,$$

and denoting the energy density of the incoming radiation with

$$\varepsilon_\nu = h \int \nu_0\, N_{\nu_0}\, d\nu_0 \,,$$

we can write

$$P_{\rm rad} = c\sigma_T \gamma^2 \left(1 + \frac{1}{3}\beta^2\right) \varepsilon_\nu \,,$$
$$P_{\rm in} = c\sigma_T \varepsilon_\nu \,.$$

So the net emitted power will be

$$P_C = P_{\rm rad} - P_{\rm in} = \frac{4}{3}\,\sigma_T\,\gamma^2\,\beta^2\,c\,\varepsilon_\nu \,. \tag{A.35}$$

The characteristic timescale on which the electron with energy γmc^2 looses energy by IC emission, or IC cooling time, is

$$t_S = \frac{\gamma mc^2}{P_C}. \tag{A.36}$$

A.4.2 Emitted spectra form an electron population

We denote with ν_0 the incoming photon frequency, with $\gamma = E/mc^2$ the electron adimensional energy, and with ν the emitted photon frequency; if incoming photons have a differential frequency distribution N_{ν_0} the number of IC radiated photons per time unit, incoming frequency unit and scattered frequency unit is

$$\frac{d\mathcal{N}_\nu}{dt\, d\nu\, d\nu_0} = N_{\nu_0}\, K(\nu, \nu_0, \gamma) \,, \tag{A.37}$$

where $K(\nu, \nu_0, \gamma)$ is the Compton kernel (Jones, 1968)

$$K(\nu, \nu_0, \gamma) = \frac{2\pi {r_0}^2 c}{\gamma^2 \nu_0} \left[2q\ln q + (1+2q)(1-q) + 2\frac{(xq)^2}{(1+2xq)}(1-q) \right] , \tag{A.38}$$

having denoted $x = 2\gamma h\nu_0/mc^2$ and

$$q = \frac{\nu}{4\nu_0\gamma^2\left(1 - \frac{h\nu}{\gamma mc^2}\right)} .$$

From Eq. A.32 we obtain

$$\frac{1}{4\gamma^2\left(1 - \frac{h\nu_0}{\gamma mc^2}\right)} \leqslant q \leqslant 1 .$$

In general, radiated power per unit frequency by a single electron will therefore be

$$\frac{dP}{d\nu} = h \int \nu N_{\nu_0} K(\nu, \nu_0, \gamma)\, \nu_0 ,$$

so, if the electrons have an energy distribution $N(\gamma)$ the emissivity will be (Inoue & Takahara, 1996)

$$j_{\nu IC} = \int N(\gamma) \frac{dP}{d\nu} d\gamma = h \int d\gamma\, N(\gamma) \int \nu N_{\nu_0} K(\nu, \nu_0, \gamma)\, d\nu_0 ;$$

for an optically thins, spherical source with radius R, we can write

$$F_{\nu IC} = \frac{1}{3}\frac{R^3}{D^2} h \int d\gamma\, N(\gamma) \int \nu N_{\nu_0} K(\nu, \nu_0, \gamma)\, d\nu_0 .$$

Let's now look in more detail Eq. A.38; neglecting the constant term we focus on

$$F(q; x) = \left[2q \ln q + (1 + 2q)(1 - q) + 2\frac{(xq)^2}{(1 + 2xq)}(1 - q)\right] . \tag{A.39}$$

Looking at Eq. A.31 we introduce the quantity (Blumenthal & Gould, 1970)

$$\widehat{E} = \frac{h\nu}{h\nu_{\max}} = \frac{h\nu}{4\gamma^2 h\nu_0}\left(1 + \frac{4\gamma h\nu_0}{mc^2}\right) = \frac{(1 + 2x)q}{1 + 2qx} . \tag{A.40}$$

Function F is shown in Fig. A.4; while for x small values (Thomson regime) most photons are scattered with small outgoing energies, at bigger x values (Klein-Nishina regime) the majority of photons is scattered with energies close to $h\nu_{\max}$.

We can obtain the limit values of A.38 in Thomson and Klein-Nishina regimes. In Thomson regime, that is $x \ll 1$, we have from Eq. A.40 $q \approx \widehat{E}$; moreover in Eq. A.38 the last term become negligible, so

$$K(\nu, \nu_0, \gamma) \approx \frac{2\pi {r_0}^2 c}{\gamma^2 \nu_0}\left[2\widehat{E} \ln \widehat{E} + \widehat{E} - 2\widehat{E}^2 + 1\right] .$$

In Klein-Nishina regime, on the other hand, we have $x \gg 1$, and for $\widehat{E} \neq 1$ we obtain from Eq. A.40

$$xq \approx \frac{\widehat{E}}{2\left(1 - \widehat{E}\right)} ,$$

and so $q \ll 1$. We then have

$$K(\nu, \nu_0, \gamma) \approx \frac{2\pi {r_0}^2 c}{\gamma^2 \nu_0}\left[1 + \frac{\widehat{E}^2}{2(1 - \widehat{E})}\right] .$$

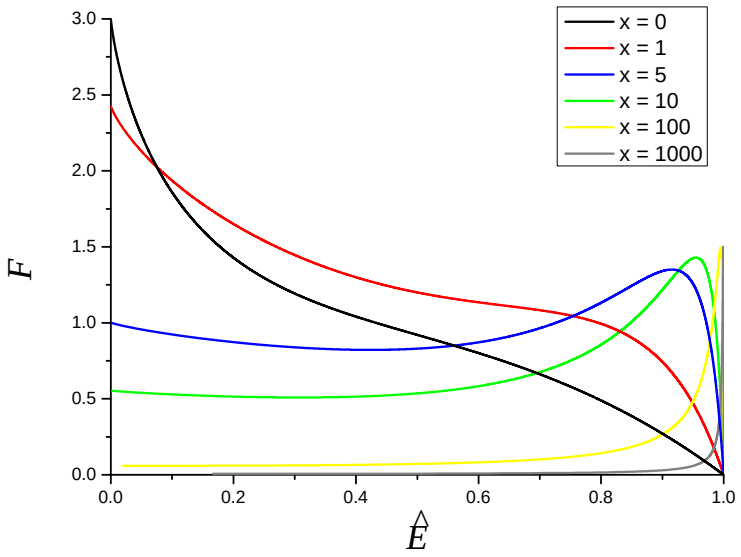

Figure A.4: Normalized $F(q;x)$ as a function of $\widehat{E}$ for different values of $x = 2\gamma h\nu_0/mc^2$ (see Eq. A.39).

For $\widehat{E} \approx 1$ we obtain form Eq. A.40 $xq \gg 1$; on neglecting the term $1-q$ in Eq. A.38 we have

$$K(\nu,\nu_0,\gamma) \approx \frac{4\pi {r_0}^2 c}{\gamma^2 mc^2} \frac{\frac{h\nu}{mc^2}}{\frac{2\gamma\nu_0}{mc^2}} \frac{1}{\left(1-\frac{h\nu}{\gamma mc^2}\right)} . \tag{A.41}$$

Note that for $\widehat{E} \neq 1$ Eq. A.41 become very small, being the denominator proportional to $x \gg 1$, while for $\widehat{E} \approx 1$ we have

$$K(\nu,\nu_0,\gamma) \approx \frac{2\pi {r_0}^2 c}{\gamma^2} \frac{1}{\nu_0\left(1-\frac{h\nu}{\gamma mc^2}\right)} \gg 1 .$$

We can in conclusion write

$$K(\nu,\nu_0,\gamma) \propto \frac{1}{\gamma^2}\,\delta\left(1-\frac{h\nu}{\gamma mc^2}\right) . \tag{A.42}$$

A.4.3 Synchrotron-self Compton

With synchrotron-self Compton process (SSC) we indicate inverse Compton scattering by an electron population on synchrotron photons emitted by the same electron population (Huges, 1991). An electron population with an energy distribution $N(\gamma)$, in a spherical source with radius R with a magnetic field B will emit synchrotron radiation with emissivity given by Eq. A.17

$$j_{\nu_0 S} = \frac{\sqrt{3}e^3 B\sin\theta}{mc^2} \int N(\gamma)\, F\left(\frac{\nu_0}{\nu_s(\gamma)}\right) d\gamma .$$

According to Eq. A.6 we can consider an average synchrotron photon density

$$\bar{N}_{\nu_0 S} = \frac{3}{4}\frac{R}{c}\frac{j_{\nu_0 S}}{h\nu_0} .$$

On neglecting synchrotron radiative cooling energy losses, electrons will IC scatter those synchrotron photons; using the results of previous section we can write for IC radiation emissivity

$$\begin{aligned} j_{\nu C} &= h \int d\gamma\, N(\gamma) \int d\nu_0\, \nu\, \bar{N}_{\nu_0 S}\, K(\nu, \nu_0, \gamma) = \\ &= \frac{3}{4}\frac{R}{c} \int d\gamma\, N(\gamma) \int d\nu_0\, \frac{\nu}{\nu_0}\, j_{\nu_0 S} K(\nu, \nu_0, \gamma) = \\ &= \frac{3}{4}\frac{R}{c}\frac{\sqrt{3}\, e^3\, B\, \sin\theta}{m\, c^3} \int d\gamma\, N(\gamma) \int d\nu_0\, \frac{\nu}{\nu_0} \int d\,\gamma'\, N(\gamma')\, F\left(\frac{\nu_0}{\nu_s(\gamma')}\right) K(\nu, \nu_0, \gamma)\,. \end{aligned} \tag{A.43}$$

On neglecting IC radiative cooling energy losses, the electrons will IC scatter also IC radiation photons, whose average density is

$$\bar{N}_{\nu C} = \frac{3}{4}\,\frac{R}{c}\,\frac{j_{\nu C}}{h\nu}\,,$$

to obtain a second order IC radiation with emissivity

$$\begin{aligned} j_{\bar{\nu}\, 2C} &= h \int d\gamma\, N(\gamma) \int d\nu\, \bar{\nu}\, \bar{N}_{\nu C}\, K(\bar{\nu}, \nu, \gamma) = \\ &= \frac{3}{4}\frac{R}{c} \int d\gamma\, N(\gamma) \int d\nu\, \frac{\bar{\nu}}{\nu}\, j_{\nu C}\, K(\bar{\nu}, \nu, \gamma) = \\ &= \left(\frac{3}{4}\right)^2 \frac{R^2\, \sqrt{3}\, e^3\, B\, \sin\theta}{m\, c^4} \int d\gamma\, N(\gamma) \int d\nu \int d\gamma'\, N(\gamma') \cdot \\ &\cdot \int d\nu_0\, \frac{\bar{\nu}}{\nu_0} \int d\gamma''\, N(\gamma'')\, F\left(\frac{\nu_0}{\nu_s(\gamma'')}\right) K(\nu, \nu_0, \gamma')\, K(\bar{\nu}, \nu, \gamma)\,. \end{aligned} \tag{A.44}$$

A.5 Fermi acceleration

Fermi acceleration process (Fermi, 1954) describes electron scattering by moving, magnetized gas clouds; energy increase by electrons is possible because in cloud rest frame they are accelerated by an electric field.

A.5.1 Second order Fermi acceleration

We consider an electron with initial momentum $p_1^\mu = (E_1/c, \vec{p}_1)$, velocity $v \approx c$ and mass m colliding a magnetized gas cloud with mass M moving with a velocity V forming an angle θ_1 with v (see Fig.A.5); the particle will be scattered by the irregularities of cloud magnetic field (Protheroe, 1996, 1999).

We choose a reference frame with x axis along $\vec{V}$; in this frame electron momentum is

$$p'^{\mu}_1 = \left(\frac{E'_1}{c}, \vec{p'}_1\right),$$

and because $\left|\vec{p}_1\right| \approx E_1/c$, we have

$$\begin{aligned} \frac{E'_1}{c} &= \gamma\left(\frac{E_1}{c} - \beta\left|\vec{p}_1\right|\cos\theta_1\right) \approx \gamma\frac{E_1}{c}\left(1 - \beta\cos\theta_1\right)\,, \\ p'_{1\,x} &= \gamma\left(\left|\vec{p}_1\right|\cos\theta_1 - \beta\frac{E_1}{c}\right) \approx \gamma\frac{E_1}{c}\left(\cos\theta_1 - \beta\right)\,, \end{aligned}$$

where $\beta = V/c$ and $\gamma = 1/\sqrt{1-\beta^2}$. After crossing the cloud the electron will come out with momentum $p'^{\mu}_2 = \left(E'_2/c, \vec{p'}_2\right)$ and the velocity forming an angle θ'_2 with x axis; Lorentz transforming back in laboratory frame we have

$$p_2^\mu = \left(\frac{E_2}{c}, \vec{p}_2\right),$$

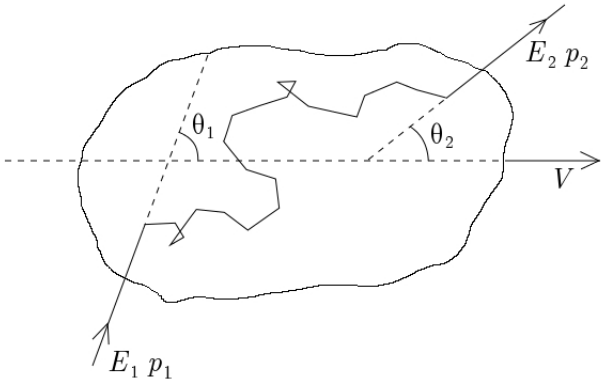

Figure A.5: Schematic representation of Fermi acceleration process.

that, being $\left|\vec{p'}_2\right| \approx E'_2/c$, yields

$$\frac{E_2}{c} = \gamma\left(\frac{E'_2}{c} + \beta\left|\vec{p'}_2\right|\cos\theta'_2\right) \approx \gamma\frac{E'_2}{c}\left(1+\beta\cos\theta'_2\right) .$$

If $m \ll M$ we can consider the scattering as elastic, that is, $E'_1 = E'_2$; we have then

$$E_2 \approx \gamma E'_1\left(1+\beta\cos\theta'_2\right) \approx \gamma^2 E_1\left(1-\beta\cos\theta_1\right)\left(1+\beta\cos\theta'_2\right)$$

The relative energy variation will therefore be

$$\frac{\Delta E}{E} = \frac{E_2 - E_1}{E_1} \approx \gamma^2\left(1-\beta\cos\theta_1+\beta\cos\theta'_2-\beta^2\cos\theta_1\cos\theta'_2\right) - 1 .$$

For typical values ($V \simeq 15$ Km s^{-1}) we have $\beta \ll 1$ and we can write

$$\frac{\Delta E}{E} \approx \beta^2\left(1-\cos\theta_1\cos\theta'_2\right) - \beta\cos\theta_1 + \beta\cos\theta'_2 . \tag{A.45}$$

From Eq. A.45 we see that head on collisions, that is, collisions with $\theta_1 \approx \pi$, yield energy increases, while tail on collisions with $\theta_1 \approx 0$ yield energy decreases; the probability of a collision at θ_1 is proportional to the relative velocity between electron and cloud, that is,

$$\frac{dP}{d\Omega_1} \propto v - V\cos\theta_1 .$$

Being $v \approx c$ we can write

$$\frac{dP}{d\Omega_1} \propto 1 - \beta\cos\theta_1 ,$$

showing that head on collision are slightly more probable than tail on collisions; the average value of $\cos\theta_1$ is

$$\langle\cos\theta_1\rangle = \frac{\int d\Omega_1 \frac{dP}{d\Omega_1}\cos\theta_1}{\int d\Omega_1 \frac{dP}{d\Omega_1}} = -\frac{\beta}{3} ;$$

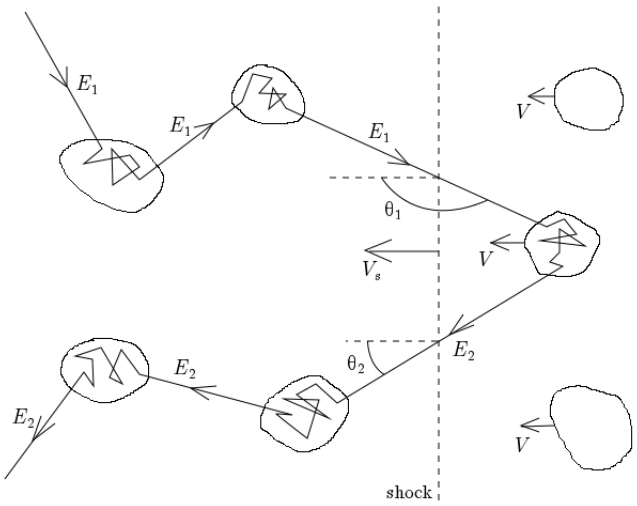

Figure A.6: Schematic representation of shock-particle interaction.

On the other hand, the electron can come out the cloud with any angle, so $\langle \cos\theta'_2 \rangle = 0$, yielding

$$\left\langle \frac{\Delta E}{E} \right\rangle \approx \frac{4}{3}\beta^2 \,. \tag{A.46}$$

This process, however, is poorly efficient in accelerating electrons, because head on collisions (yielding energy increase) are only slightly more probable than tail on collisions (yielding energy decrease); as a consequence the average energy increase is proportional to $\beta^2 \ll 1$. Acceleration efficiency can be increased in presence of shock front, as discussed in the next section.

A.5.2 First order Fermi acceleration

We now consider a shock front moving with velocity V_s in a medium with gas clouds; clouds upstream the shock front are at rest, while those downstream move with velocity V parallel to V_s (see Fig. A.6).

We now consider an electron upstream crossing the shock front and colliding shocked gas cloud; we can apply to this process the results of the previous section, in particular Eq. A.45. However, for a upstream electron to actually cross the shock front it must be $\cos\theta_1 \leqslant 0$. If n if is the electron density upstream, on considering $V_s \ll c$ the shock-crossing rate for upstream electrons is

$$R_{\rm cross} = \frac{n}{4\pi} \int\limits_{\cos\theta_1 \leqslant 0} (V_s - c\cos\theta_1)\, d\Omega_1 \approx n\,\frac{c}{4}\,,$$

so the probability for an electron to have a velocity forming an angle θ_1 with V_s

$$\frac{dP}{d\Omega_1} \propto \frac{n\,c\,\cos\theta_1}{R_{\rm cross}} \propto \cos\theta_1 \,.$$

The average value of $\cos\theta_1$ will therefore be

$$\langle \cos\theta_1 \rangle = \frac{\displaystyle\int\limits_{\cos\theta_1 \leqslant 0} d\Omega_1 \frac{dP}{d\Omega_1} \cos\theta_1}{\displaystyle\int\limits_{\cos\theta_1 \leqslant 0} d\Omega_1 \frac{dP}{d\Omega_1}} = -\frac{2}{3}\,.$$

In the same way, for the electron to cross the shock front again after the scattering with the downstream cloud it has to be

$$\langle \cos \theta'_2 \rangle = \frac{2}{3} .$$

We can therefore average Eq. A.45 over the angles distribution and neglect β^2 terms, to obtain

$$\left\langle \frac{\Delta E}{E} \right\rangle \approx \frac{4}{3} \beta . \tag{A.47}$$

In this case relative energy increase is proportional to β, making this mechanism more efficient in accelerating particles than the second order Fermi acceleration. In particular, for a strong shock on a monoatomic gas we have $V = 3/4\, V_s$, so that

$$\left\langle \frac{\Delta E}{E} \right\rangle \approx \frac{V_s}{c} . \tag{A.48}$$

This acceleration process yields to an electron energy distribution in the form of a power law, that is,

$$N(\gamma) = N_0 \left(\frac{\gamma}{\gamma_0} \right)^{-s} .$$

In fact, in the shock rest frame upstream clouds move with velocity $v_u = V_s$, while downstream clouds move with velocity $v_d = V_s - V$; for a strong shock on a monoatomic gas it will result $v_d = V_s/4$, and so the rate of electrons lost downstream is

$$R_{\text{loss}} = n v_d = n \frac{V_s}{4} .$$

Therefore the probability for an electron to cross the shock front and be lost downstream will be

$$P_{\text{esc}} = \frac{R_{\text{loss}}}{R_{\text{cross}}} \approx \frac{V_s}{c} ,$$

while the probability for an electron to cross the shock front and come back upstream is

$$P_{\text{ret}} = 1 - P_{\text{esc}} \approx 1 - \frac{V_s}{c} .$$

An electron, with initial energy E_0, after k acceleration cycles will reach energy

$$E = E_0 \left(1 + \frac{\Delta E}{E} \right)^k ,$$

where

$$k = \frac{\ln\left(\frac{E}{E_0}\right)}{\ln\left(1 + \frac{\Delta E}{E}\right)} .$$

So, the number of electrons that after k acceleration cycles will have energy greater than E will be

$$N(> E) \propto {P_{\text{ret}}}^k \approx \left(1 - \frac{V_s}{c} \right)^k = \left(\frac{E}{E_0} \right)^{\frac{\ln\left(1 - \frac{V_s}{c}\right)}{\ln\left(1 + \frac{\Delta E}{E}\right)}} .$$

Being $V_s/c \ll 1$, the exponent can be approximated as

$$\frac{\ln\left(1 - \frac{V_s}{c}\right)}{\ln\left(1 + \frac{\Delta E}{E}\right)} \approx \frac{\ln\left(1 - \frac{V_s}{c}\right)}{\ln\left(1 + \left\langle \frac{\Delta E}{E} \right\rangle\right)} \approx \frac{\ln\left(1 - \frac{V_s}{c}\right)}{\ln\left(1 + \frac{V_s}{c}\right)} \approx -1 ,$$

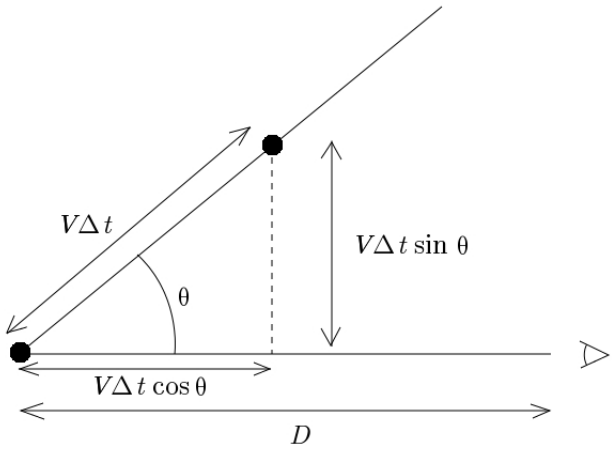

Figure A.7: Super-luminal motion scheme.

so

$$N(>E) \propto \left(\frac{E}{E_0}\right)^{-1},$$

and the differential energy distribution will of course be

$$N(\gamma) = \frac{dN(>\gamma)}{d\gamma} \propto \left(\frac{\gamma}{\gamma_0}\right)^{-2}. \tag{A.49}$$

A.6 Super-luminal motion and beaming effects

An emitting region moving with velocity V forming an angle θ with the observer line of sight can appear to move faster than light (Vietri, 2006); if the source is at distance D from the observer ad time t_0, emitted photons will reach us at time $t_0 + D/c$ (see Fig. A.7).

After a time $\Delta t \ll D/V$ the region moves of $V\Delta t$ and its distance from the observer will be approximatively $D - V\Delta t\cos\theta$, so emitted photons will now reach the observer at time $t_0 + \Delta t + (D - V\Delta t\cos\theta)/c$; however, the transverse shift as seen by the observer is $V\Delta t\sin\theta$, so the observer will estimate for the source an apparent velocity

$$v_{\rm app} = V\frac{\sin\theta}{1 - \frac{V}{c}\cos\theta}. \tag{A.50}$$

For $\cos\theta = V/c$ Eq. A.50 reaches its maximum ΓV, where $\Gamma = 1/\sqrt{1-(V/c)^2}$; so for angle values $\theta \approx \arccos V/c$ it is possible to have $v_{\rm app} > c$.

The source motion also modifies observed flues and frequencies, as a consequence of relativistic Doppler effect; in fact, if photons are emitted with frequency ν' in the region rest frame, they will be observed with frequency

$$\nu = \nu'\delta,$$

where δ is the beaming factor

$$\delta = \frac{1}{\Gamma\left(1 - \frac{V}{c}\cos\theta\right)}.$$

Note that for $\theta \ll 1$ we have $\delta \approx 2\Gamma$. Time interval will then transform as

$$\delta t = \delta t' \frac{1}{\delta} ,$$

while solid angles according to A.26 transform as

$$d\Omega = d\Omega' \frac{1}{\delta^2} ;$$

as a consequence, surfaces will transform as

$$dA = dA' \frac{1}{\delta^2} .$$

Emitted and observed fluxes will also be related by powers of the beaming factor; in fact, if the emitted flux in the source rest frame is

$$F'_{\nu'} = \frac{dE'}{dt'\, d\nu'\, dA'} ,$$

the number of emitted photons will be

$$dN' = \frac{1}{h\nu'} F'_{\nu'}\, dt'\, d\nu'\, dA' ,$$

and the observer will estimate a number of received photons

$$dN = \frac{1}{h\nu} F_\nu\, dt\, d\nu\, dA = \frac{1}{\delta^3} \frac{1}{h\nu'} F_\nu\, dt'\, d\nu'\, dA' .$$

Being the photon number invariant we have

$$\frac{1}{\delta^3} \frac{1}{h\nu'} F_\nu\, dt'\, d\nu'\, dA' = \frac{1}{h\nu'} F'_{\nu'}\, dt'\, d\nu'\, dA' ,$$

and so

$$F_\nu = \delta^3 F'_{\nu'} . \tag{A.51}$$

On the other hand, the SED

$$S'_{\nu'} = \nu' F'_{\nu'}$$

will transform as

$$S_\nu = \delta^4 S'_{\nu'} . \tag{A.52}$$

The rest frame bolometric luminosity inferred from assuming an isotropic flux distribution will transform as

$$L = L' \delta^4 . \tag{A.53}$$

Note that Eq. A.51 is valid for emission from a single spherical source; if emission is from a continuous jet we would have $F_\nu = \delta^2 F'_{\nu'}$ (Begelman et al., 1984; Lind & Blandford, 1985).

Of course, besides beaming effects, observed quantities will be affected by usual cosmological effects

$$\nu = \nu' \frac{1}{(1+z)} ,$$

$$S_\nu = S'_{\nu'} \frac{1}{(1+z)^2} ,$$

$$L = L' \frac{1}{(1+z)^2} .$$

Appendix B

Analytical solutions of diffusion equation

B.1 Fokker-Planck equation

Diffusion equation for a particle energy distribution in presence of systematic and stochastic acceleration processes can be written as

$$\frac{\partial N(\gamma,t)}{\partial t} = \lambda_2(t)\frac{\partial}{\partial\gamma}\left(\gamma^2\frac{\partial N}{\partial\gamma}\right) - \lambda_1(t)\frac{\partial}{\partial\gamma}\left(\gamma N\right) , \tag{B.1}$$

where λ_1 and λ_2 are the systematic and stochastic acceleration rates, respectively. Eq. B.1 can be solved analytically, on using methods proposed by Kaplan (1956). Given a function f, we introduce its Mellin transform

$$\widetilde{f}(p) = \int_0^\infty x^p f(x)\,dx\,,$$

$$f(x) = \frac{1}{2\pi i}\int_{\delta-i\infty}^{\delta+i\infty} x^{-p-1}\widetilde{f}\,(p)\;dp\,.$$

Multiplying Eq. B.1 by γ^p and integrating by parts in γ, we have, if N decreases to zero fast enough,

$$\frac{\partial\widetilde{N}(p,t)}{\partial t} = \left[p\lambda_1(t) + p(p+1)\lambda_2(t)\right]\widetilde{N}(p,t)\,,$$

so that

$$\widetilde{N}(p,t) = \widetilde{N}(p,0)\,\mathrm{e}^{p\Lambda_1+p(p+1)\Lambda_2}\,,$$

where

$$\Lambda_1(t) = \int^t \lambda_1(t')\,dt'\,,$$

$$\Lambda_2(t) = \int^t \lambda_2(t')\,dt'\,.$$

So we have

$$N(\gamma,t) = \frac{1}{2\pi i}\int_{\delta-i\infty}^{\delta+i\infty}\gamma^{-p-1}\widetilde{N}(p,0)\,\mathrm{e}^{p\Lambda_1+p(p+1)\Lambda_2}\,dp\,.$$

For an initially mono-energetic electron distribution

$$N(\gamma,0) = n\,\delta\left(\gamma-\gamma_0\right)\,,$$

we have

$$\widetilde{N}(p,0) = \int_0^\infty \gamma^p n\,\delta\left(\gamma-\gamma_0\right)\;d\gamma = n\,{\gamma_0}^p\,, \tag{B.2}$$

and therefore

$$N(\gamma,t) = \frac{1}{2\pi i}\frac{n}{\gamma}\int_{\delta-i\infty}^{\delta+i\infty}\left(\frac{\gamma}{\gamma_0}\right)^{-p} e^{p\Lambda_1+p(p+1)\Lambda_2}\,dp = \frac{1}{2\pi i}\frac{n}{\gamma}\int_{\delta-i\infty}^{\delta+i\infty} p\Lambda_1 + e^{p(p+1)\Lambda_2 - p\ln\left(\frac{\gamma}{\gamma_0}\right)}\,dp\,.$$

Denoting

$$\bar{p} = \frac{1}{2\Lambda_2}\left[\ln\left(\frac{\gamma}{\gamma_0}\right) - (\Lambda_1+\Lambda_2)\right] \tag{B.3}$$

we can write

$$N(\gamma,t) = \frac{1}{2\pi i}\frac{n}{\gamma}\mathrm{e}^{\Lambda_2\bar{p}^2-\left[\ln\left(\frac{\gamma}{\gamma_0}\right)-(\Lambda_1+\Lambda_2)\right]\bar{p}}\int_{\delta-i\infty}^{\delta+i\infty} e^{\Lambda_2(p-\bar{p})^2}\,dp.$$

Making a Lie rotation Lie $p' = -i(p-\bar{p})$ and substituting Eq. B.3 we have

$$N(\gamma,t) = \frac{1}{2\sqrt{\pi}}\frac{n}{\gamma_0}\frac{1}{\sqrt{\Lambda_2}}e^{-\frac{(\Lambda_1+\Lambda_2)^2}{4\Lambda_2}}\left(\frac{\gamma}{\gamma_0}\right)^{-\frac{1}{2}\left(1-\frac{\Lambda_1}{\Lambda_2}\right)-\frac{\ln 10}{4\Lambda_2}\log\left(\frac{\gamma}{\gamma_0}\right)}.$$

So we can write

$$N(\gamma,t) = N_0\left(\frac{\gamma}{\gamma_0}\right)^{-s-r\log\left(\frac{\gamma}{\gamma_0}\right)},$$

where

$$N_0 = \frac{1}{2\sqrt{\pi}}\frac{n}{\gamma_0}\frac{1}{\sqrt{\Lambda_2}}e^{-\frac{(\Lambda_1+\Lambda_2)^2}{4\Lambda_2}},$$
$$s = \frac{1}{2}\left(1-\frac{\Lambda_1}{\Lambda_2}\right),$$
$$r = \frac{\ln 10}{4\Lambda_2}.$$

Finally we note that the total power density of the electron distribution is

$$P = mc^2\frac{d}{d\,t}\int \gamma\,N(\gamma\,,t)\,d\gamma = mc^2 2\lambda_2\,n\,\gamma_0\left(1+\frac{\lambda_1}{2\lambda_2}\right)\mathrm{e}^{\Lambda_1+2\Lambda_2} = \left(1+\frac{\lambda_1}{2\lambda_2}\right)n\,\langle\gamma\rangle\,,$$

where $\langle\gamma\rangle$ is defined by Eq. 2.7.

B.2 Fokker-Planck equation with radiative cooling

In addition to systematic and stochastic acceleration, we now consider radiative cooling: if particle energy losses can be written as

$$\frac{d\gamma}{dt} = -\xi(t)\,\gamma^2\,,$$

diffusion equation is expressed by

$$\frac{\partial N(\gamma,\,t,)}{\partial t} = \lambda_2(t)\frac{\partial}{\partial\gamma}\left(\gamma^2\frac{\partial N}{\partial\gamma}\right) - \lambda_1(t)\frac{\partial}{\partial\gamma}(\gamma N) + \xi(t)\frac{\partial}{\partial\gamma}\left(\gamma^2 N\right). \tag{B.4}$$

Eq. B.4 can be solved for λ_1, λ_2 and ξ independent on time; as in previous section, we multiply Eq. B.4 by γ^p, integrate by parts in γ, to obtain

$$\frac{\partial\widetilde{N}(p,t)}{\partial t} = [p\lambda_1 + p(p+1)\lambda_2]\,\widetilde{N}(p,t) - p\,\xi\,\widetilde{N}(p+1,t)\,. \tag{B.5}$$

We now make use of Laplace transform

$$\widehat{f}(\omega) = \int_0^{+\infty} e^{-\omega t} f(t) dt \,,$$
$$f(t) = \frac{1}{2\pi i} \int_{\rho-i\infty}^{\rho+i\infty} e^{\omega t} \widehat{f}(\omega) d\omega \,;$$

we multiply Eq. B.5 by $e^{-\omega t}$ and integrate over time to obtain

$$\int_0^{+\infty} e^{-\omega t} \frac{\partial \widetilde{N}(p,t)}{\partial t} dt = [p\lambda_1 + p(p+1)\lambda_2]\, \widehat{N}(p,\omega) - p\xi \widehat{N}(p+1,\omega) \,, \tag{B.6}$$

where

$$\widehat{N}(p,\omega) = \int_0^{+\infty} e^{-\omega t} \widetilde{N}(p,t) dt \,.$$

Integrating by parts the left member of Eq. B.6 we obtain

$$-\widetilde{N}(p,0) + \omega\, \widehat{N}(p,\omega) = [p\lambda_1 + p(p+1)\lambda_2]\, \widehat{N}(p,\omega) - p\,\xi\, \widehat{N}(p+1,\omega) \,,$$

and therefore

$$\widehat{N}(p,\omega) = \frac{\widetilde{N}(p,0) - p\,\xi\, \widehat{N}(p+1,\omega)}{[\omega - \Phi(p)]} \,,$$

where

$$\Phi(p) = p\lambda_1 + p(p+1)\lambda_2 \,.$$

For an initially mono-energetic particle distribution we have from Eq. B.2 $\widetilde{N}(p,0) = n\,\gamma_0{}^p$, and so

$$\widehat{N}(p,\omega) = \frac{n\,\gamma_0{}^p - p\xi \widehat{N}(p+1,\omega)}{[\omega - \Phi(p)]} \,,$$
$$\widehat{N}(p+1,\omega) = \frac{n\,\gamma_0{}^{p+1} - (p+1)\xi \widehat{N}(p+2,\omega)}{[\omega - \Phi(p+1)]} \,,$$
$$\vdots$$
$$\widehat{N}(p+k,\omega) = \frac{n\,\gamma_0{}^{p+k} - (p+k)\xi \widehat{N}(p+k+1,\omega)}{[\omega - \Phi(p+k)]} \,.$$

On iteratively substituting we obtain

$$\widehat{N}(p,\omega) = n\,\gamma_0{}^p \sum_{k=0}^{\infty} \frac{(p+k-1)!}{(p-1)!} \frac{(-\gamma_0\xi)^k}{[\omega - \Phi(p)] \cdots [\omega - \Phi(p+k)]} \,, \tag{B.7}$$

which essentially is a power series of the parameter $q = \dfrac{\gamma_0 \xi}{2\lambda_2}$; if $q < 1$, we can consider only the first two terms of Eq. B.7

$$\widehat{N}(p,\omega) \approx n\,\gamma_0{}^p \left\{ \frac{1}{[\omega - \Phi(p)]} - \frac{\gamma_0 p \xi}{[\omega - \Phi(p)]\,[\omega - \Phi(p+1)]} \right\} .$$

On making inverse Laplace and Mellin transformations we have

$$N(\gamma,t) = -\frac{1}{4\pi^2}\int_{\delta-i\infty}^{\delta+i\infty}\gamma^{-(p+1)}dp\int_{\rho-i\infty}^{\rho+i\infty}e^{\omega t}\widehat{N}(p,\omega)d\omega \approx$$

$$\approx -\frac{n}{4\pi^2\gamma_0}\int_{\delta-i\infty}^{\delta+i\infty}\left(\frac{\gamma}{\gamma_0}\right)^{-(p+1)}dp\int_{\rho-i\infty}^{\rho+i\infty}e^{\omega t}\left\{\frac{1}{[\omega-\Phi(p)]}-\frac{\gamma_0 p\xi}{[\omega-\Phi(p)]\,[\omega-\Phi(p+1)]}\right\}d\omega\,.$$

We can solve the ω integration on using the residue method (Beranrdini et al., 1993), to obtain

$$N(\gamma,t) \approx \frac{n}{2\pi i\gamma_0}\int_{\delta-i\infty}^{\delta+i\infty}\left(\frac{\gamma}{\gamma_0}\right)^{-(p+1)}\left\{e^{\Phi(p)t}-\gamma_0 p\xi\left[\frac{e^{\Phi(p)t}-e^{\Phi(p+1)t}}{[\Phi(p)-\Phi(p+1)]}\right]\right\}dp =$$

$$= \frac{n}{2\pi i\gamma_0}\int_{\delta-i\infty}^{\delta+i\infty}\left(\frac{\gamma}{\gamma_0}\right)^{-(p+1)}e^{\Phi(p)t}dp+$$

$$+\frac{n}{2\pi i\gamma_0}\,q\int_{\delta-i\infty}^{\delta+i\infty}\left(\frac{\gamma}{\gamma_0}\right)^{-(p+1)}\frac{p}{p+1+\frac{\lambda_1}{2\lambda_2}}\left[e^{\Phi(p)t}-e^{\Phi(p+1)t}\right]dp =$$

$$= \frac{n}{2\pi i\gamma_0}\int_{\delta-i\infty}^{\delta+i\infty}\left(\frac{\gamma}{\gamma_0}\right)^{-(p+1)}e^{\Phi(p)t}\left\{1+\frac{\gamma_0\xi}{2\lambda_2}\left[1-e^{(\Phi(p+1)-\Phi(p))t}\right]\right\}dp-$$

$$-\left(1+\frac{\lambda_1}{2\lambda_2}\right)\frac{n}{2\pi i\gamma_0}\,q\int_{\delta-i\infty}^{\delta+i\infty}\left(\frac{\gamma}{\gamma_0}\right)^{-(p+1)}\frac{e^{\Phi(p)t}-e^{\Phi(p+1)t}}{p+1+\frac{\lambda_1}{2\lambda_2}}dp\,.$$

The second term is zero, being proportional to

$$\int_{\delta-i\infty}^{\delta+i\infty}\left(\frac{\gamma}{\gamma_0}\right)^{-(p+1)}\frac{e^{\Phi(p)t}-e^{\Phi(p+1)t}}{p+1+\frac{\lambda_2}{2\lambda_1}}dp = 0\,,$$

because for $p=-1-\frac{\lambda_1}{2\lambda_2}$ we have $\Phi(p)=\Phi(p+1)$. On the other hand, the first term can be solved as in the previous section; finally, we have

$$N(\gamma,t) \approx N_0\left(\frac{\gamma}{\gamma_0}\right)^{-s-r\log\left(\frac{\gamma}{\gamma_0}\right)}\left[1+q\left(1-\frac{\gamma}{\langle\gamma\rangle}\right)\right],$$

where $\langle\gamma\rangle$ is defined by Eq. 2.7.

We note that the total power density of the electron distribution is

$$P \approx mc^2 2\lambda_2\, n\,\gamma_0\left\{\left(1+\frac{\lambda_1}{2\lambda_2}\right)\mathrm{e}^{(\lambda_1+2\lambda_2)t}+q\left[\left(1+\frac{\lambda_1}{2\lambda_2}\right)\left(\mathrm{e}^{(\lambda_1+2\lambda_2)t}-\mathrm{e}^{(\lambda_1+4\lambda_2)t}\right)-\mathrm{e}^{(2\lambda_1+6\lambda_2)t}\right]\right\}.$$

B.3 Continuous injection with radiative cooling

We now consider the diffusion equation in presence of continuous particle injection and radiative cooling; if energy losses can be written

$$\frac{d\gamma}{dt} = -\xi\,\gamma^2$$

and particles are injected with a constant power-law spectrum $I\,\gamma^{-s}$. In this case we have

$$\frac{\partial N(\gamma,\,t,)}{\partial t} = \xi \frac{\partial}{\partial \gamma}\left(\gamma^2 N\right) + I\gamma^{-s}\,. \tag{B.8}$$

Eq. B.8 can be solved with the characteristics method; we can write

$$\frac{\partial N(\gamma,\,t,)}{\partial t} - \xi\gamma^2 \frac{\partial N(\gamma,\,t,)}{\partial \gamma} = 2\xi\gamma N(\gamma,\,t,) + I\gamma^{-s}\,.$$

We write

$$\begin{aligned}
\frac{dt}{d\epsilon} &= 1\,,\\
\frac{d\gamma}{d\epsilon} &= -\xi\gamma^2\,,\\
\frac{dN}{d\epsilon} &= 2\xi\gamma\, N + I\gamma^{-s}
\end{aligned}$$

to obtain

$$\frac{d\gamma}{dt} = -\xi\gamma^2 \rightarrow \frac{1}{\gamma} = \xi\, t + c\,.$$

We then introduce the auxiliary function

$$\zeta = \frac{1}{\gamma} - \xi\, t \rightarrow \gamma = \frac{1}{\xi\, t + \zeta}\,; \tag{B.9}$$

so we have

$$\frac{dN}{dt} = 2\xi\gamma\, N + I\gamma^{-s} = \frac{2\xi}{\xi\, t + \zeta} + q(\xi\, t + \zeta)^s\,,$$

which has the solution

$$N(\zeta\, t) = (\xi\, t + \zeta)^2 \left\{\frac{A}{\zeta^2} + \frac{I}{\xi(s-1)}\left[(\xi\, t + \zeta)^{a-1} - \zeta^{a-1}\right]\right\}\,,$$

where A is a constant; on substituting back Eq. B.9 we finally obtain

$$N(\gamma\,, t) = \frac{A}{(1-\gamma\xi\, t)^2} + \frac{I}{\xi(s-1)}\gamma^{-(1+s)}\left[1 - (1-\gamma\xi\, t)^{s-1}\right].$$

For initial condition $N(\gamma\,, 0) = 0$ we have (Kardashev, 1962)

$$N(\gamma\,, t) = \frac{I}{\xi(s-1)}\gamma^{-(1+s)}\left[1 - (1-\gamma\xi\, t)^{s-1}\right]\,; \tag{B.10}$$

the distribution given in Eq. B.10 may be approximated by a broken power law, because it results

$$N(\gamma\,, t) \approx \begin{cases} I\, t\, \gamma^{-s} & \gamma \ll \frac{1}{\xi\, t}\,; \\ \frac{I}{\xi(s-1)}\,\gamma^{-(s+1)} & \gamma \gg \frac{1}{\xi\, t}\,. \end{cases}$$

Note that the total power density of the electron distribution for $s > 2$ is

$$P \approx mc^2 \left\{\xi\, I\, t\left(\frac{2-s}{3-s}\right)\left[(\xi\, t)^{3-s} - (\gamma_{min})^{3-s}\right] + \frac{I\,(\xi\, t)^{2-s}}{\xi(2-s)} + \frac{I}{2-s}\left[\left(1 - \frac{1}{\xi}\right)(\gamma_{max})^{2-s} - (\gamma_{min})^{2-s}\right]\right\}\,.$$

Appendix C

Spectral analysis of the HBL sample

Tables C.1, C.2, C.3 and C.4 report the log of the selected X-ray observations and the values of the spectral parameters we have derived for TeV HBLs in our sample.

In *XMM-Newton* Table C.1 and C.3 $Frame$ indicates the EPIC camera used (M1=MOS1 and M2=MOS2), the modes (PW=partial window and FW=full window) and the filter (Th=thin, Md=medium, Tk=thick) used for each pointing (see Sect. 5.3 for details), and the exposure is reported in seconds in the column $Exps$. In Table A.1 capital letters near the observation date indicate a different pointing in the same observation, while lower case letters refer to time resolved spectra (see also Tramacere et al., 2007). The capital letter F in the last column *XMM-Newton* table (A.1) indicates that the observation is too contaminated by solar flares to be used in our spectral analysis.

In *Swift* Table C.2 and C.4 the column $Frame$ reports on the observation modality (PC for photon counting and WT for windowed timed, see also Sect. 5.3 for details), and $Exps$ means the exposure time in seconds.

All other columns in each table refer to the log-parabolic model and the power-law with exponential cut-off bestfit. When the value estimated for a spectral parameter is consistent with zero in a 2σ interval, the values reported in each table refer to the power-law model bestfit. In these cases, the curvature parameter b, the SED peak energy E_p and the corresponding SED peak height S_p cannot be reliably evaluated, and are marked with a dashed line. The observations marked with the * in the following table have been rebinned only for 20 cts/bin. We find consistent spectral parameters (within a 1σ interval) from the two different values of column densities, in particular, in Fig. C.1 we show the value of the curvature parameter estimated with the different N_H reported by the Lockman & Savage (1995) and by the LAB survey (Kalberla et al., 2005).

Values of E_p are reported in keV, the normalization K in units of $10^{-4} photons\ cm^{-2}\ s^{-1}\ keV^{-1}$ and S_p in units of $10^{-13} erg\ cm^{-2}\ s^{-1}$ with F_X denoting the $2-10\ keV$ flux measured in units of $10^{-11} erg\ cm^{-2}\ s^{-1}$. For spectra with less than 30 bins we report only the estimate of the X-ray flux F_X with a power-law model absorbed by a galactic column density (see Sect. 5.4 for details).

Table C.1: *XMM-Newton* spectral analysis results with the LP model of the NBLs.

Obs ID	*Date*	Frame	Exps	a	b	E_p	K	S_p	F_X	χ^2_r
BZB J0208+3523										
0084140101	01/02/14	M1-FW(Me)	38070	2.09(0.03)	0.61(0.07)	0.85(0.06)	8(1)	13.0(0.2)	0.10	0.92(134)
0084140501	02/02/04	M1-FW(Me)	11680	1.95(0.05)	0.41(0.11)	1.16(0.14)	9(1)	13.9(0.3)	0.16	1.13(69)
BZB J0326+0225										
0094382501	02/02/05	M1-PW2(Me)	4563	2.36(0.07)	0.32(0.16)	0.27(0.21)	18(1)	36.6(7.4)	0.20	0.68(47)
BZB J0441+1504										
0152900201	03/09/05	M1	7438	2.13(0.08)	-	-	3(1)	-	0.07	1.44(16)
BZB J0744+7433										
0123100101	00/04/13	M1-PW3(Th)	10620	2.17(0.03)	0.16(0.06)	0.28(0.18)	26(1)	45.8(3.6)	0.44	1.01(135)
0123100201	00/04/12	M1-PW(Th)	19580	2.19(0.03)	0.18(0.06)	0.30(0.15)	23(1)	42.0(2.8)	0.38	1.00(141)
BZB J1231+6414										
0124900101	00/05/21	M1-FW(Th)	16220	2.15(0.04)	0.25(0.08)	0.50(0.18)	9(1)	15.9(0.7)	0.15	1.05(105)

Table C.2: *Swift* spectral analysis results with the LP model of the NBLs.

Obs ID	*Date*	Frame	Exps	a	b	E_p	K	S_p	F_X	χ^2_r
BZB J0123+3420										
00035000001	09/06/05	pc	1587	1.52(0.08)	0.66(0.18)	2.32(0.37)	76(3)	149.3(6.9)	2.02	0.83(25)
00035000002	06/07/06	pc	5414	1.72(0.05)	0.45(0.10)	2.05(0.23)	64(2)	113.2(3.5)	1.56	1.31(55)
00035000003	10/07/06	pc	2444	1.69(0.12)	0.57(0.28)	1.85(0.34)	73(4)	127.9(7.4)	1.63	1.47(16)
00030876001	18/01/07	pc	782	1.52(0.23)	0.66(0.51)	2.30(0.91)	93(8)	182.4(16.9)	2.46	0.51(5)
00035000005	07/09/07	pc	1018	1.78(0.12)	-	-	68(6)	-	2.41	0.58(7)
00035000009	15/09/07	pc	1289	1.61(0.26)	0.99(0.58)	1.57(0.24)	82(7)	143.4(13.5)	1.42	0.94(5)
00035000010	27/09/07	pc	754	1.52(0.35)	2.00(1.14)	1.32(0.15)	174(17)	297.4(32.3)	1.61	0.22(3)
00035000011	27/10/07	pc	1479	1.91(0.09)	0.25(0.23)	1.52(0.48)	67(3)	110.1(5.9)	1.52	1.11(19)
00035000013	09/11/07	pc	2105	1.79(0.08)	0.49(0.18)	1.64(0.23)	87(4)	149.7(7.2)	1.88	0.81(23)
00035000014	16/11/07	pc	1380	1.63(0.09)	0.79(0.19)	1.72(0.17)	85(4)	151.3(7.8)	1.72	1.57(20)
00037298001	06/03/08	pc	1248	1.72(0.11)	0.33(0.24)	2.69(1.34)	73(4)	134.2(8.2)	2.01	0.83(17)
00037298002	08/06/08	pc	4757	1.69(0.06)	0.49(0.12)	2.06(0.25)	68(2)	122.4(4.4)	1.66	1.32(43)
00037298003	28/08/09	pc	4816	1.70(0.06)	0.68(0.12)	1.66(0.12)	73(2)	126.4(4.3)	1.47	0.85(45)
BZB J0152+0147										
00031015005	02/12/07	pc	3123	2.10(0.06)	0.71(0.22)	0.48(0.15)	26(1)	42.6(1.8)	0.42	1.20(25)
00031015006	10/12/07	pc	2226	2.19(0.08)	0.26(0.22)	0.43(0.39)	23(1)	37.9(3.9)	0.33	0.91(14)
00031015002	13/11/07	pc	1738	2.17(0.10)	0.78(0.42)	0.77(0.16)	34(2)	55.9(3.4)	0.34	0.60(12)
00031015003	14/11/07	pc	1876	2.21(0.08)	0.90(0.26)	0.77(0.12)	30(2)	49.6(2.6)	0.26	1.21(15)
00031015004	15/11/07	pc	1822	2.30(0.08)	0.50(0.25)	0.50(0.22)	27(2)	48.5(3.8)	0.29	1.02(14)
00031015007	16/12/07	pc	1513	2.28(0.14)	-	-	42(4)	-	0.71	0.73(6)
00031015008	23/12/07	pc	2256	2.45(0.13)	-	-	11(1)	-	0.15	0.58(6)
00031015009	30/12/07	pc	4461	2.57(0.09)	0.88(0.34)	0.48(0.15)	10(1)	20.7(1.8)	0.06	0.88(12)
00031015010	06/01/08	pc	2644	1.91(0.09)	0.85(0.23)	1.13(0.12)	20(1)	32.6(1.8)	0.27	0.48(15)
00031015011	13/01/08	pc	2289	2.29(0.14)	-	-	14(2)	-	0.24	0.71(6)
BZB J0201+0034										
00038117001	05/06/09	pc	5041	1.92(0.08)	0.80(0.23)	1.13(0.12)	12(1)	19.2(1.0)	0.16	0.95(17)
BZB J0214+5144										
00038333001	10/12/08	pc	5040	1.90(0.13)	0.26(0.25)	1.55(0.47)	52(2)	84.9(4.2)	1.16	1.01(22)
00038333002	11/12/08	pc	780	1.34(0.71)	1.66(1.58)	1.58(0.26)	42(6)	79.2(10.3)	0.61	1.17(2)
00038333003	16/09/09	pc	3376	1.70(0.18)	0.57(0.33)	1.82(0.31)	50(3)	87.4(5.3)	1.10	1.52(15)
BZB J0325-1646										
00035005001	29/06/05	pc	7671	2.91(0.11)	-	-	4(1)	-	0.03	0.43(10)
BZB J0326+0225										
00035006001	26/06/05	pc	10680	2.28(0.01)	0.50(0.23)	0.52(0.21)	7.5(0.4)	13.2(1.0)	0.08	0.51(19)
00035006002	29/06/05	pc	4650	2.54(0.14)	-	-	7(1)	-	0.08	0.43(5)
00035006003	11/07/05	pc	6549	2.44(0.20)	-	-	5(1)	-	0.06	1.18(5)
BZB J0441+1504										
00036806002	08/01/08	pc	7059	1.14(0.15)	1.23(0.26)	2.23(0.16)	18(1)	40.5(1.8)	0.47	1.24(31)

Table C.2: continued

Obs ID	*Date*	Frame	Exps	a	b	E_p	K	S_p	F_X	χ^2_r
BZB J0442-0018										
00036312005	19/10/08	pc	10780	2.00(0.18)	-	-	2(1)	-	0.05	0.38(4)
BZB J0621-3411										
00038819001	29/07/09	pc	949	0.89(0.51)	1.55(1.12)	2.29(0.65)	17(2)	43.9(5.1)	0.49	0.65(2)
BZB J0751+1730										
00036808001	30/05/07	pc	3102	1.22(0.38)	1.35(0.84)	1.94(0.36)	7(1)	14.2(1.6)	0.15	0.08(3)
BZB J0847+1133										
00037396001	29/02/08	pc	2022	1.89(0.11)	-	-	35(3)	-	1.05	1.27(8)
BZB J0916+5238										
00038165001	07/03/09	pc	7710	2.09(0.06)	0.56(0.18)	0.83(0.13)	9.5(0.4)	15.4(0.7)	0.13	0.84(23)
BZB J0952+7502										
00036810001	20/05/07	pc	9759	1.80(0.07)	0.47(0.16)	1.63(0.25)	7.5(0.3)	12.6(0.6)	0.16	0.86(23)
00036810002	04/10/07	pc	2230	2.38(0.33)	-	-	5(1)	-	0.08	0.58(1)
BZB J1010-3119										
00030940002	17/05/07	pc	1481	2.10(0.11)	0.34(0.30)	0.72(0.43)	43(2)	69.8(4.4)	0.68	0.90(14)
00030940003	18/05/07	wt	774	2.00(0.17)	0.55(0.40)	1.00(0.34)	51(4)	82.4(5.9)	0.77	1.04(8)
00030940004	18/05/07	pc	1968	1.81(0.11)	1.18(0.27)	1.21(0.10)	44(2)	71.7(3.7)	0.51	1.08(18)
BZB J1022+5124										
00036811001	13/01/08	pc	5703	1.60(0.08)	-	-	8(1)	-	0.40	1.36(14)
BZB J1053+4929										
00031594001	21/01/10	pc	5243	2.22(0.11)	0.98(0.46)	0.77(0.13)	6.4(0.5)	10.5(0.8)	0.05	1.62(8)
BZB J1056+0252										
00037547001	08/06/07	pc	4725	1.66(0.07)	0.57(0.15)	1.97(0.25)	19(1)	34.6(1.5)	0.45	0.81(29)
BZB J1111+3452										
00038219001	18/04/09	pc	4590	1.75(0.11)	0.56(0.31)	1.67(0.39)	9(1)	14.9(1.0)	0.18	1.02(11)
BZB J1117+2014										
00038451001	20/04/09	pc	1341	2.42(0.13)	0.87(0.55)	0.57(0.24)	21(2)	38.1(3.7)	0.14	0.51(6)
BZB J1136+6737										
00037135001	25/05/07	pc	2788	1.61(0.09)	0.79(0.19)	1.76(0.18)	49(2)	87.8(4.8)	1.02	1.19(18)
00037135002	30/05/07	pc	4487	1.75(0.07)	0.67(0.18)	1.53(0.17)	44(2)	74.1(3.6)	0.83	0.73(22)
00037135003	16/02/08	pc	4291	1.51(0.05)	0.62(0.10)	2.50(0.26)	95(3)	190.9(5.8)	2.67	0.86(62)
00036812001	29/01/08	pc	3983	1.48(0.07)	0.36(0.15)	5.16(2.84)	48(2)	117.9(12.6)	1.83	1.05(28)
00036812002	30/01/08	pc	2304	1.69(0.08)	0.40(0.18)	2.40(0.72)	49(2)	89.1(4.8)	1.30	1.00(20)
BZB J1145-0340										
00036813001	09/11/07	pc	2870	2.19(0.16)	-	-	6(1)	-	0.12	1.17(3)
00036813002	06/12/07	pc	2934	1.64(0.17)	1.22(0.43)	1.40(0.16)	9(1)	14.6(1.3)	0.12	0.69(5)

Table C.2: continued

Obs ID	*Date*	Frame	Exps	a	b	E_p	K	S_p	F_X	χ^2_r
BZB J1237+6258										
00042002001	14/12/04	pc	3114	2.29(0.32)	-	-	4(1)	-	0.06	0.10(1)
00060001001	28/12/04	pc	2677	2.85(0.41)	-	-	5(1)	-	0.04	0.37(1)
00042002008	10/03/05	wt	1105	2.37(0.20)	-	-	14(2)	-	0.22	1.79(3)
00042002018	29/11/05	pc	1593	1.63(0.42)	1.50(1.36)	1.33(0.23)	12(1)	20.6(2.6)	0.14	0.56(2)
00042002024	13/03/07	pc	3664	2.23(0.14)	-	-	6(1)	-	0.11	0.65(5)
00042002028	01/10/07	pc	1124	1.86(0.34)	-	-	12(1)	-	0.37	0.95(1)
00042002035	27/01/10	pc	4729	1.97(0.22)	0.69(0.59)	1.05(0.35)	5(1)	7.9(0.7)	0.07	1.02(4)
BZB J1253-3931										
00037538001	20/12/08	pc	4651	1.42(0.11)	0.60(0.19)	3.01(0.63)	20(1)	43.8(2.2)	0.64	0.72(25)
BZB J1257+2412										
00031203001	09/05/08	pc	2200	1.90(0.08)	-	-	16(1)	-	0.49	1.16(12)
BZB J1341+3959										
00038268001	15/10/08	pc	5198	1.64(0.06)	0.60(0.12)	1.99(0.22)	23(1)	41.1(1.6)	0.54	1.02(38)
00038268002	21/12/09	pc	5901	1.65(0.08)	0.72(0.17)	1.76(0.18)	14.1(0.6)	25.0(1.2)	0.30	1.42(25)
BZB J1417+2543										
00035270001	20/12/05	pc	8547	1.85(0.03)	0.42(0.08)	1.52(0.11)	62(1)	101.7(2.5)	1.29	1.20(84)
00056620002	26/05/05	pc	775	1.51(0.26)	-	-	74(8)	-	4.07	0.59(3)
00056620002	26/05/05	wt	1015	1.87(0.07)	0.51(0.19)	1.34(0.18)	81(4)	132.8(6.2)	1.52	0.75(25)
00035270002	11/07/06	pc	1882	1.78(0.08)	0.57(0.18)	1.57(0.21)	62(3)	104.4(5.5)	1.25	0.42(19)
00031204001	10/05/08	pc	1694	1.83(0.07)	0.73(0.20)	1.31(0.12)	51(2)	83.5(3.9)	0.83	1.08(25)
00031204002	30/05/08	pc	1664	1.89(0.09)	0.52(0.29)	1.27(0.23)	47(3)	76.8(4.8)	0.85	0.89(13)
BZB J1439+3932										
00037514002	15/10/08	pc	1458	2.48(0.20)	-	-	16(1)	-	0.21	0.33(4)
00037514001	07/06/08	pc	832	1.99(0.27)	-	-	20(2)	-	0.52	0.28(2)
BZB J1442+1200										
00031218002	12/06/08	pc	1732	1.85(0.11)	0.37(0.33)	1.62(0.58)	39(3)	65.3(4.8)	0.87	1.45(9)
00031218003	26/02/10	pc	1110	2.11(0.23)	-	-	41(4)	-	0.88	0.16(3)
00031218005	09/03/10	pc	1058	1.56(0.30)	1.98(0.91)	1.29(0.14)	44(5)	75.3(8.6)	0.40	1.79(3)
BZB J1534+3715										
00038300001	12/12/08	pc	14760	2.85(0.15)	-	-	1.3(0.1)	-	0.01	0.93(5)
BZB J1605+5421										
00038303001	18/01/09	pc	7066	1.40(0.12)	0.79(0.33)	2.41(0.69)	4.9(0.3)	10.3(0.8)	0.14	0.87(10)
BZB J1728+5013										
00040635001	05/04/10	pc	1395	1.98(0.10)	0.70(0.35)	1.03(0.17)	50(3)	80.2(5.5)	0.68	0.64(10)
00040635003	05/04/10	pc	2150	2.11(0.07)	0.34(0.20)	0.69(0.25)	44(2)	71.8(3.4)	0.69	1.42(20)
00040635004	01/05/10	pc	1667	2.31(0.11)	-	-	44(4)	-	0.71	0.59(7)

Table C.2: continued

Obs ID	*Date*	Frame	Exps	a	b	E_p	K	S_p	F_X	χ^2_r
BZB J1743+1935										
00030950001	15/06/07	pc	1918	2.00(0.09)	0.34(0.24)	1.01(0.32)	39(2)	62.0(3.1)	0.71	1.85(19)
BZB J2131-0915										
00037543001	30/03/09	pc	5189	2.17(0.06)	0.77(0.22)	0.78(0.10)	17(1)	27.4(1.2)	0.17	1.01(23)
BZB J2250+3824										
00039211001	10/08/09	pc	1110	2.36(0.14)	-	-	28(2)	-	0.41	0.75(5)
00039211002	18/02/10	pc	2996	2.47(0.11)	-	-	15(1)	-	0.19	0.95(9)
00040151001	17/04/10	pc	1654	2.83(0.34)	-	-	14(2)	-	0.11	2.39(1)
00039211003	18/04/10	pc	3446	2.53(0.12)	0.46(0.31)	0.27(0.29)	17(1)	38.2(14.1)	0.13	1.11(11)
BZB J2308-2219										
00036815001	29/09/07	pc	7289	1.98(0.21)	-	-	3(1)	-	0.07	0.62(3)
BZB J2322+3436										
00040684002	17/02/10	pc	3523	2.33(0.21)	-	-	5(1)	-	0.07	1.40(2)
BZB J2343+3439										
00037545002	02/06/08	pc	3336	1.78(0.09)	0.74(0.25)	1.41(0.16)	24(1)	39.5(2.0)	0.41	0.43(19)
00037545001	30/05/08	pc	2381	1.53(0.14)	1.67(0.38)	1.38(0.09)	25(1)	43.4(2.6)	0.28	0.69(13)

Table C.3: *XMM-Newton* spectral analysis results with the EC model of the NBLs.

Obs ID	*Date*	Frame	Exps	a	E_p	K	S_p	F_X	χ^2_r
BZB J0208+3523									
0084140101	01/02/14	M1-FW(Me)	38070	1.86(0.06)	0.41(0.11)	10(1)	13.4(0.4)	0.10	0.98(134)
0084140501	02/02/04	M1-FW(Me)	11680	1.84(0.09)	1.03(0.34)	10(1)	13.7(0.3)	0.15	1.15(69)
BZB J0326+0225									
0094382501	02/02/05	M1-PW2(Me)	4563	2.64(0.45)	0.10(0.09)	21(3)	32.1(18.0)	0.21	0.70(47)
BZB J0441+1504									
0152900201	03/09/05	M1	7438	2.12(0.30)	0.12(0.23)	3(1)	5.2(0.6)	0.07	1.48(16)
BZB J0744+7433									
0123100201	00/04/12	M1-PW(Th)	19580	2.12(0.05)	0.09(0.03)	25(1)	41.5(5.9)	0.38	0.94(141)
BZB J1231+6414									
0124900101	00/05/21	M1-FW(Th)	16220	2.04(0.07)	0.10(0.03)	11(8)	16.5(2.6)	0.15	0.99(105)

Table C.4: *Swift* spectral analysis results with the EC model of the NBLs.

Obs ID	*Date*	Frame	Exps	a	E_p	K	S_p	F_X	χ^2_r
BZB J0123+3420									
00035000001	09/06/05	pc	1587	1.24(0.19)	2.23(0.27)	113(15)	156.1(8.7)	1.80	0.66(25)
00035000002	06/07/06	pc	5414	1.47(0.10)	0.10(0.01)	80(6)	97.1(0.1)	1.50	1.15(55)
00035000003	10/07/06	pc	2444	1.48(0.18)	0.08(0.01)	84(1)	99.7(0.1)	1.73	1.18(16)
00030876001	18/01/07	pc	782	1.01(0.48)	2.01(0.47)	157(58)	186.8(15.6)	1.84	1.28(5)
00035000005	07/09/07	pc	1018	1.41(0.29)	0.10(0.01)	87(16)	103.3(12.7)	1.67	0.31(6)
00035000009	15/09/07	pc	1289	1.68(0.67)	0.30(2.51)	88(45)	121.9(52.2)	2.44	0.06(5)
00035000010	27/09/07	pc	754	0.17(1.05)	1.40(0.15)	635(489)	300.5(33.7)	1.29	0.13(3)
00035000011	27/10/07	pc	1479	1.90(0.32)	2.73(6.23)	68(18)	109.5(9.5)	1.70	1.17(19)
00035000013	09/11/07	pc	2105	1.51(0.20)	1.81(0.26)	115(17)	150.8(7.9)	1.70	1.03(23)
00035000014	16/11/07	pc	1380	1.18(0.19)	1.93(0.17)	126(16)	152.7(8.6)	1.54	1.43(20)
00037298001	06/03/08	pc	1248	1.32(0.27)	0.14(0.10)	1(1)	124.1(13.8)	2.07	1.54(17)
00037298002	08/06/08	pc	4757	1.53(0.10)	0.11(0.01)	74(6)	92.7(3.1)	1.57	1.34(43)
00037298003	28/08/09	pc	4816	1.32(0.11)	1.94(0.12)	102(8)	129.6(4.7)	1.40	0.64(45)
BZB J0152+0147									
00031015005	02/12/07	pc	3123	1.88(0.16)	0.09(0.12)	31(7)	53.2(34.8)	0.40	1.19(25)
00031015006	10/12/07	pc	2226	2.07(0.20)	0.11(0.07)	24(7)	45.6(15.5)	0.33	0.94(14)
00031015002	13/11/07	pc	1738	1.51(0.38)	0.29(0.44)	62(29)	67.3(13.1)	0.27	0.59(12)
00031015003	14/11/07	pc	1876	1.57(0.24)	0.20(0.10)	53(15)	62.2(8.1)	0.24	1.16(15)
00031015004	15/11/07	pc	1822	1.91(0.23)	0.09(0.10)	38(11)	63.8(35.9)	0.26	0.95(14)
00031015007	16/12/07	pc	1513	1.89(0.68)	0.12(0.17)	63(54)	102.0(61.1)	0.39	0.78(5)
00031015008	23/12/07	pc	2256	2.07(0.60)	0.10(0.52)	18(20)	34.5(96.2)	0.08	0.59(5)
00031015009	30/12/07	pc	4461	1.84(0.30)	0.10(0.14)	20(10)	29.0(23.1)	0.05	0.83(12)
00031015010	06/01/08	pc	2644	1.33(0.22)	0.95(0.26)	33(9)	34.3(1.7)	0.24	0.41(15)
00031015011	13/01/08	pc	2289	2.23(0.65)	0.11(0.27)	15(18)	35.1(44.5)	0.21	0.82(5)
BZB J0201+0034									
00038117001	05/06/09	pc	5041	1.45(0.20)	0.71(0.40)	18(5)	20.6(1.1)	0.15	1.05(17)
BZB J0214+5144									
00038333001	10/12/08	pc	5040	1.77(0.24)	2.48(0.27)	59(10)	86.2(4.6)	1.12	0.98(22)
00038333002	11/12/08	pc	780	0.44(1.45)	1.87(0.25)	108(84)	74.8(10.3)	0.51	1.06(2)
00038333003	16/09/09	pc	3376	1.50(0.30)	2.50(0.25)	63(12)	88.6(5.8)	1.05	1.51(15)
BZB J0325-1646									
00035005001	29/06/05	pc	7671	2.88(0.46)	0.07(0.13)	4(5)	19.1(14.4)	0.03	0.47(9)
BZB J0326+0225									
00035006001	26/06/05	pc	10680	1.95(0.21)	0.85(0.23)	10(3)	11.0(0.5)	0.08	0.52(19)
00035006002	29/06/05	pc	4650	2.12(0.46)	0.52(0.80)	8(5)	10.4(1.9)	0.07	0.30(4)
00035006003	11/07/05	pc	6549	2.37(0.65)	0.13(0.29)	5(6)	7.7(2.8)	0.07	1.19(4)
BZB J0441+1504									
00036806002	08/01/08	pc	7059	0.83(0.24)	2.62(0.14)	29(5)	41.2(1.9)	0.45	1.36(31)

Table C.4: continued

Obs ID	*Date*	Frame	Exps	a	E_p	K	S_p	F_X	χ^2_r
BZB J0442-0018									
00036312005	19/10/08	pc	10780	1.66(0.88)	1.26(0.72)	3(4)	3.6(0.4)	0.04	0.42(3)
BZB J0621-3411									
00038819001	29/07/09	pc	949	0.21(1.02)	2.33(0.54)	37(30)	44.9(5.6)	0.42	0.71(2)
BZB J0751+1730									
00036808001	30/05/07	pc	3102	0.61(0.77)	2.06(0.34)	13(10)	14.5(1.7)	0.13	0.13(3)
BZB J0847+1133									
00037396001	29/02/08	pc	2022	1.89(0.40)	1.26(0.56)	35(17)	57.7(4.9)	1.05	1.41(7)
BZB J0916+5238									
00038165001	07/03/09	pc	7710	1.77(0.16)	0.07(0.06)	12(3)	21.2(7.1)	0.12	0.92(23)
BZB J0952+7502									
00036810001	20/05/07	pc	9759	1.53(0.15)	1.09(0.60)	9(2)	13.0(0.6)	0.15	0.89(23)
BZB J1010-3119									
00030940002	17/05/07	pc	1481	1.86(0.28)	1.39(0.24)	53(14)	63.5(3.8)	0.62	0.87(14)
00030940003	18/05/07	wt	774	1.58(0.39)	1.52(0.23)	74(22)	78.7(6.5)	0.68	0.92(8)
00030940004	18/05/07	pc	1968	1.12(0.25)	1.54(0.10)	82(16)	68.5(3.8)	0.46	1.16(18)
BZB J1022+5124									
00036811001	13/01/08	pc	5703	1.58(0.26)	0.24(0.47)	8(3)	14.2(2.3)	0.40	1.43(13)
BZB J1053+4929									
00031594001	21/01/10	pc	5243	1.42(0.41)	0.11(0.15)	13(10)	15.1(11.2)	0.04	1.67(8)
BZB J1056+0252									
00037547001	08/06/07	pc	4725	1.36(0.14)	2.13(0.25)	25(4)	35.3(1.7)	0.43	0.82(29)
BZB J1111+3452									
00038219001	18/04/09	pc	4590	1.24(0.30)	1.33(0.35)	14(6)	15.9(1.1)	0.15	0.84(11)
BZB J1117+2014									
00038451001	20/04/09	pc	1341	1.74(0.49)	0.12(0.15)	39(27)	58.4(41.6)	0.12	0.52(6)
BZB J1136+6737									
00037135001	25/05/07	pc	2788	1.19(0.18)	1.58(0.26)	71(11)	90.0(5.0)	0.96	1.27(18)
00037135002	30/05/07	pc	4487	1.33(0.17)	0.94(0.46)	62(10)	78.2(3.4)	0.77	0.78(22)
00037135003	16/02/08	pc	4291	1.17(0.10)	2.47(0.31)	127(8)	192.8(6.4)	2.50	0.88(62)
00036812001	29/01/08	pc	3983	1.30(0.14)	0.10(0.01)	56(7)	79.2(5.3)	1.75	1.07(28)
00036812002	30/01/08	pc	2304	1.43(0.17)	1.83(0.77)	61(10)	90.1(5.1)	1.20	0.94(20)
BZB J1145-0340									
00036813001	09/11/07	pc	2870	2.18(0.70)	0.08(0.69)	6(5)	12.0(44.7)	0.12	1.72(2)
00036813002	06/12/07	pc	2934	0.96(0.40)	1.39(0.25)	16(8)	14.9(1.4)	0.11	0.85(5)

Table C.4: continued

Obs ID	*Date*	Frame	Exps	a	E_p	K	S_p	F_X	χ^2_r
BZB J1237+6258									
00042002008	10/03/05	wt	1105	1.76(0.53)	0.11(0.15)	18(14)	30.0(20.9)	0.19	2.37(2)
00042002018	29/11/05	pc	1593	0.98(0.70)	0.98(0.43)	26(26)	21.9(2.2)	0.12	0.35(2)
00042002024	13/03/07	pc	3664	1.89(0.43)	0.07(0.39)	8(6)	14.8(31.1)	0.09	0.80(4)
00042002035	27/01/10	pc	4729	1.82(0.40)	0.13(0.10)	6(4)	10.9(3.2)	0.07	0.92(4)
BZB J1253-3931									
00037538001	20/12/08	pc	4651	1.15(0.18)	0.15(0.04)	26(4)	26.5(1.7)	0.60	0.68(25)
BZB J1257+2412									
00031203001	09/05/08	pc	2200	1.62(0.30)	5.06(28.73)	21(9)	27.0(11.1)	0.35	1.15(11)
BZB J1341+3959									
00038268001	15/10/08	pc	5198	1.37(0.11)	1.58(0.38)	28(4)	41.4(1.6)	0.53	1.14(38)
00038268002	21/12/09	pc	5901	1.18(0.17)	1.47(0.23)	21(4)	26.2(1.2)	0.27	1.28(25)
BZB J1417+2543									
00056620002	26/05/05	pc	775	1.49(0.99)	0.32(2.16)	73(74)	114.0(71.5)	4.14	0.58(2)
00056620002	26/05/05	wt	1015	1.54(0.18)	0.17(0.15)	107(16)	153.0(14.4)	1.39	0.77(25)
00035270002	11/07/06	pc	1882	1.44(0.17)	1.06(0.49)	82(12)	109.6(5.0)	1.18	0.41(19)
00031204001	10/05/08	pc	1694	1.26(0.19)	1.00(0.25)	83(14)	90.7(3.8)	0.71	0.90(25)
00031204002	30/05/08	pc	1664	1.53(0.26)	0.12(0.08)	65(18)	90.7(14.6)	0.75	0.89(13)
BZB J1439+3932									
00037514002	15/10/08	pc	1458	2.41(0.66)	0.09(0.50)	17(23)	56.7(151.9)	0.18	0.39(3)
00037514001	07/06/08	pc	832	2.21(1.28)	0.15(0.49)	20(49)	53.2(46.5)	0.38	1.30(1)
BZB J1442+1200									
00031218003	26/02/10	pc	1110	2.13(0.86)	0.15(0.41)	41(52)	94.6(51.1)	0.86	0.16(2)
00031218005	09/03/10	pc	1058	0.15(0.88)	1.26(0.19)	164(106)	80.5(9.2)	0.33	1.60(3)
BZB J1605+5421									
00038303001	18/01/09	pc	7066	0.91(0.31)	2.35(0.74)	8(3)	10.5(0.8)	0.12	0.90(10)
BZB J1728+5013									
00040635001	05/04/10	pc	1395	1.44(0.32)	0.62(0.55)	80(26)	88.8(7.0)	0.57	0.61(10)
00040635003	05/04/10	pc	2150	1.86(0.18)	0.08(0.11)	54(11)	92.7(55.7)	0.65	1.39(20)
00040635004	01/05/10	pc	1667	1.99(0.41)	0.09(0.24)	59(28)	108.7(143.9)	0.50	0.56(6)
BZB J1743+1935									
00030950001	15/06/07	pc	1918	1.79(0.23)	1.56(0.26)	46(10)	59.9(3.4)	0.67	1.80(19)
BZB J2131-0915									
00037543001	30/03/09	pc	5189	1.63(0.20)	0.18(0.09)	26(8)	31.7(3.4)	0.15	1.07(23)
BZB J2250+3824									
00039211001	10/08/09	pc	1110	2.35(0.59)	0.55(2.12)	28(15)	39.0(9.2)	0.41	0.91(4)
00039211002	18/02/10	pc	2996	2.47(0.42)	0.15(0.19)	15(9)	22.2(4.9)	0.19	1.04(8)
00039211003	18/04/10	pc	3446	2.25(0.29)	0.58(0.39)	22(7)	23.9(2.2)	0.13	1.09(11)

Table C.4: continued

Obs ID	*Date*	Frame	Exps	a	E_p	K	S_p	F_X	χ^2_r
BZB J2308-2219									
00036815001	29/09/07	pc	7289	1.97(0.72)	1.76(1.03)	3(3)	4.5(0.5)	0.07	0.60(2)
BZB J2322+3436									
00040684002	17/02/10	pc	3523	1.68(1.16)	1.00(0.91)	7(10)	7.1(0.9)	0.05	2.40(1)
BZB J2343+3439									
00037545002	02/06/08	pc	3336	1.31(0.24)	1.71(0.16)	36(9)	39.5(2.1)	0.36	0.44(19)
00037545001	30/05/08	pc	2381	0.51(0.34)	1.58(0.10)	65(20)	43.2(2.7)	0.25	0.60(13)

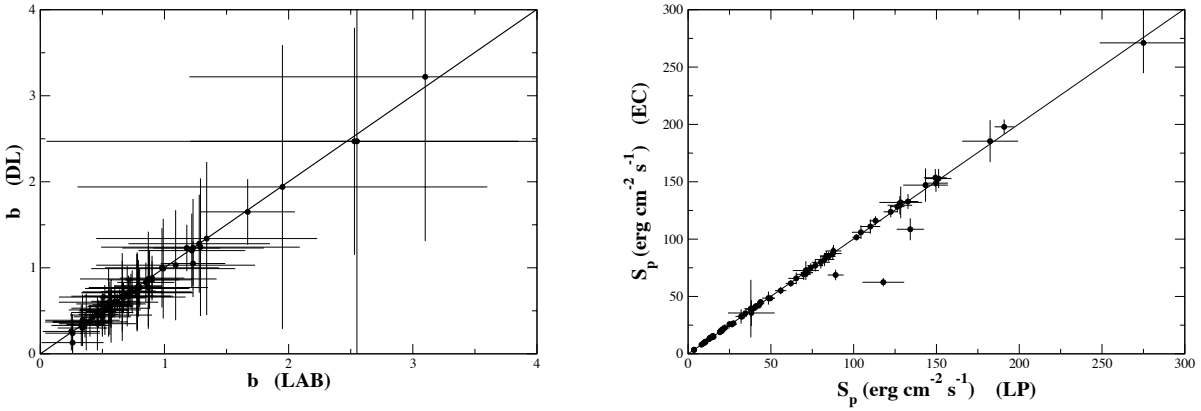

Figure C.1: Left) The curvature parameter evaluated by using the LP model with the two different Galactic N_H value of the absorption as reported by the Lockman & Savage (1995) and the LAB survey one (Kalberla et al., 2005). The spectral curvature of the LP model is not significantly affected by the choice of the Galactic absorption value in the fitting procedure. Right) The SED peak height S_p evaluated by using the LP and the EC models with the same Galactic N_H from the LAB survey (Kalberla et al., 2005) for the HBL sample.

Bibliography

Abdo, A., A., Ackermann, M., Ajello, M., et al. 2010a, ApJ, 710, 1271

Abdo, A., A., Ackermann, M., Agudo, I., et al. 2010b, ApJ, 716, 30

Abdo, A., A., Ackermann, M., Ajello, M., et al. 2010c, Nat, 463, 919

Aharonian, F., Akhperjanian, A., G., Bazer-Bachi, A. R., et al. 2007, ApJ, 664, L71

Aharonian, F.; Akhperjanian, A., G., Anton, G., et al. 2009a, ApJ, 695, 40

Aharonian, F., Akhperjanian, A., G., Anton, G., et al. 2009b, A&A, 502, 749

Aharonian, F., Akhperjanian, A., G., Anton, G. 2010, A&A, 521, 69

Albert, J., Aliu, E., Anderhub, H., et al. 2007a, ApJ, 669, 862

Albert, J., Aliu, E., Anderhub, H., et al. 2007b. ApJ, 666, L17

Albert, J., Aliu, E., Anderhub, H, et al. 2008, Sci, 320, 1752

Antonucci, R., 1993, ARA&A, 31, 473

Arnaud, K., A. 1996, "Astronomical Data Analysis Software and Systems V", eds. Jacoby G. and Barnes J., p17, ASP Conf. Series volume 101

Band, D., L., & Grindlay, J., E. 1985, ApJ, 298, 128

Begelman, M. C., Fabian, A., & Rees, M. J. 2008, MNRAS, 384, L19

Begelman, M., C., Blandford, R., D. & Rees, M., J. 1984, RvMP, 56, 255

Bernardini, C., Ragnisco, O., & Santini, P., 1993, *Metodi matematici della fisica*, Roma, Carocci

Bettoni, D., Falomo, R., Fasano, G., et al. 2003, A&A, 399, 869

Blandford, R., D., & Znajek, R., L. 1977, MNRAS, 179, 433

Blandford, R., D., & Rees, M., J. 1978, PROC. Ṗittsburgh Conference on BL Lac objects", 328

Blandford, R., D., & Payne, D., G. 1982, MNRAS, 199, 883

Blandford, R. D. 1990, in Saas-Fee Advanced Course 20, Active Galactic Nuclei, ed. R. D. Blandford, H. Netzer, & L. Woltjer (Springer), 161

Blumenthal, G., R., & Gould, R., J. 1970, Rev. Mod. Phys., 42, 237

Blustin, A. J., Page, M. J., & Branduardi-Raymont, G., 2004, A&A, 417, 61

Böttcher, M. 2007, Ap&SS, 309, 95

Burrows, D., Hill, J., E., Nousek, J., A., et al. 2005, SSRv., 120, 165

Campana, R., Massaro, E., & Mineo, T., 2009, A&A, 499, 847

Casula, V. 2008, Thesis

Cavaliere, A., & Morrison, P. 1980, ApJ, 238, 63

Cavaliere, A., & D'Elia, V. 2002, ApJ, 571, 226

Celotti, A., Ghisellini, G. & Chiaberge, M. 2001, MNRAS, 321, 1

Celotti, A., Ghisellini, G. & Fabian, A. C. 2007, MNRAS, 375, 417

Celotti, A. & Ghisellini, G. 2008, MNRAS, 385, 283

Chen, A. W., DAmmando, F., Villata, M., et al. 2008, A&A, 489, L37

Dermer, C., D. & Schlickeiser, R. 1993, ApJ, 416, 458

Dermer, C., D. & Schlickeiser, R. 2002, ApJ, 575, 667

Dermer, C. D., Finke, Justin, D. & Menon, G. 2008, in Proceedings of the Workshop on Blazar Variability across the Electromagnetic Spectrum, published online at http://pos.sissa.it/archive/conferences/063/019/BLAZARS2008_019.pdf

Di Sciascio, G. and the ARGO-YBJ Collaboration 2010, MmSAI, 81, 326

Djannati-Atai, A., Piron, F., Barrau, A., et al. 1999, A&A, 350, 17

Donnarumma, I., Vittorini, V., Vercellone. S., et al. 2009, ApJ, 691, L13

Dunkley, J., Komatsu, E., Nolta, M. R., et al. 2009, ApJS, 180, 306

Dunkley, J. 2009 ApJ, 701, 1804

Falomo, R., Kotilainen, J., K., Carangelo, N., et al. 2003, ApJ, 595, 624

Faranoff, B. L., Riley, J. M., 1974, MNRAS, 167, 31

Fermi, E. 1954, Phys. Rev., 75, 1169

Ferrarese, L., & Merritt, D. 2000, ApJ, 539, L9

Fossati, G., Buckley, J. H., Bond, I. H., et al. 2008, ApJ, 677, 906

Freeman, P., Doe, S., & Siemiginowska, A. 2001, Proc. SPIE, 4477, 76

Gebhardt, K., Bender, R., Bower, G., et al. 2000, ApJ, 539, L13

Georganopoulos, M., & Kazanas, D. 2003, ApJ, 594, 27

Georganopoulos, M., Perlman, E. S., & Kazanas, D. 2005, ApJ, 634, L33

Ghisellini, G. & Maraschi, L. 1989, ApJ, 340, 181

Ghisellini, G., Celotti, A., Fossati, G., et al. 1998, MNRAS, 301, 451

Ghisellini, G., Padovani, P., Celotti, A., et al. 1993, ApJ, 407, 65

Ghisellini, G., Maraschi, L., Tavecchio, F. 2009a, MNRAS, 396, 105

Ghisellini, G. & Tavecchio, F. 2009b, MNRAS, 397, 985

Ghosh, P., & Abramowicz, M. 1997, MNRAS, 292, 887

Giannios, D., Uzdensky, D. A., & Begelman, M. C. 2009, MNRAS, 395, 29

Giommi, P., Piranomonte, S., Perri, M., et al. 2005, A&A, 434, 385

Giommi, P., Colafrancesco, S., Cutini, S., et al. 2008, A&A, 487, L49

Gould, R., J. 1979, A&A, 76, 306

Hill, J., E., Burrows, D., N., Nousek, J., A., et al. 2004, SPIE, 5165, 217

Hoffmeister, C., 1929, AN, 236, 233

Huges, P., A. 1991, *Beams and Jets in Astrophysics*, Cambridge, Cambridge Univ. Press

Inoue, S., & Takahara F. 1996, ApJ, 463, 555

Ioka, K., Nakamura, T., 2002, ApJ, 570, L21

Jackson, J., D. 2001, *Elettrodinamica classica*, Bologna, Zanichelli

Jones, F., C. 1968, Phys. Rev. 167, 1159

Jones, T., W., O'Dell, S., L., & Stein, W., A. 1974, ApJ, 188, 353

Kalberla, P., M., W., Burton, W., B., & Hartmann, D. 2005, A&A, 440, 775

Kaplan, S., A. 1956, Sov. Phys., 2, 2

Kardashev, N., S. 1962, SvA, 6, 317

Katarzyński, K., Ghisellini, G., Tavecchio, F., et al. 2005, A&A, 433, 479

Kellermann, K. I., Sramek, R., Schmidt, M., Schaffer, D. B., Green, R., 1989, AJ, 98, 1195

Kembhavi, A., K., Narlikar, J., V. 1999, *Quasars and Active Galactic Nuclei*, Cambridge, Cambridge Univ. Press

Königl, A. 1986, NYASA, 470, 88

Konopelko, A., Mastichiadis, A., Kirk, J., et al. 2003, ApJ, 597, 851

Krolik, J. H. 1999, ApJ, 515, 73

Landau, R., Golisch, B., Jones, T., et al. 1986, ApJ, 308, 78

Lapi, A., Cavaliere, A., & Menci, N. 2005, ApJ, 619, 90

Laurent-Muehleisen, S., A., Kollgaard, R., I., Feigelson, E., D, et al. 1999 ApJ, 525, 127

Lenain, J.-P., Boisson, C., & Sol, H. 2008, IJMPD, 17, 1577

Lin, Y., C., Bertsch, D., L., Dingus, B., L., et al. 1995, ApJ, 442, 96

Lind, K., M., & Blandford, R. 1985, ApJ, 295, 358

Litvinenko, Y., E. 1996 ApJ, 462, 997

Litvinenko, Y., E. 1999 A&A, 349, 685

Livio, M., Ogilvie, G., & Pringle, J. 1999, ApJ, 512, 100

Lockman, F. J., & Savage, B. D. 1995, ApJS, 97, 1

Loiseau, N. 2004, "User's guide to the *XMM-Newton* Science Analysis System" (issue 3.1)

Longair, M., S. 1997, *High Energy Astrophysics*, Cambridge, Cambridge Univ. Press

Maraschi, L., Ghisellini, G., & Celotti, A. 1992, ApJ, 397, L5

Maraschi, L., & Tavecchio, F. 2001, ASPC, 227, 40M

Marscher, A. P., & Gear, W. K. 1985, ApJ, 298, 114

Maselli, A. & Massaro, E. 2009, AN, 330, 295

Maselli, A., Massaro, E., Nesci, R. 2010, A&A 512, 74

Massaro, E., Perri, M., Giommi, P., et al. 2004a, A&A, 413, 489

Massaro, E., Perri, M., Giommi, P., et al. 2004b, A&A, 422, 103

Massaro, E., Tramacere, A., Perri, M., et al. 2006, A&A, 448, 861

Massaro, F. 2007, Ph.D. Thesis

Massaro, F., Tramacere A., Cavaliere A., et al. 2008a, A&A , 478, 395

Massaro, F., Giommi, P., & Tosti, G. 2008b, A&A, 489, 1047

Massaro, E., Giommi, P., Leto, C., et al. 2009 A&A, 495, 691

Massaro, F., Grindlay, J., E., & Paggi, A. 2010a, ApJL, 714, 299

Massaro, E. et al. 2010b A&A submitted http://arxiv.org/abs/1006.0922

Massaro, F., & Grindlay, J., E. 2010c, ApJL submitted

McKinney, J. C. & Gammie, C. F. 2004, ApJ, 611, 977

McKinney, J. C. 2005, ApJ, 630, 5

McNamara, B. R., Kazemzadeh, F., Rafferty, D. A., et al. 2007, ApJ, 698, 594

Meier, D. L. 1999, ApJ, 522, 753

Meier, D. L. 2002, NewAR, 46, 247

Moore, R. L. & Stockman, H. S., 1981, ApJ, 243, 60

Moretti, A., Campana, S., Mineo, T., et al. 2005, SPIE, 5898, 348

Mukherjee, R. 2001, in High Energy Gamma-Ray Astronomy, ed. F. A. Aharonian, & H. J. Vlk (New York: AIP), AIP Conf. Proc., 558, 324

Mushotzky, R. F., 1982, ApJ, 256, 92

Nemmen, R. S., Bower, R. G., Babul, A., et al. 2007, MNRAS, 377, 1652

Nieppola, E., Tornikoski, M., & Valtaoja, E. 2006, A&A, 445, 441

Nilsson, K., Pursimo, T., Sillanpää, A., et al. 2008, A&A, 487, L29

Oke, J., B., & Gunn, J., E. 1974, ApJ, 189, 5

Ostriker, J. P., & McKee, C. F. 1988, Rev. Mod. Phys., 61, 1

Pacciani, L., Vittorini, V., Tavani, M., et al. 2010, ApJ, 716, 170

Padovani, P. 1988, A&A, 192, 9

Padovani, P., & Giommi, P. 1995a, ApJ, 444, 567

Padovani, P., & Giommi, P. 1995b, MNRAS, 277, 1477

Padovani, P., Perlman, E., S., Landt, H., et al. 2003, ApJ, 588, 128

Padovani, P. 2007a, Ap&SS, 309, 63

Padovani, P., Giommi, P., Landt, H., et al. 2007b, ApJ, 662, 182

Paggi, A. 2007, Thesis

Paggi, A., Massaro, F., Vittorini, V. et al. 2009 A&A, 504, 821

Paggi, A., Cavaliere, A., Vittorini, V., et al. 2009b, A&A, 508L, 31

Paltani, S., Courvoisier, T. J. L., Walter, R., 1998, A&A 340, 47

Perlman, E., S., Stocke, J., T., Schachter, J., F., et al. 1996, ApJS, 104, 251

Perri, M., Maselli, A., Giommi, P., et al., 2007, A&A, 462, 889

Peterson, B., M. 1997, *An Introduction to Active Galactic Nuclei*, Cambridge, Cambridge University Press

Pittori, C., Verrecchia, F., Chen, A. W., et al. 2009, A&A, 506, 1563

Protheroe, R., J. 1996, astro-ph/9612212v1

Protheroe, R., J., & Stanev, T. 1999, Astropart. Phy., 10, 185

Rybicki, G., B., & Lightman, A., P. 1979, *Radiative processes in astrophysics*, New York, Wiley

Sambruna, R. M., Maraschi, L., Urry, C. M., 1996 ApJ, 463, 444

Sasada, M., Uemura, M., Arai, A., et al. 2008, PASJ, 60, 37

Scarpa, R., Urry, C., M., Falomo, R., et al. 1999 ApJ, 521, 134

Schmidt, M., 1963, Nature, 197, 1040

Schmitt, J. L., 1968, Nat., 218, 663

Setti, G., & Woltjer, L. 1994, ApJS, 92, 629

Shapiro, S., L., & Teukolsky, S., A. 1983, *Black Holes, White Dwarfs, and Neutron Stars*, New York, Wiley-Interscience

Sikora, M., Begelman, M., C., & Rees, M., J. 1994, ApJ, 421, 123

Snowden, S., Immler, S., Arida, M., et al., 2004, "The *XMM-Newton* ABC Guide" (version 2.01)

Stawarz, L., & Petrosian, V., 2008, ApJ, 681, 1725

Strittmatter, P., A., Serkowski, K., Carswell, R., et al. 1972, ApJ, 175L, 7

Strüder, L., Briel, U., Dennerl, K., et al. 2001, A&A, 365L, 18

Tagliaferri, G., Ravasio, M., & Ghisellini, G. 2003, A&A, 400, 477

Tagliaferri, G., Foschini, L., Ghisellini, G., et al. 2008, ApJ, 679, 1029

Tanihata, C., Kataoka, J., Takahashi, T., et al. 2004, ApJ, 601, 759

Tavecchio, F., Maraschi, L., & Ghisellini, G. 1998, ApJ, 509, 608

Tavecchio, F., & Ghisellini, G. 2008a, AIPC, 1085, 431

Tavecchio, F., & Ghisellini, G. 2008b, MNRAS, 385, 98

Tchekhovskoy, A., McKinney, J. C., & Narayan, R. 2009, ApJ, 699 ,1789

Tramacere, A., Massaro, F., & Cavaliere, A. 2007, A&A, 466, 521

Tramacere, A., Giommi, P., Perri, M. et al. 2009, A&A, 501, 879

Turner, M., J., L., Abbey, A., Arnaud, M., et al. 2001, A&A, 365L, 27

Turnshek, D. A., 1984, ApJ, 280, 51

Urry, C. M., & Padovani, P. 1995, PASP, 107, 803

Urry, C., M., Scarpa, R., O'Dowd, M., et al. 2000 ApJ, 532, 816

Vietri, M. 2006, *Astrofisica delle alte energie*, Torino, Bollati Boringhieri

Villata, M., Raiteri, C., M., Larionov, V., M., et al. 2008, A&A, 481, 79

Vittorini, V., Tavani, M., Paggi, A., et al. 2009, ApJ, 706, 1433